NONLINEAR VIBRATION CONTROL OF THE FLEXIBLE DRIVE-SHAFT SYSTEM WITH NONCONSTANT VELOCITY COUPLING VIA TORSIONAL INPUT

A Dissertation Presented for the

Doctor of Philosophy

Degree

The University of Tennessee, Knoxville

Wei Yao

December 2019

Copyright © 2019 by Wei Yao
All rights reserved.

DEDICATION

To

My parents

Yao, Kouxiang & Mao, Xiuzhen

ACKNOWLEDGEMENTS

I would like to express my deepest gratitude to my primary advisor, Dr. Hans A. DeSmidt, for his excellent guidance, great patience, and moral support during my whole study. His knowledge and dedication inspire my research work. Appreciation is also extended to the members of my Ph.D. committee, Dr. Seddik M. Djouadi, Dr. Eric Wade, and Dr. Xiaopeng Zhao, for their insightful discussions and suggestions.

This research was supported by a grant from the National Science Foundation (Grant Number: NSF-CMMI-0748022) under the Dynamical Systems Program directed by Dr. Eduardo A. Misawa

ABSTRACT

Driveline system involves a complex interconnected multi-link system with a rigorous actuation scheme. A full understanding and description of such a mechanism are crucial to the design and control of assistive driveline system to decrease the vibration and enhance the stability. Sommerfeld effective is the jump phenomena that are observed in the rotor system driving through the critical speed when there is not enough power to overdrive driveshaft under such situations. Then a proper controller is required to control the power source to provide enough large input to the system to spinup over the critical speed.

The purpose of this dissertation is to analyze the Sommerfeld effect in the driveshaft system consisting of Non-Constant Velocity (NCV) flexible couplings and multi-shafts driven by a torque input and develop a torsional control strategy that drives the shaft system through the critical speed smoothly without existence the Sommerfeld effect during the acceleration process.

This dissertation explores the Sommerfeld effect performances in the driveshaft system that includes two NCV flexible couplings and multi-shafts when the driveshaft is driven through the critical frequencies with either unlimited power condition or limited power condition. The parametric performance analysis has been studied to investigate the nonlinear vibration and the energy sink phenomenon.

The hybrid controller consisting of the sliding mode control (SMC) with the linear quadratic regulator (LQR) strategy is theoretically developed to drive the shaft system through the critical frequency without measuring the Sommerfeld effect. The analysis shows that under the unlimited power condition, the driveshaft system coupled with the proper hybrid SMC/LQR controller by torsional input overdrives the critical speed smoothly.

For the practical situation, most of the power sources are under a limited power condition, which causes more difficulty in providing enough torque for the driveline system to overdrive the critical speed. Therefore, the driveshaft system operation under the limited power condition is also explored. The SMC/LQR controller is applied to the control of the voltage of the DC motor, which is powered through the electric circuit to control the input torque of the driveline under the limited power condition.

TABLE OF CONTENTS

LIST OF TABLES

LIST OF FIGURES

Chapter 1
INTRODUCTION

1.1 Universal Joint

Non-constant velocity coupling is also called as universal joint (U-joint) or Hooke's Joint, which is widely used in driveshaft system as it can transmit rotational moment through two rigid shafts that can rotate in any direction. The second U-joint is used in the system will cancel the difference of angular velocity on the first U-joint. So, the two U-joints systems can be considered as a constant-velocity joint with the ability to bend in any direction. This system has a more flexible ability to transmitting the rotational moment than a simple constant-velocity joint. (Kirk, Mondy, & Murphy, 1984) show the U-joint is the source of vibration and instability of a driveshaft system. Crolla (1978) explored the driveline system consisting of either one or two Hooke's joints. However, in this research, the intermediate shaft connected by two Hooke's joints was assumed as rigid. (Dewell & Mitchell, 1984) introduced the kinematics of a 4-bolt disk coupling. There exists an additional rotational spring stiffness in this type of coupling. The output speed of the shaft connecting by the U-joint was a function of the input rotating speed and the static misalignment angle.

Then the driveshaft system involving the U-joint has been investigated. (Asokanthan & Wang, 1996) explores the torsional oscillations due to the parametric instability of the two torsional flexible shafts connected by one U-joint. Since no lateral deflection is considered in this model, therefore only the torsional dynamics is studied. The unstable region is near the principle torsional natural frequencies and sum-combination torsional natural frequencies. (Asokanthan & Meehan, 2000) extended to the numerical method for nonlinear analysis on the same model. The results indicated the resonant behaviors in the nonlinear analysis that are not predicted in a linear analysis. Also, the variation of the misalignment angle affects chaotic motion characteristics. (Bulut & Parlar, 2011) explores the stability of the system consisting of two massless torsional flexible shafts interconnected by one U-joint using the monodromy matrix method. The different type of resonance region is found under a large misalignment angle condition.

(Bulut, 2014) modeled the same system using finite element method. The stability analysis was explored using the monodromy matrix method. The results showed the sum-type combination resonance regions are the most of large instability zones in the practical range of misalignment angles. The above research work focused on the stability analysis of two flexible torsional flexible shafts interconnected by one U-joint. Only torsional instability was considered since the lateral shaft orientations were assumed as fixed. (Iwatsubo & Saigo, 1984) analyzed the transverse vibration of a rotor system coupling with a U-joint under the effect of the constant follower load-torque. The parametric and self-excited vibration was induced by constant load-torque transmitted through U-joint when the rotating speed is closed to the sum-combinations of the transverse natural frequencies. (Xu & Marangoni, 1994a) and (Xu & Marangoni, 1994b) studied the lateral vibration of the driveline including the two shafts connecting under either the misaligned or unbalance condition. The research indicated that 2× running speed is closed to the fundamental frequency of the system, then the vibration due to the misalignment is significant.

The torsional-lateral coupled system started to be studied then. (Kato, Ota, & Kato, 1988) analyzed the lateral-torsional coupled vibration of driveshaft system including a flexible drive shaft connected with NCV coupling and supported by a bearing. The stability result showed that when the 2× rotating speed of shaft equaled to the sum of the lateral and the torsional natural frequencies, then the driven shaft is unstable. (Kato & Ota, 1990) studied the shaft coupling with a U-joint with viscous and Coulomb's friction between cross pin and yokes. The analytical results show that the excitations were caused at even multiples of the shaft rotating speed by either viscous friction or Coulomb friction. The magnitude of the excitation induced by viscous friction increase with the larger misalignment angle. However, the excitation induced by Coulomb friction is independent of misalignment angle. Furthermore, when the viscous coefficient on both sides of U-joint is equal, the excitation could be suppressed. (Saigo, Okada, & Ono, 1997) explored stability of the structure of shafts that are mounted on a bearing support coupling with U-joint under the effect of Coulomb friction. The results indicted

Coulomb friction induced the lateral vibration, which would cause the shaft instability. The asymmetry property bearing effectively suppressed the vibration. Furthermore, the misalignment angle stabilized the vibration induced by Coulomb friction. (A. Mazzei Jr, Argento, & Scott, 1999) analysis of the stability of the shaft system consisting of one U-Joint. The driven shaft that was subjected to a constant follower torque was introduced as Rayleigh beam and was mounted by a damped bearing on the other end. The stability analysis presented that flutter instability and parametric instability was caused by the follower torque when the shaft speed was closed to the sum-type combination natural frequencies. (DeSmidt, Wang, & Smith, 2002) explored the rotor-shaft driveline system coupling with one U-joint under the effect of load torque. The driven shaft was assumed as either torsional or lateral flexibility. The torsional-lathe teral interaction caused the parametric instability when the rotating speed was near the sum- combination of the torsional-lateral natural frequencies. Furthermore, the misalignment suppressed the flutter instability for the speed near difference combination of the torsional-lateral natural frequencies induced by load torque.

The previous research work only analyzes the stability of the driveline system consisting of only one U-joint. In most of the practical applications, more than one U-joint will be used to connect the multi-shafts. Therefore, the rotor-shaft system with multiple U-joints was also been studied. (Sheu, Chieng, & Lee, 1996) explored the steady-state response of the driveline system consisting of two U-joints with a rigid intermediate shaft. The results show that the viscous joint damping had nearly zero effect on the fluctuation of output speed. The viscous friction was the main source for the amplitude of critical speed under the low load condition. (DeSmidt, Wang, & Smith, 2004) studied the segmented driveshaft system consisting of two torsional-lateral flexible intermediate shafts connected with two U-joints and follower load torque. The stability analysis results show that the load torque caused the bending-bending combination instability region, the instability is caused by the misalignment in either bending-bending or torsion-bending combination regions. Furthermore, the external damping could be used to suppress the whirling instability.

Moreover, all the previous research works were done under the constant input speed condition. The research work had started to explore the driveshaft system with the variable driving speed condition in recent years. (A. J. Mazzei Jr, 2011) studied the possibilities of the linearly increasing speed of the input shaft to passage through either parametric resonance or the forced resonance in a small speed and time range. It was shown that no sweep rate was found to avoid the forced motion resonance. The nonlinear lateral vibration of the driveline system coupled with one U-joint, internal tuned damper, and a center bearing was explored by (Browne & Palazzolo, 2009) with varying input speed. A significant jump excitation was measured during the accelerating progress and the subsequent jumping during the run-down progress. The misalignment caused the moment excitation, which was also influenced by load inertia.

1.2 Sommerfeld Effect under Nonideal Driving Condition

The stability analysis is used to determine the unstable range of the driveshaft system.

The Sommerfeld effect was first introduced by (Sommerfeld, 1902), which is described in (Kononenko, 1969), who conducted an experiment that consisted of a cantilever beam and a non-ideal energy source. A jump excitation phenomenon was detected in the response of the motor when the rotational speed was driven through the natural frequency of the system. While the driving power was increasing, the rotational speed of the motor remains the same then jump to a higher value, which was higher than the natural frequency. Results show that rotational speed was affected by the lateral vibration in this experiment. The power was consumed to exciting the lateral vibration instead of increasing the rotational speed. Furthermore, the experiment shows that the jump phenomenon occurred in both spinning up and slowing down progress. The ‘Energy Sink’ was first proposed as well.

The non-idea driven condition was explored by researchers to study the chaotic motion. The structure of two bars that were linked and driven by a DC motor. The support point of the pendulum was free to vibrate due to the effect of motion of the motor and the oscillation of pendulum was explored by (Krasnopolskaya & Shvets, 1993), who investigated the parametric conditions for the capture and pass-through region for the undamped shaft with a small unbalanced torque. Two chaotic regions that were closed to the fundamental frequencies were determined. (Belato, Weber, Balthazar, & Mook, 2001) studied a similar case as well. The purpose of this research work was to study the stability regions under the limited power condition. The solutions jumped from a saddle-node bifurcation to another solution with larger magnitude with the speed increasing. Critical parameters were studied to estimate whether the chaotic motion occurred near the fundamental natural frequency.

Then the dynamic system that was similar to the Sommerfeld's description was studied. (Dimentberg, McGovern, Norton, Chapdelaine, & Harrison, 1997) investigate the unbalanced shaft interacted with limited power. The Krylov-Bogoliubov averaging-over-the-period method was applied. A torque-speed curve slope was explored to determine the stability condition of the roots. The results of smooth passage, the passage with the slowdown, and capture were shown with the varying nondimensional torque. The approach to passage the critical frequency of switching of lateral stiffness was proposed and verified by experiment.

Further research work had been done to analyze the chaotic vibrations. A more complicated structure that included two degrees of freedoms with the natural frequencies 1:2 was studied by (Tsuchida, de Lolo Guilherme, & Balthazar, 2005).

The nonlinear spring was added to the system for the nonlinearity analysis by (Bolla, Balthazar, Felix, & Mook, 2007). A frequency-response curve was obtained to determine the Bifurcation phenomenon. The multi-scale perturbation technique was applied to analyze the problem. The additional nonlinear electromechanical vibration absorber was added to the previous structure by (Felix & Balthazar, 2009). The absorber significantly reduced the vibration amplitude of the cantilevered beam. (Gonçalves, Silveira, Junior, & Balthazar, 2014) explored the cantilever beam driven by a non-ideal power source analytically and experimentally. The system parameters and the operational procedure of the motor were determined to affect the Sommerfeld effect. Then the study of Sommerfeld effect was extended to the rotor dynamic system by (Samantaray, Dasgupta, & Bhattacharyya, 2010), who explored the rotor drive system consisting of a flexible shaft and a heavy disk under the influence of external and internal damping and gyroscopic forces driven by the nonideal motor. The torsional material damping has a significant effect on suppressing the Sommerfeld effect in the rotor-motor system. (Karthikeyan, Bisoi, Samantaray, & Bhattacharyya, 2015) studied the Sommerfeld effect of rotor-motor using the commercial software ANSYS. The regression equations of the steady state transverse and rotating displacement were developed to fit the data point. The semi-analytical method was used to predict the Sommerfeld effect in the rotor dynamics. (Verichev, 2012) studied the torsional vibration in the resonance zone of the shaft driven by a limited power source. The Sommerfeld effect was also observed near the torsional resonance zone as well. The control strategies were proposed by (Bisoi, Samantaray, & Bhattacharyya, 2017) to drive the rotor through the resonance. The voltage control and the field control were applied in the strategies design. The control methods were designed for both the shunt DC motor and the series wound DC motor. Switched control was proposed tor switching between the shunt and series configurations.

1.3 Sliding Mode Control Method

(Vadim Utkin, 1977) introduced a robust control method for variable structure system including uncertainties and disturbances named as a sliding mode. A discontinuous control was introduced to switch the structure of the system on the interaction of designed sliding lines. (Yoerger & Slotine, 1985) applied the sliding mode surfaces on the trajectory control of the system with parametric uncertainty. A dynamic system of the sliding surface was introduced for the general nth order differential equations. The boundary layer was discussed for the tradeoff between the model uncertainty and the controlling precision. (Vadim Utkin & Shi, 1996) proposed a new form of sliding mode control algorithm for the system with uncertainty named as the integral sliding mode. The system in sliding surfaces with integral sliding mode control was of the same order with the original whole system.

The above research works were investigated base on state feedback condition. However, most of the practical problems could be output feedback ones since some states were not measurable. (Li & Slotine, 1987) explored the sliding controller design for the output controllable system. The independent sliding controllers were designed for each output. (Slotine, Hedrick, & Misawa, 1987) introduced an observer including sliding surfaces. (El-Khazali & Decarlo, 1995) investigated the sliding mode control method for static output feedback of the linear invariant system. Two design algorithms of the switching surface were considered. (Woodham & Zinober, 1993) explored the possibility of the eigenvalue placement of the linear closed-loop system in a bounded region. The robust discontinuous observer for the uncertain dynamic system was developed by (Edwards & Spurgeon, 1994). The numerical algorithm was introduced for robust observer design. (Edwards & Spurgeon, 1995) introduced a new procedure for sliding mode controller of an uncertain output feedback system without designing the observer. The eigenvalues assignment results were used for designing the sliding planes. (Wang & Fan, 1993) proposed estimation of control gain for the output feedback condition. This simple adaption law was applied to the control algorithm so that there was no necessity to design the observer. (Wang & Fan, 1994) introduced a new form of sliding surface for the output feedback system. This algorithm was used to stabilize the uncertain systems without observers. (S. Bag, S. Spurgeon, & C. Edwards, 1996) and (S. K. Bag, S. K. Spurgeon, & C. Edwards, 1996) investigated the robust switching surface design applied to the variable structure system with output feedback. The probability of eigenvalues placement for the output feedback was also explored. (Edwards, Spurgeon, & Akoachere, 2000) used the LMI method to determine the sliding surface and control law gain for the output feedback system. (Lewis & Sinha, 1999) introduced the sliding mode control algorithm that was used for the mechanical system with uncertainty. The approach to determine the control gain vector was developed to satisfy the reaching condition.

All the above research works were done based on the matching condition. The reduced order system that determines the stability is the linear invariant system without the uncertainty or disturbances. (Chan, Tao, & Lee, 2000) investigated the sliding mode controller for state feedback linear systems with mismatched time varying state matrix. The sliding mode control algorithm for the output feedback system was proposed by (Pai & Sinha, 2006) when the matching condition was not satisfied by a time-varying state matrix but satisfied by the input matrix and the disturbance matrix. An adaption law was also used to estimate the upper bound of the state norm to avoid the observer.

1.4 Objectives

The stability analysis of the driveline system coupling with the U-joint under steady state condition has been explored by the above researches. Most research work model includes only on U-joint. Only a few researchers focus on the multiple U-joints, and most previous research assumes the constant input speed. The sliding mode control method is widely studied as an effective robust control method for the system including uncertain term, especially for the complicated nonlinear system since the 1970s.

As cited above, many researchers have studied the chaotic problems in rotor-motor system affected by lateral vibration.

The objective of this thesis is to design a control method to drive the nonlinear driveshaft system through the resonance speed with either unlimited or limited power source by the unique pure torque input. The nonlinear shaft model was developed to study the Sommerfeld effect with a constant torque input. A sliding mode control is applied to drive the shaft through the resonance zone, which is called as the passage result. The nonlinear driveshaft system coupling with the U-joint is developed. Then the Sommerfeld effect is studied on the nonlinear system with the constant torque input. A hybrid SMC/LQR control strategy is proposed for the torque input control to drive the shaft system through the resonance region escape from the capture phenomenon. The power is unlimited for the controller. Furthermore, a limited power source is modeled instead of the unlimited torque input. A feedback control method is designed for the limited power control to drive the shaft through the resonance as the same result as the unlimited power control.

Chapter 2
DEVELOPMENT OF DRIVELINE ROTORDYMAMIC SYSTEM MODEL

2.1 Introduction

The comprehensive analytical model of the driveshaft system has been developed to facilitate analysis of the dynamics. The nonlinear model of segmented shafts coupling with two U-joints model is introduced. The system model is assumed as the fully nonlinear. The intermediate shaft is assumed as elastic, the input and the output shaft are assumed as rigid ones. The rotor disk is attached to the end of the output shaft coupled with a follower load torque. A bearing is mounted on the ground at the middle of the output shaft to provide external stiffness and damping property. Therefore, the lateral and torsional motions are coupled in the nonlinear model. The constraint conditions that assume the output shaft is parallel to the input shaft are applied to the nonlinear system model, only the in-plane motion is involved, the zero out-of-plane motion is assumed. The nonlinear equations of motion of the driveshaft system coupled with U-joints are obtained in this chapter. Furthermore, the reduced 2-DOF model is introduced as well. In this 2-DOF reduction model, the lateral motion is assumed to be zero, only the torsional motion is considered.

2.2 Modeling the Nonlinear Driveshaft System

The driveshaft system is shown in Figure 2.1 and Figure 2.2 consists of a rigid input and output shaft, and a flexible intermediate shaft. The segments of shafts are connected with two U-joints, A and B, which are set as the in-phase condition which is 90° phase angle difference about the shaft rotation axis, i.e. $\psi_A = 0^o$, and $\psi_B = 90^o$. L_s is the length of the shaft. The output shaft is mounted by a roller bearing, which is L_b axial distance measured from the NCV flexible coupling B.

The global coordinate frame is fixed at the origin point. Then the coordinates {**a**}, {**b**}, and {**c**} are body fixed coordinates that respect to three driveline shafts. Assume that the power source that provides the torque to the system is assumed to be connected seamless to the input shaft, then the power source rotational speed is as same as the input rotational speed of the driveline shaft system. The input shaft is fixed and only free for rotation. The intermediate and output shafts are free for either lateral displacement or rotation. A rotor load of the inertia J_L that receives the load torque is attached to the output shaft.

$\delta_1(t)$ and $\delta_2(t)$ are misalignment angle in $\mathbf{n_1}$-$\mathbf{n_2}$ plane respect to NCV coupling A and B. $\gamma_1(t)$ and $\gamma_2(t)$ are respect misalignment angles in the $\mathbf{n_1}$-$\mathbf{n_3}$ plane shown in Figure 2.2. $\phi(t)$ is the rotation angle of input shaft, $\phi_2(t)$ and $\phi_L(t)$ are the rotational angle of intermediate and output shafts.

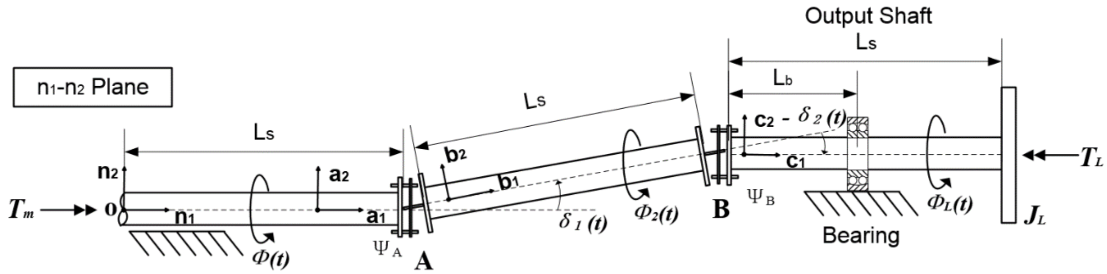

Figure 2.1 Shaft system Configuration in n1-n2 plane

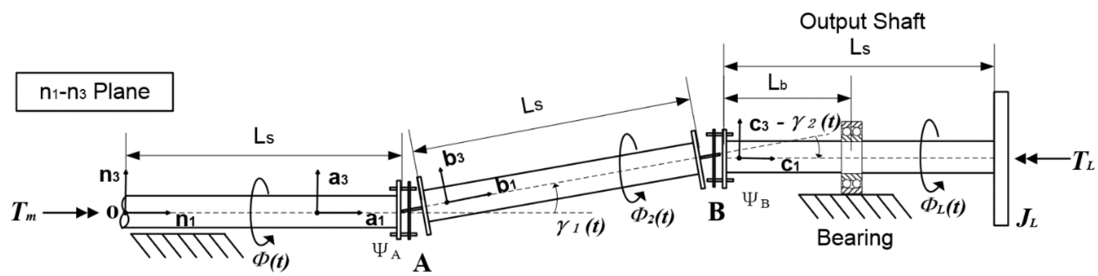

Figure 2.2 Driveshaft System Configuration in n1-n3 plane

2.3 Flexible Shaft and U-joint Kinematics

Figure 2.3 shows the typical structure of U-joint where two body fixed coordinates are attached to the respective ends of the coupling. This coupling has two rotation axes from the input coordinate to the output coordinate as Euler angles α_1 and β_1. The input yoke is described as a frame $\{\mathbf{a}\} = [\mathbf{a_1},\ \mathbf{a_2}, \mathbf{a_3}]^T$. The output frame is described as a frame $\{\mathbf{b}\} = [\mathbf{b_1}, \mathbf{b_2},\ \mathbf{b_3}]^T$. Then the rotation sequence is shown in equation (2.1)

$$\{\mathbf{n}\} \xrightarrow{(\phi+\psi_A)\mathbf{n_1}} \{\mathbf{a}\} \xrightarrow{\alpha_1 \mathbf{a_2}} \{\mathbf{a}'\} \xrightarrow{\boldsymbol{\beta_1} \mathbf{a}'_3} \{\mathbf{b}\} \qquad (2.1)$$

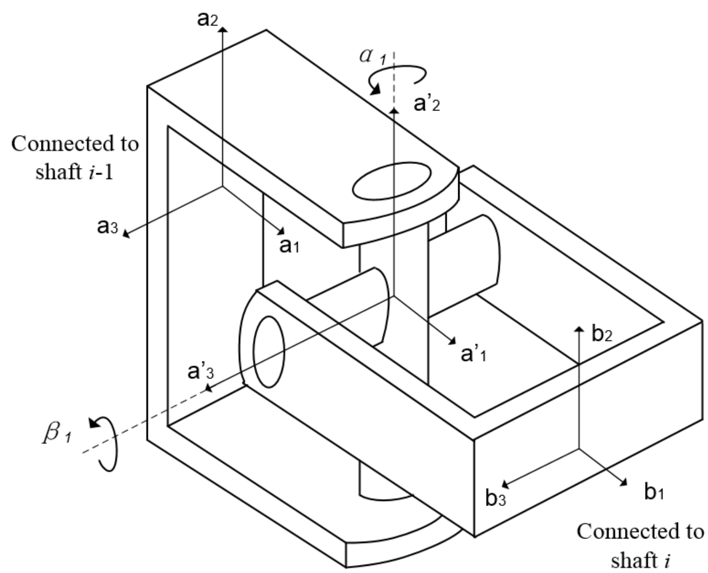

Figure 2.3 Universal Joint with Eulerian Angles α_1 and β_1

Then we can also define the rotation sequence for the U-joint B in equation (2.2)

$$\{\mathbf{b}\} \xrightarrow{(\varphi+\psi_B)\mathbf{b_1}} \{\mathbf{b}'\} \xrightarrow{\alpha_2 b_2'} \{\mathbf{c}'\} \xrightarrow{\beta_2 \mathbf{c}_3'} \{\mathbf{c}\} \tag{2.2}$$

Since the two rotation angles are defined as Eulerian angles, then the rotation transformation matrices can be applied for the coordinates transform. **T** matrixes are the rotation transformation matrices as a body fixed the rotation. $\mathbf{T_{ij}}$ means the rotation transformation from i coordinate to j coordinate. Such as the $\mathbf{T_{na}}$ mean the rotation transformation from {**n**} coordinate system to {**a**} coordinate.

The input and output shafts are assumed to be rigid. The intermediate shaft is modeled as flexible shaft, therefore there is rotational stiffness that will be determined by shaft parameters, and a twist angle $\varphi(t)$ is defined as well. $\mathbf{J_{ms}}$ is the matrix of moment of inertia that is shown in

$$\mathbf{J_{ms}} = \begin{bmatrix} J_s & 0 & 0 \\ 0 & I_s & 0 \\ 0 & 0 & I_s \end{bmatrix} \tag{2.3}$$

Therefore, the body fixed coordinate frames {**a**}, {**b**}, and {**c**} in Figure 2.1 and Figure 2.2 can be expressed in global coordinate {**n**} by multiplying the transformation matrices.

$$\begin{bmatrix} \mathbf{a_1} \\ \mathbf{a_2} \\ \mathbf{a_3} \end{bmatrix} = \begin{bmatrix} 1 & 0 & 0 \\ 0 & \cos(\phi+\psi_A) & sin(\phi+\psi_A) \\ 0 & -sin(\phi+\psi_A) & cos(\phi+\psi_A) \end{bmatrix} \begin{bmatrix} \mathbf{n_1} \\ \mathbf{n_2} \\ \mathbf{n_3} \end{bmatrix} = \mathbf{T_{na}} \begin{bmatrix} \mathbf{n_1} \\ \mathbf{n_2} \\ \mathbf{n_3} \end{bmatrix} \tag{2.4}$$

$$\begin{bmatrix} \mathbf{a'_1} \\ \mathbf{a'_2} \\ \mathbf{a'_3} \end{bmatrix} = \begin{bmatrix} cos\alpha_1 & 0 & sin\alpha_1 \\ 0 & 1 & 0 \\ -sin\alpha_1 & 0 & cos\alpha_1 \end{bmatrix} \begin{bmatrix} \mathbf{a_1} \\ \mathbf{a_2} \\ \mathbf{a_3} \end{bmatrix} = \mathbf{T_{aa'}} \begin{bmatrix} \mathbf{a_1} \\ \mathbf{a_2} \\ \mathbf{a_3} \end{bmatrix} \tag{2.5}$$

$$\begin{bmatrix} \mathbf{b_1} \\ \mathbf{b_2} \\ \mathbf{b_3} \end{bmatrix} = \begin{bmatrix} cos\beta_1 & sin\beta_1 & 0 \\ -sin\beta_1 & cos\beta_1 & 0 \\ 0 & 0 & 1 \end{bmatrix} \begin{bmatrix} \mathbf{a_1} \\ \mathbf{a_2} \\ \mathbf{a_3} \end{bmatrix} = \mathbf{T_{a'b}} \begin{bmatrix} \mathbf{a'_1} \\ \mathbf{a'_2} \\ \mathbf{a'_3} \end{bmatrix} \tag{2.6}$$

$$\begin{bmatrix} \mathbf{b'_1} \\ \mathbf{b'_2} \\ \mathbf{b'_3} \end{bmatrix} = \begin{bmatrix} 1 & 0 & 0 \\ 0 & \cos(\varphi+\psi_B) & sin(\varphi+\psi_B) \\ 0 & -sin(\varphi+\psi_B) & cos(\varphi+\psi_B) \end{bmatrix} \begin{bmatrix} \mathbf{b_1} \\ \mathbf{b_2} \\ \mathbf{b_3} \end{bmatrix} = \mathbf{T_{bb'}} \begin{bmatrix} \mathbf{b_1} \\ \mathbf{b_2} \\ \mathbf{b_3} \end{bmatrix} \tag{2.7}$$

$$\begin{bmatrix} \mathbf{c'_1} \\ \mathbf{c'_2} \\ \mathbf{c'_3} \end{bmatrix} = \begin{bmatrix} cos\alpha_2 & 0 & sin\alpha_2 \\ 0 & 1 & 0 \\ -sin\alpha_2 & 0 & cos\alpha_2 \end{bmatrix} \begin{bmatrix} \mathbf{b'_1} \\ \mathbf{b'_2} \\ \mathbf{b'_3} \end{bmatrix} = \mathbf{T_{b'a'}} \begin{bmatrix} \mathbf{b'_1} \\ \mathbf{b'_2} \\ \mathbf{b'_3} \end{bmatrix} \tag{2.8}$$

$$\begin{bmatrix} \mathbf{c_1} \\ \mathbf{c_2} \\ \mathbf{c_3} \end{bmatrix} = \begin{bmatrix} cos\beta_2 & sin\beta_2 & 0 \\ -sin\beta_2 & cos\beta_2 & 0 \\ 0 & 0 & 1 \end{bmatrix} \begin{bmatrix} \mathbf{c'_1} \\ \mathbf{c'_2} \\ \mathbf{c'_3} \end{bmatrix} = \mathbf{T_{c'c}} \begin{bmatrix} \mathbf{c'_1} \\ \mathbf{c'_2} \\ \mathbf{c'_3} \end{bmatrix} \tag{2.9}$$

The position vector of the mass center of each shaft can be expressed as the following equations.

$$\boldsymbol{r_{m1}} = \frac{L_s}{2}\mathbf{a_1} \tag{2.10}$$

$$\boldsymbol{r_{m2}} = L_s\mathbf{a_1} + \frac{L_s}{2}\boldsymbol{b_1} \tag{2.11}$$

$$\boldsymbol{r_{m3}} = L_s\mathbf{a_1} + L_s\mathbf{b_1} + \frac{L_s}{2}\mathbf{c_1} \tag{2.12}$$

Generally, we can get the velocity by deriving the position vectors of the center of mass on each shaft are determined in equation (2.13)

$$\boldsymbol{v_{m\mathrm{i}}} = \frac{d\boldsymbol{r_{m\mathrm{i}}}}{dt}, \qquad i = 1,2,3 \tag{2.13}$$

Based on the misalignment angle definitions, the configuration of two shafts through one U-joint. $\delta_1(t)$ and $\gamma_1(t)$ are misalignment angles of U-joint A are shown in Figure 2.4.

v_1 and w_1 represent the displacements in {**n**} coordinate frame. Then the {**b**} coordinate frame can be expressed in the global frame by using misalignment angles $\delta_1(t)$ and $\gamma_1(t)$.

$$\begin{bmatrix}\mathbf{b_1}\\\mathbf{b_2}\\\mathbf{b_3}\end{bmatrix} = \begin{bmatrix} l_{b_1a_1} & l_{b_1a_2} & l_{b_1a_3}\\ l_{b_2a_1} & l_{b_2a_2} & l_{b_2a_3}\\ l_{b_3a_1} & l_{b_3a_2} & l_{b_3a_3}\end{bmatrix}\begin{bmatrix}\mathbf{a_1}\\\mathbf{a_2}\\\mathbf{a_3}\end{bmatrix} = [R_1]\begin{bmatrix}\mathbf{a_1}\\\mathbf{a_2}\\\mathbf{a_3}\end{bmatrix} = [R_1]\mathbf{T_{na}}\begin{bmatrix}\mathbf{n_1}\\\mathbf{n_2}\\\mathbf{n_3}\end{bmatrix} \tag{2.14}$$

Where $l_{b_ia_j}$ is the cosine of the angle between the axis b_i and axis a_j, $i, j = 1,2,3$.

Now using the equations from (2.4) to (2.6), we have the expression of {**b**} in global coordinate using the Eulerian angles α_1 and β_1

$$\begin{bmatrix}\mathbf{b_1}\\\mathbf{b_2}\\\mathbf{b_3}\end{bmatrix} = \mathbf{T_{a'b}}\mathbf{T_{aa'}}\mathbf{T_{na}}\begin{bmatrix}\mathbf{n_1}\\\mathbf{n_2}\\\mathbf{n_3}\end{bmatrix} = \mathbf{T_{nb}}\begin{bmatrix}\mathbf{n_1}\\\mathbf{n_2}\\\mathbf{n_3}\end{bmatrix} \tag{2.15}$$

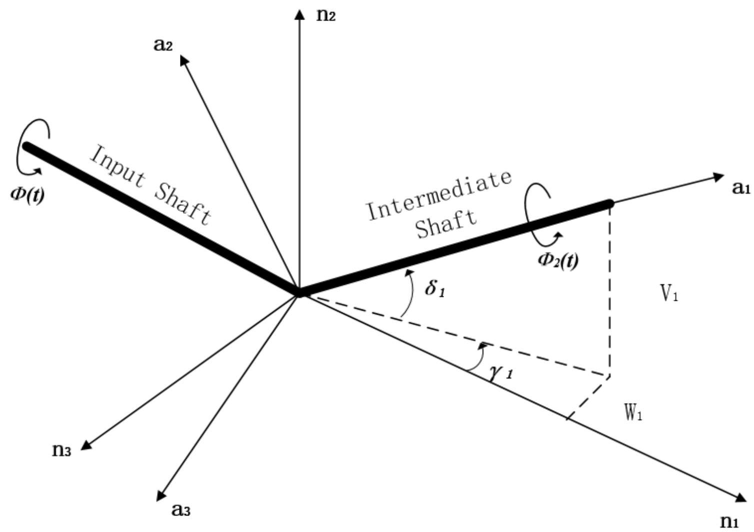

Figure 2.4 Configuration of Shafts through Misalignment Angles of U-joint A

By equating the equation (2.12) and equation (2.13), to eliminate the Eulerian angles α_1 and β_1, let $\Phi_1 = \phi + \psi_A$, $\Phi_2 = \varphi + \psi_B$ we have the expressions

$$\cos(\alpha_1) = \frac{\sec\beta_1\sqrt{{L_s}^2 - V^2 - W^2}}{L_s} \tag{2.16}$$

$$\sin(\alpha_1) = \frac{\sec(\beta_1)(\sin(\phi + \psi_A)\,V - \cos(\phi + \psi_A)W)}{L_S} \tag{2.17}$$

$$\sin(\beta_1) = \frac{\cos(\phi + \psi_A)\,V + \sin(\phi + \psi_A)\,W}{L_s} \tag{2.18}$$

The following equations from equation (2.19) to equation (2.22) are also used to eliminate the Eulerian angles.

$$\sec(\beta_1) = \frac{1}{\cos(\beta_1)} \tag{2.19}$$

$$\cos(\beta_1) = 1 - sin^2(\beta_1) \tag{2.20}$$

$$V = L_s \sin(\delta_1) \tag{2.21}$$

$$W = L_s \sin(\delta_1)\cos(\gamma_1) \tag{2.22}$$

The angular velocities of the input and intermediate shaft are expresses in respect body-fixed coordinate frame as in equation (2.23) and equation (2.24). $\dot{\phi}_1$ is the angular velocity vector of the input shaft, $\dot{\phi}_2$ is the angular velocity vector of the intermediate shaft

$$\dot{\phi}_1 = \dot{\phi}\mathbf{n_1} \tag{2.23}$$

$$\begin{aligned} \dot{\phi}_2 = {} & \dot{\phi}_{21}(\phi, \dot{\phi}, \delta_1, \dot{\delta}_1, \gamma_1, \dot{\gamma}_1)\mathbf{b_1} + \dot{\phi}_{22}(\phi, \dot{\phi}, \delta_1, \dot{\delta}_1, \gamma_1, \dot{\gamma}_1)\mathbf{b_2} \\ & + \dot{\phi}_{23}(\phi, \dot{\phi}, \delta_1, \dot{\delta}_1, \gamma_1, \dot{\gamma}_1)\mathbf{b_3} \end{aligned} \tag{2.24}$$

Where the upper index(**.**) denotes the derivative with respect to time.

$$\dot{\phi}_{21} = \frac{\begin{matrix} [2cos^2\Phi_1\, sin\,\delta_1 + \sin\gamma_1(-2\, sin\,\gamma_1\, sin\,\delta_1\, sin^2\Phi_1 \\ +\cos(2\delta_1)\sec\delta_1\sin(2\Phi_1)))\dot{\gamma}_1 \\ -\cos\gamma_1 \sec\delta_1((2\, sin(\gamma_1)\, sin^2\Phi_1 \\ +\sin(2\Phi_1)\tan\delta_1)\dot{\delta}_1 + 2\dot{\phi})] \end{matrix}}{\begin{matrix} 2[-sec^2\delta_1 + sin^2\gamma_1 sin^2\Phi_1 + sin\,\gamma_1 \sin(2\Phi_1)\tan\delta_1 \\ +cos^2\Phi_1 tan^2\delta_1] \end{matrix}} \tag{2.25}$$

$$\dot{\phi}_{22} = \frac{cos\,\delta_1\,(-\,cos\,\delta_1\, sin\,\Phi_1 + \sin\gamma_1 sin\,\delta_1\, sin\,\Phi_1)\,\dot{\gamma}_1 + cos\,\gamma_1\Phi_1\dot{\delta}_1}{\sqrt{term1}} \tag{2.26}$$

$$\dot{\phi}_{23} = \frac{(cos\,\delta_1\, sin\,\Phi_1 - \sin\gamma_1 sin\,\delta_1\, sin\,\Phi_1)\dot{\gamma}_1 + cos\gamma_1\, cos\,\delta_1\, sin\,\Phi_1\,\dot{\gamma}_1}{\sqrt{term1}} \tag{2.27}$$

$$\begin{aligned} term1 = {} & 1 - cos^2\Phi_1 sin^2\delta_1 - cos^2\delta_1 sin^2\gamma_1 sin^2\Phi_1 \\ & -\ cos\,\delta_1\, sin\,\gamma_1\, sin\,\delta_1 \sin(2\Phi_1) \end{aligned} \tag{2.28}$$

2.4 Kinematically Inverse Model

In this section, the kinematically inverse model is proposed with the constraint condition, which assumes that the only the in-plane movement is considered. The high stiffness on the out-of-plane direction is assumed. Therefore, the out-of-plane movement is assumed as zero.

To estimate vibration phenomenon under the lateral deflection due to misalignment angles, the output shaft is supposed to be kept horizontal to the input shaft under the misalignment angle configuration as $[\gamma_1(t) = 0,\ \gamma_2(t) = 0, \delta_2(t) = -\delta_1(t)]$, which is called the 'offset misalignment' condition. The new structure of the driveshaft system is shown in Figure 2.5, which illustrates all of the new degrees of freedom (DOF) of the mathematical system. With the constraint condition, the Eulerian angles α_2 and β_2 of U-joint B, are expressed as the function of Eulerian angles of α_1 and β_1 of U-joint.

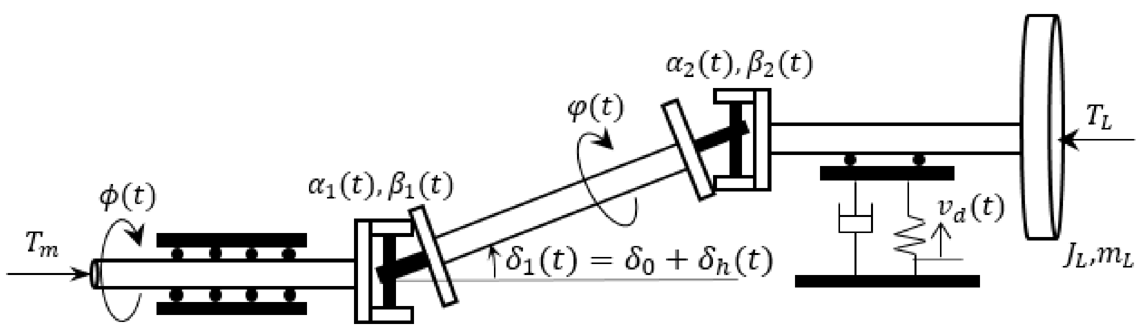

Figure 2.5 Constraint System with New DOF

The body fixed frame $\{\mathbf{c}\} = [\mathbf{c_1}, \mathbf{c_2}, \mathbf{c_3}]^T$ is expressed as respect to the global fixed frame $\{\boldsymbol{n}\}$ as shown in equation

$$\mathbf{c_1} = \mathbf{n_1} \tag{2.29}$$

After substituting equations from equation (2.4) to equation (2.8) into equation (2.9), the body fixed the frame $\{\mathbf{c}\}$ is able to be expressed as a sequence of the rotations respect to the global fixed frame $\{\mathbf{n}\}$ in equation (2.30)

$$\begin{bmatrix}\mathbf{c_1}\\ \mathbf{c_2}\\ \mathbf{c_3}\end{bmatrix} = \mathbf{T_{c'c}}\mathbf{T_{b'a'}}\mathbf{T_{bb'}}\begin{bmatrix}\mathbf{b_1}\\ \mathbf{b_2}\\ \mathbf{b_3}\end{bmatrix} = \mathbf{T_{c'c}}\mathbf{T_{b'a'}}\mathbf{T_{bb'}}\mathbf{T_{a'b}}\mathbf{T_{aa'}}\mathbf{T_{na}}\begin{bmatrix}\mathbf{n_1}\\ \mathbf{n_2}\\ \mathbf{n_3}\end{bmatrix} \tag{2.30}$$

Where from equation (2.30), the body fixed from $\{\boldsymbol{c}\}$ is in from equation (2.31)

$$\mathbf{c_1} = c_{11}\mathbf{n_1} + c_{12}\mathbf{n_2} + c_{13}\mathbf{n_3} \tag{2.31}$$

Where the coefficients are in form from equation (2.32) to equation (2.34)

$$\begin{aligned} c_{11} = {} & \sin\alpha_1[-cos\beta_2 \cos\Phi_2\, sin\alpha_2 + sin\beta_2 \sin\Phi_2] \\ & + cos\alpha_1\{cos\alpha_2 cos\beta_1 cos\beta_2 - sin\beta_1[co\,s\,\Phi_2 sin\beta_2 \\ & + cos\beta_2 sin\alpha_2 sin\Phi_2]\} \end{aligned} \tag{2.32}$$

$$c_{12} = cos\alpha_2 cos\beta_2 sin\beta_1 + cos\beta_1(cos\Phi_2 sin\beta_2 + cos\beta_2 sin\alpha_2 sin\Phi_2) \tag{2.33}$$

$$\begin{aligned} c_{13} = {} & -cos\alpha_2 cos\beta_1 cos\beta_2 sin\alpha_1 \\ & + cos\Phi_2(-cos\alpha_1 cos\beta_2 sin\alpha_2 + sin\alpha_1 sin\beta_1 sin\beta_2) \\ & + (cos\beta_2 sin\alpha_1 sin\alpha_2 sin\beta_1 + cos\alpha_1 sin\beta_2) sin\Phi_2 \end{aligned} \tag{2.34}$$

By equating the equation (2.29) and equation (2.31), then we have equations, which are written in matrix form,

$$\begin{bmatrix} cos\alpha_2 cos\beta_2 \\ cos\beta_2 sin\alpha_2 \\ sin\beta_2 \end{bmatrix} = \begin{bmatrix} cos\alpha_1 cos\beta_1 \\ -cos\Phi_2 sin\alpha_1 - cos\alpha_1 sin\beta_1 sin\Phi_2 \\ -cos\alpha_1 cos\Phi_2 sin\beta_1 + sin\alpha_1 sin\Phi_2 \end{bmatrix} \tag{2.35}$$

Therefore, we have the expressions for Eulerian angles α_2 and β_2 that are functions of Eulerian angles α_1 and β_1. By substituting the additional misalignment angle configuration into angular velocity vector in equation (2.24), which is rewritten as

$$\dot{\phi}_2 = \dot{\phi}_{21}\mathbf{b_1} + \dot{\phi}_{22}\mathbf{b_2} + \dot{\phi}_{23}\mathbf{b_3} \tag{2.36}$$

$$\dot{\phi}_{21} = \frac{\cos\Phi_1 \sin\delta_1 \sin\Phi_1 \dot{\delta}_1 + \cos\delta_1 \dot{\phi}}{-1 + cos^2\Phi_1 \sin^2\delta_1} \tag{2.37}$$

$$\dot{\phi}_{22} = \frac{\sin\Phi_1 \dot{\delta}_1}{\sqrt{1 - cos^2\Phi_1 \sin^2\delta_1}} \tag{2.38}$$

$$\dot{\phi}_{23} = \frac{cos\delta_1\, cos\,\Phi_1 \dot{\delta}_1}{\sqrt{1 - cos^2\Phi_1 sin^2\delta_1}} \tag{2.39}$$

Since the output shaft is constrained to be horizontal to the input shaft, then only the rotational speed about an axis $\mathbf{c_1}$ is considered, which is shown in equation (2.40)

$$\dot{\phi}_L = \frac{\dot{\phi}_{L1}}{\dot{\phi}_{L2}} \tag{2.40}$$

$$\begin{aligned} \dot{\phi}_{L1} = {} & 2(2sin\delta_1 sin(2\Phi_1) sin^2\varphi \\ & + (-cos(2\Phi_1) + cos^2\Phi_1 sin^2\delta_1)\sin(2\varphi)\, tan\delta_1)\dot{\delta}_1 \\ & + 4cos\delta_1 \dot{\Phi}_1 + (3 + \cos(2\delta_1) - 2cos(2\Phi_1) sin^2\delta_1)\dot{\varphi} \end{aligned} \tag{2.41}$$

$$\dot{\phi}_{L2} = 2(2sec\delta_1 + sin\delta_1(-sin\delta_1 sin(2\Phi_1)sin(2\varphi) - 2(1 + cos(2\Phi_1) - cos^2\Phi_1 sin^2\delta_1)sin^2\delta_1)tan\delta_1 \tag{2.42}$$

The lateral displacement v_d is defined as a function of the position v shown in Figure 2.5 minus the static lateral position, which is defined as in equation (2.43). The static lateral position is determined by the static misalignment angle δ_0

$$v_d = v - v_0 = L_s[\sin(\delta_1) - \sin(\delta_0)] \tag{2.43}$$

Now the DOF of the nonlinear driveline system is $q = \{\phi(t), \delta_1(t), \varphi(t)\}^T$.

2.5 Energy Method

The equations of motion of the driveshaft system shown in Figure 2.5 are derived using the energy method. The angular momentum is

$$H = J\omega \tag{2.44}$$

Where J is the cross-sectional polar mass moment of inertia, ω is the cross-section axis rotational speed. Then the kinetic energy associated with rotation is

$$KE_R = \frac{1}{2}\omega H = \frac{1}{2}J\omega^2 \tag{2.45}$$

Therefore, the total kinetic energy of the driveline shaft system is the sum of the translational, rotational kinetic energy shown in equation (2.46). Moreover, the load kinetic energy is derived in equation (2.47)

$$KEs = \sum_{i=1}^{3} KE_i = \frac{1}{2}\sum_{i=1}^{3}(m_i \boldsymbol{v}_{\boldsymbol{i}}^T \boldsymbol{v}_{\boldsymbol{i}}) + \frac{1}{2}\sum_{j=1}^{2} \mathbf{J}_{\mathbf{ms}} \dot{\theta}_j^T \, \dot{\theta}_j + \frac{1}{2} J_s \dot{\theta}_L^2 \tag{2.46}$$

$$KE_L = \frac{J_L}{2} \dot{\theta}_L^2 \tag{2.47}$$

Where KE_i is the kinetic energy of input, intermediate, and output shafts, m_i is the mass of each shaft, v_i is the velocity of each shaft, $\dot{\theta}_i$ is the angular velocity of each shaft, J_S is shaft cross-sectional polar mass moment of inertia in the rotating-frame. Stain energy is also one of the key components of the motion calculation of the driveline system. The strain energy varies with the change of the displacement of the bearing in the shaft of the system. The shaft strain energy, V_s is,

$$V_s = \frac{1}{2} k_b (y_d)^2 + \frac{1}{2} \frac{G_s J_s}{L_s} \varphi(t)^2 \tag{2.48}$$

Where k_b is the lateral stiffness coefficient, G_s is the shaft material shear modulus. The corresponding Rayleigh dissipation function of the driveline shaft system

$$D_s = \frac{1}{2} Cd_b (\dot{y}_d)^2 + \frac{\xi_s}{2} \frac{G_s J_s}{L_s} \dot{\varphi}(t)^2 \tag{2.49}$$

Where Cd_b is the damping of bearing, ξ_s is the shaft material viscous damping coefficient.

2.6 Loading Torque and Virtual Power Terms

The shaft model is combined with an electrical motor. Motor torque T_m and load torque T_L are assumed as inputs for the system. The loading condition and follower loading torque are shown in Figure 2.6. The loading torque is perpendicular to the cross-section plane of the load rotor. T_m is the input torque that is applied to the input shaft. T_L is assumed as follower loading torque, which is not assumed to be of a constant value. $\vec{T}_m$ is the input torque vector in $\mathbf{n_1}$, and $\vec{T}_L$ is the load torque vector in $\mathbf{c_1}$ direction

$$\vec{T}_m = T_m \mathbf{n_1}\,, \qquad \vec{T}_L = T_L \mathbf{c_1} \tag{2.50}$$

$$\delta P_m = \sum \vec{T}_m \frac{\partial}{\partial \dot{q}_j}(\frac{d\vec{\theta}_1}{dt})\delta \dot{q}_j \tag{2.51}$$

$$\delta P_L = \sum \vec{T}_L \frac{\partial}{\partial \dot{q}_j}(\frac{d\vec{\theta}_L}{dt})\delta \dot{q}_j \tag{2.52}$$

Where δP_m and δP_L, are virtual power of the $\vec{T}_m$ and $\vec{T}_L$, which result in generalized forces $\boldsymbol{Q_m}$ and $\boldsymbol{Q_L}$. With

$$\boldsymbol{Q}_{\boldsymbol{m}}^T \delta \dot{q}_j = \delta P_m \Longrightarrow \boldsymbol{Q_m} = \boldsymbol{F}_m(\boldsymbol{q}, \dot{\boldsymbol{q}}) \tag{2.53}$$

$$\boldsymbol{Q}_{\boldsymbol{L}}^T \delta \dot{q}_j = \delta P_L \Longrightarrow \boldsymbol{Q_L} = \boldsymbol{F}_L(q, \dot{q}) \tag{2.54}$$

Furthermore, $\boldsymbol{F}_m$ and $\boldsymbol{F}_L$ are generalized loading vector from effects of input torque and follower loading torque.

2.7 Equations of Motion of the Driveline System

In this section, Lagrange’s Equation is used to obtain the equations of motion of the driveshaft system.

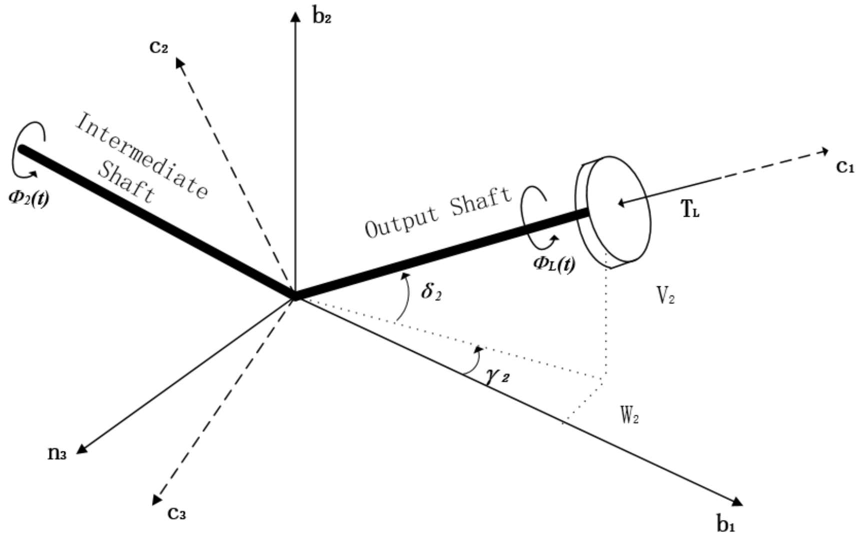

Figure 2.6 Follower Load Condition

The generalized equation including the kinetic energy, potential energy, and the dissipation of the system is shown in equation (2.55)

$$\frac{d}{dt}\left(\frac{\partial(KE_s + KE_L)}{\partial\dot{q}_i}\right) - \frac{\partial(KEs + KE_L)}{\partial q_i} + \frac{\partial V_s}{\partial q_i} + \frac{\partial D_s}{\partial\dot{q}_i} = Q_i, i = 1,2,\dots,N \quad (2.55)$$

Where q_i is the arbitrary set of values, which mean the degree of freedom, which represents the angles of the input shaft, misalignment angles of U-joints, and twists angle. *N* means the number of generalized coordinates. Q_i is the generalized forces. The Lagrange's function of the Lagrange's Equations can be written as,

$$\mathcal{L} = KE_s + KE_L - V_s \quad (2.56)$$

Then the Lagrange's equations can be written by substituting equation (2.56) into equation (2.55)

$$\frac{d}{dt}\left(\frac{\partial \mathcal{L}}{\partial \dot{q}_i}\right) - \frac{\partial \mathcal{L}}{\partial q_i} + \frac{\partial D_s}{\partial \dot{q}_i} = Q_i\,, \qquad i = 1,2,\dots,N \tag{2.57}$$

Therefore, the system dynamics can be written as a set of nonlinear time-varying differential equations (2.58)

$$\boldsymbol{M_n}(q)\ddot{q} + \boldsymbol{NL}(q,\dot{q}) = \boldsymbol{F}_m(q,\dot{q}) + \boldsymbol{F}_L(q,\dot{q}) \tag{2.58}$$

$\boldsymbol{M_n}(q)$ is the time-varying mass matrix of the nonlinear model, and $\boldsymbol{NL}(q,\dot{q})$ is the nonlinear time-varying vector that are functions of of $(q,\dot{q})$.

2.8 2-DOF Model

The critical static misalignment angle has been determined in the previous chapter, which leaves us a question about what effect of the lateral movement will be involved in the speed limits value or the Sommerfeld effect. Therefore, the reduction 2-DOF model is proposed in this section for exploring the lateral movement effect.

Unlike the structure in Figure 2.5, the lateral movement of the output shaft is assumed as zero, which is shown in Figure 2.7. Therefore, the DOF of the system Now the DOF of the nonlinear system is $q_r = \{\phi(t), \varphi(t)\}^T$. Then the torsional-lateral coupled driveline system is reduced to the pure torsional system.

Then apply the energy method and Lagrange’s equation to obtain the EOM of the driveline system.

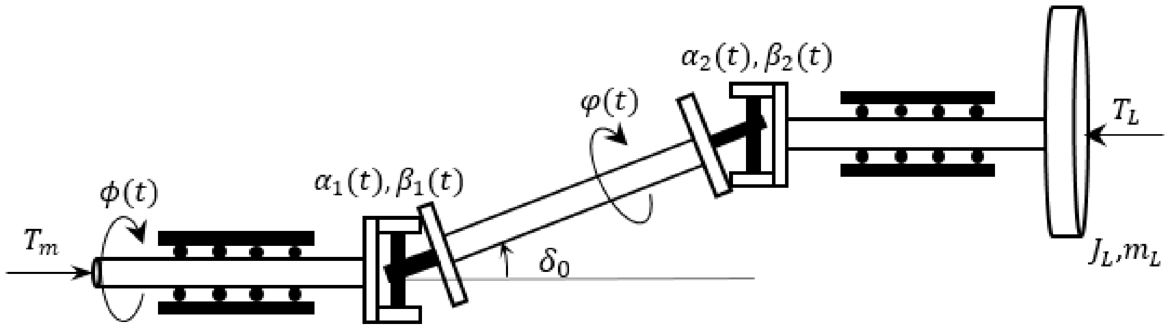

Figure 2.7 Offset Misalignment Condition: 2 DOF

The total kinetic energy of the driveline shaft system is the sum of the translational, rotational kinetic energy of shafts, and the load kinetic energy shown in equation (2.59).

$$KE_r = \frac{1}{2}\sum_{i=1}^{3}\left(m_i \boldsymbol{v}_i^T \boldsymbol{v}_i + J_{sm}\dot{\phi}_i^2\right) + \frac{J_L}{2}\dot{\phi}_L^2 + \frac{1}{2}m_L \boldsymbol{v}_L^T \boldsymbol{v}_L \tag{2.59}$$

Where KE_r is the total kinetic energy of input, intermediate, output shafts, and load rotor, m_i is the mass of each shaft, $\boldsymbol{v}_i$ is the velocity of each shaft, $\dot{\theta}_i$ is the angular velocity of each shaft, J_S is shaft cross-sectional polar mass moment of inertia in the rotating-frame, and $\boldsymbol{v}_L$ is the velocity vector of the rotor. Stain energy V_{sr} is,

$$V_{sr} = \frac{1}{2}\frac{G_s J_s}{L_s}\varphi(t)^2 \tag{2.60}$$

G_s is the shaft material shear modulus.

The corresponding Rayleigh dissipation function of the driveline shaft system

$$D_{sr} = \frac{\xi_s}{2}\frac{G_s J_s}{L_s}\dot{\varphi}(t)^2 \tag{2.61}$$

Where ξ_s is the shaft material viscous damping coefficient.

As well as the previous section, the torque input T_m and load torque T_L are assumed as inputs for the system. The loading condition and follower loading torque are shown in Figure 2.6. The loading torque is perpendicular to the cross-section plane of the load rotor.

T_m is the input torque that is applied to the input shaft. T_L is assumed as follower loading torque, which is not assumed to be of a constant value.

$$\vec{T}_m = T_m \mathbf{n_1}\,, \qquad \vec{T}_L = T_L \mathbf{c_1} \tag{2.62}$$

$$\delta P_{mr} = \sum \vec{T}_m \frac{\partial}{\partial \dot{q}_j}(\frac{d\vec{\theta}_1}{dt})\delta \dot{q}_{jr} \tag{2.63}$$

$$\delta P_{Lr} = \sum \vec{T}_L \frac{\partial}{\partial \dot{q}_j}(\frac{d\vec{\theta}_L}{dt})\delta \dot{q}_{jr} \tag{2.64}$$

Where δP_m and δP_L, are virtual power of the $\vec{T}_m$ and $\vec{T}_L$, which result in generalized forces $\boldsymbol{Q_m}$ and $\boldsymbol{Q_L}$. With

$$\boldsymbol{Q_{mr}^T}\delta \dot{q}_j = \delta P_m \Longrightarrow \boldsymbol{Q_{mr}} = \boldsymbol{F}_{mr}(q_r, \dot{q}_r) \tag{2.65}$$

$$\boldsymbol{Q_{Lr}^T}\delta \dot{q}_j = \delta P_L \Longrightarrow \boldsymbol{Q_{Lr}} = \boldsymbol{F}_{Lr}(q_r, \dot{q}_r) \tag{2.66}$$

Furthermore, $\boldsymbol{F}_{mr}$ and $\boldsymbol{F}_{Lr}$ are generalized loading vector from effects of input torque and follower loading torque.

Using the Lagrange's Equations to obtain the equations of motion for the driveshaft system. Lagrange's Equations can be written as,

$$\mathcal{L} = KE_r - V_{sr} \tag{2.67}$$

Then the Lagrange's equations can be written by substituting equation (2.67) into equation (2.68)

$$\frac{d}{dt}\left(\frac{\partial \mathcal{L}}{\partial \dot{q_{ir}}}\right) - \frac{\partial \mathcal{L}}{\partial q_{ir}} + \frac{\partial D_{sr}}{\partial \dot{q_{ir}}} = Q_{ir} \quad i = 1,2 \tag{2.68}$$

Where q_{ir} is the degree of freedom of the reduced system, which represents the rotation angle of the input shaft and twists angle, Q_{ir} is the generalized force. Therefore, the system dynamics can be written as a set of nonlinear time-varying differential equations (2.69)

$$\boldsymbol{M_{nr}}(q_r)\ddot{q}_r + \boldsymbol{f_r}(q_r, \dot{q}_r) = \boldsymbol{F}_{mr}(q_r, \dot{q}_r) + \boldsymbol{F}_{Lr}(q_r, \dot{q}_r) \tag{2.69}$$

$\boldsymbol{M_{nr}}(q_r)$ is the time-varying mass matrix of the nonlinear model, and $\boldsymbol{f_r}(q_r, \dot{q}_r)$ is the nonlinear time-varying vector that is a function of $(q_r, \dot{q}_r)$.

2.9 Conclusion

The nonlinear model of the segmented driveshaft system coupling with double U-joints is proposed in this chapter. The inverse kinematic method is used with the constraint condition that reduces the full nonlinear model to the 3-DOF system, which is still extremely involving the intense nonlinearity of the coupling of the lateral motion and torsional motion. Furthermore, the 2-DOF nonlinear model is proposed involving only the torsional motion. The input of the system is the input torque, and the load torque needs to be determined for different simulation conditions.

Chapter 3

ANALYSIS OF THE NONLINEAR DRIVESHAFT SYSTEM

3.1 Introduction

The Sommerfeld effect has been studied in recent years, however, the structure of the segmented drivelines coupled with U-joint is not included in these previous research work. To understand the nonlinear jump phenomenon is important to design the driveline system during the accelerating process, especially when the driveline is designed to operate under the supercritical condition. Then the nonlinear jump phenomenon is possible to occur when the rotating speed of the shaft passage the natural frequency. The more power is required when the speed getting closer to the natural frequency. Therefore, the analysis of the Sommerfeld effect of the segmented drivelines system is critical for the coupling of the driveline system with a power source system. The input to the system is considered as the rotating speed of the input shaft in the most previous research. The torque input is practical when the driveline is connected with the power source in the real application. The nonlinear equations of motion described in the previous chapter are used to obtain the responses of the driveshaft system. Torque is an input for the driveline system.

This chapter explores the Sommerfeld effect of the nonlinear driveline system coupling with the U-joint with the torque input.

3.2 Simulation with Constant Torque Input: 3-DOF

3.2.1 Time Domain Response

The nonlinear mathematic equations of motion have been developed through the inverse dynamics and Lagrange equation as shown in equation (2.58).

In the practical application, the driveshaft is driven by the torque. Therefore, the input of the driveline system is the input torque T_m. As shown in Figure 3.1, the input torque is expressed in T_m. To reach a steady state acceleration, the T_m is expressed in

$$T_m = a(J_s + J_L) \tag{3.1}$$

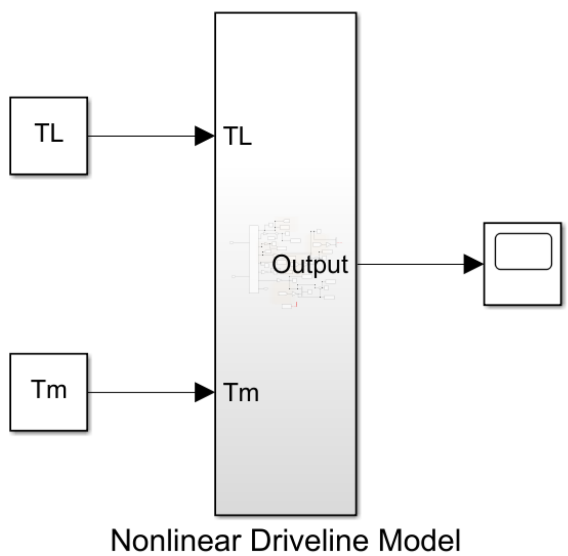

Figure 3.1 Structure of Driveline system with Torque Input

$$T_L = T_{Lv} + T_{Lc} \tag{3.2}$$

$$T_{Lv} = -D_g \Omega_L \tag{3.3}$$

$$T_{Lc} = -\varphi_0 k_{tor} \tag{3.4}$$

Where the φ_0 is the static twist angle. Two load torque conditions are considered in this chapter. The first condition of load torque T_L is viscous such that the $\varphi_0 = 0$. Under this condition, the static misalignment angle is the main parametric variable for investigating. The shaft parameters are listed in the following Table 3.1.

Table 3.1 Driveline System Parameters

	supercritical	subcritical
Number of segments	3	3
Segment length, *L*	3.335m	3.335m
Outer diameter, *D*	0.1443m	0.1443m
Material Density, ρ	2800kg^3/m^3	2800kg^3/m^3
Shear Modulus, *G*	27GPa	10GPa
Load disk diameter, *d*	0.65024m	0.65024m
Load disk thickness, *t*	0.0254m	0.0254m
Viscous coefficient, D_g	1.81×10$^{(-2)}$$\mu Pa \cdot s$	1.81×10$^{(-2)}$$\mu Pa \cdot s$
Lateral Stiffness, k_L	$1 \times 10^7 N \cdot m$	$2 \times 10^8 N \cdot m$
Torsional Damping Coefficient, ξ	2×10^{-4}	2×10^{-4}

The acceleration of the rotating speed is assumed as 2 rad/s^2 in this chapter. Then the input torque can be calculated by equations (3.1) to (3.2). Therefore, the input torque T_m is determined as 31.168 Nm in this section. As the description in chapter 2 and shown in Figure 2.5, the static misalignment angle is the constant value. The misalignment angle expression is shown in equation (3.5).

$$\delta_1(t) = \delta_0 + \delta_h(t) \tag{3.5}$$

Where $\delta_1(t)$ is the dynamic misalignment angle that consists of the static misalignment angle and a perturbation dynamic term, where δ_0 is the static misalignment angle which is determined before the simulation, and $\delta_h(t)$ is the perturbation term of the misalignment angle, which is assumed as a small value.

Figure 3.2 to Figure 3.10 illustrate the response of the perturbation dynamic misalignment angle, twist angle, and output speed for the supercritical case in which the torsional natural frequency is larger than the lateral natural frequency.

The static misalignment angle condition is set from 10^o to 40^o. Figure 3.2 and Figure 3.3 illustrate the passage phenomenon in static misalignment angle of 10^o and 11^o condition. Then the results from Figure 3.5 to Figure 3.10 show that the capture phenomenon occurs in the static misalignment angles from 15^o to 40^o. Referring from results of passage phenomenon, the rotating speed of the shaft will pass the resonance frequency region when the static misalignment angles are lower than 15^o since the result in Figure 3.5 illustrate that the rotating speed of the shaft is captured. Therefore, the static misalignment angle affects the results of the passage or capture phenomenon of the driveshaft system coupling with U-joints.

As the Figure 3.8 and Figure 3.9 show that the more than one resonance speed occurs when the system is under the large misalignment angle condition, passaging through the previous critical speed is also observable from the response. Moreover, the larger static misalignment angle conditions require the large torque to passage away from the Sommerfeld effect due to the corresponding larger amplitude of the oscillation in the torsional response.

As the results show that the speed captured is lower with the increase of the static misalignment angle. The left figure of Figure 3.11 shows the comparison of the all output speeds with different static misalignment conditions.

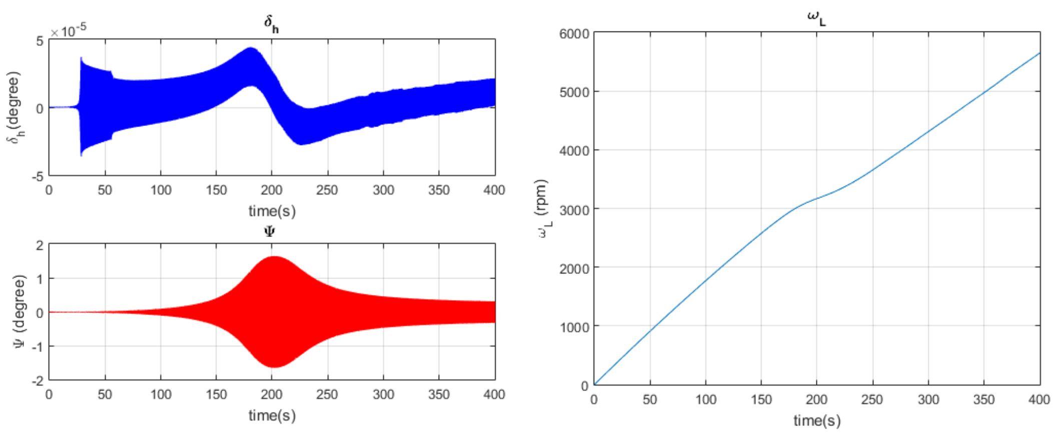

Figure 3.2 Supercritical Passage: $\delta_0 = 10°$

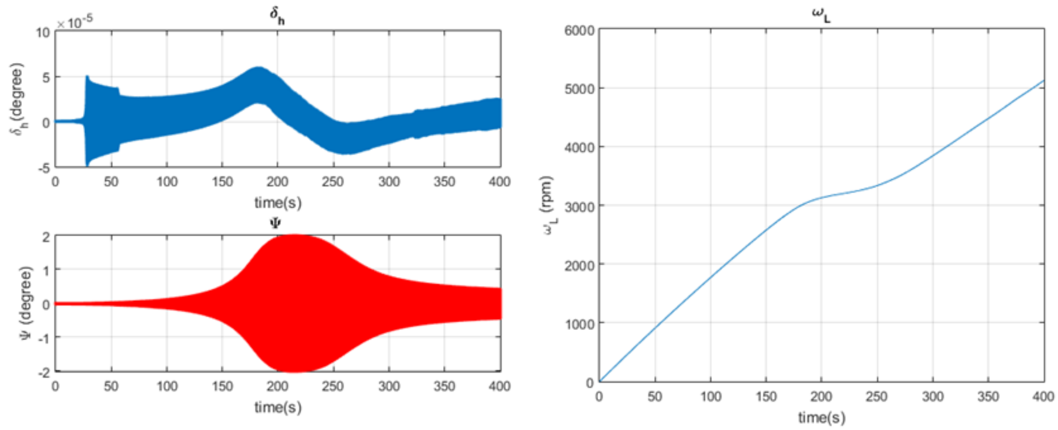

Figure 3.3 Supercritical Passage: $\delta_0 = 11°$

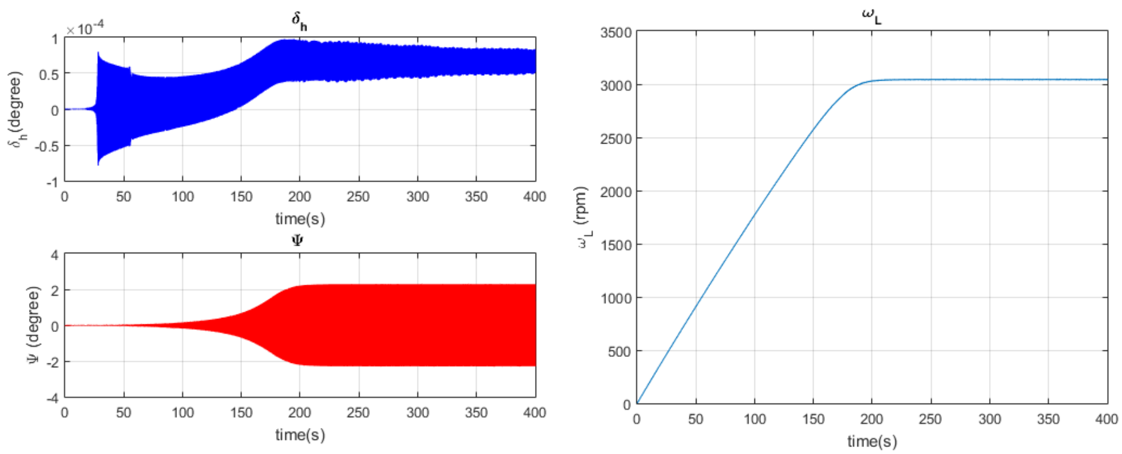

Figure 3.4 Supercritical Passage: $\delta_0 = 13°$

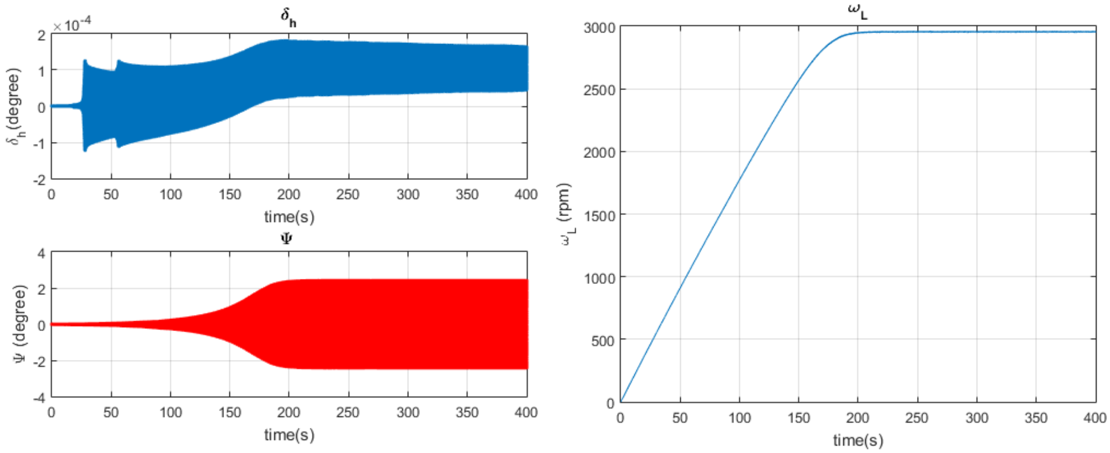

Figure 3.5 Supercritical Passage: $\delta_0 = 15°$

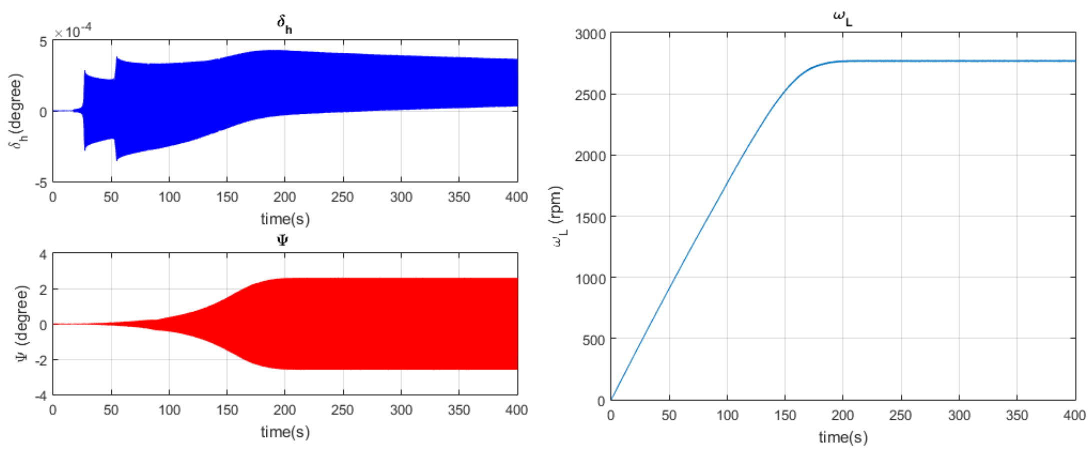

Figure 3.6 Supercritical Passage: $\delta_0 = 20°$

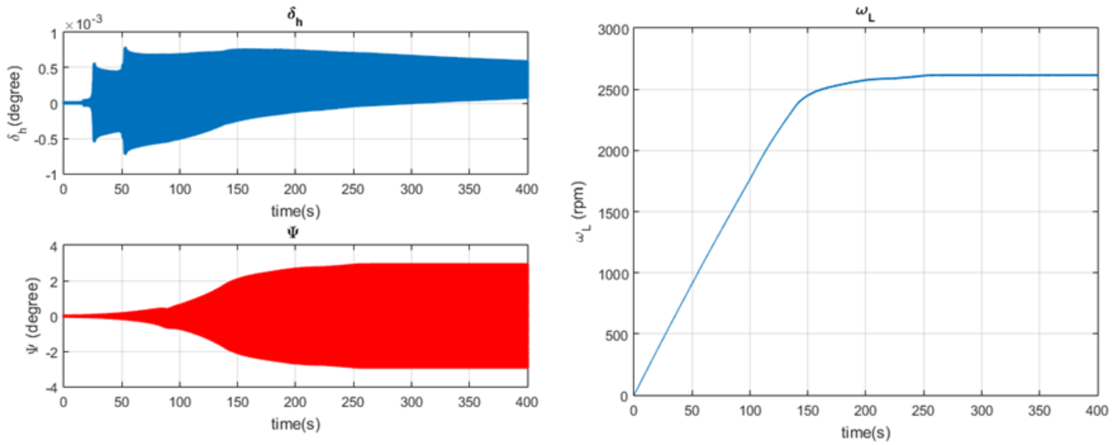

Figure 3.7 Supercritical Capture: $\boldsymbol{\delta_0 = 25°}$

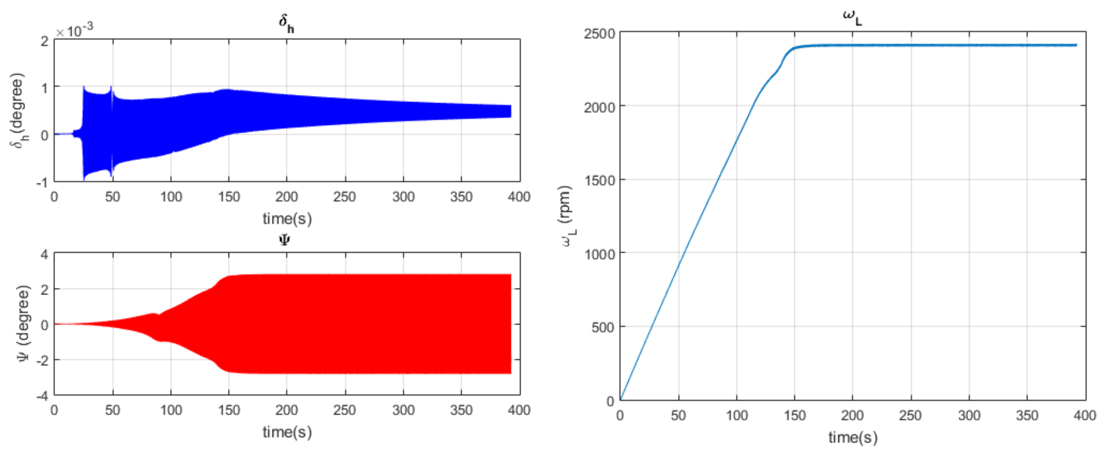

Figure 3.8 Supercritical Capture: $\boldsymbol{\delta_0 = 30°}$

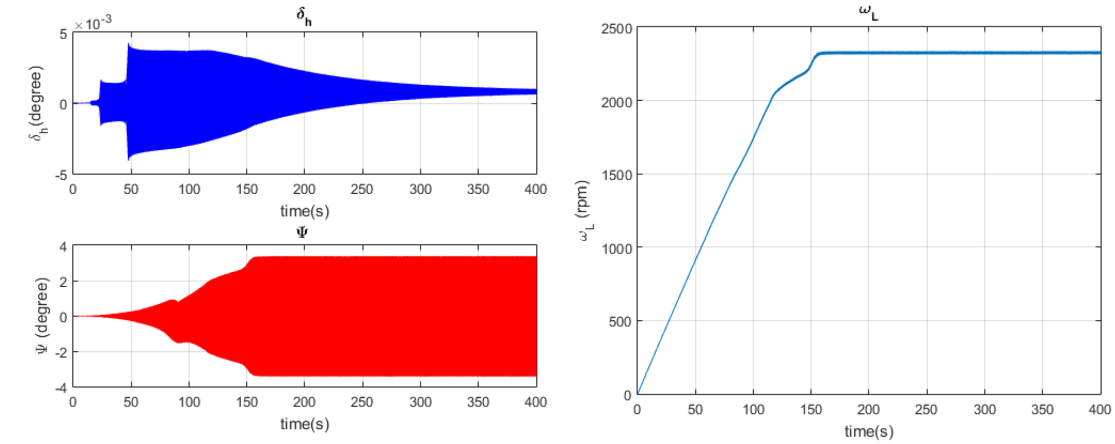

Figure 3.9 Supercritical Capture: $\delta_0 = 35°$

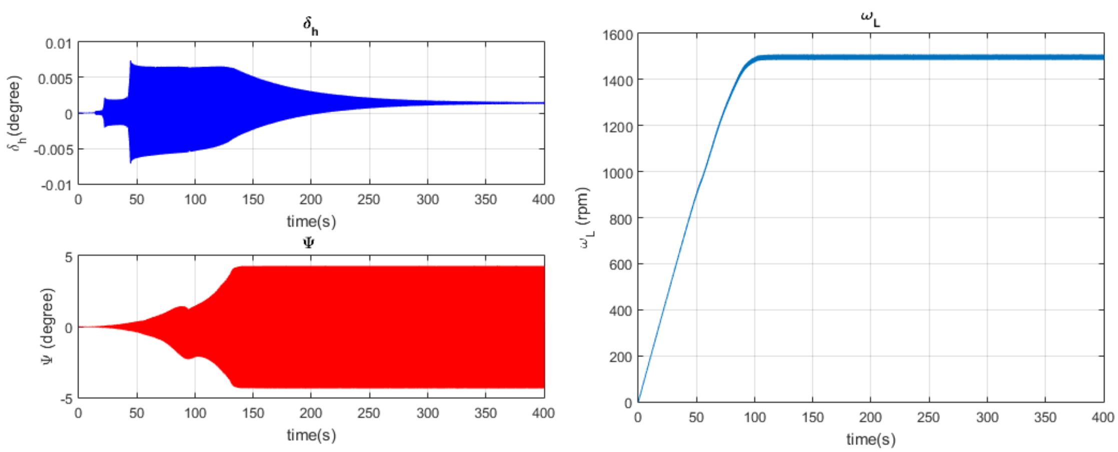

Figure 3.10 Supercritical Capture:$\delta_0 = 40°$

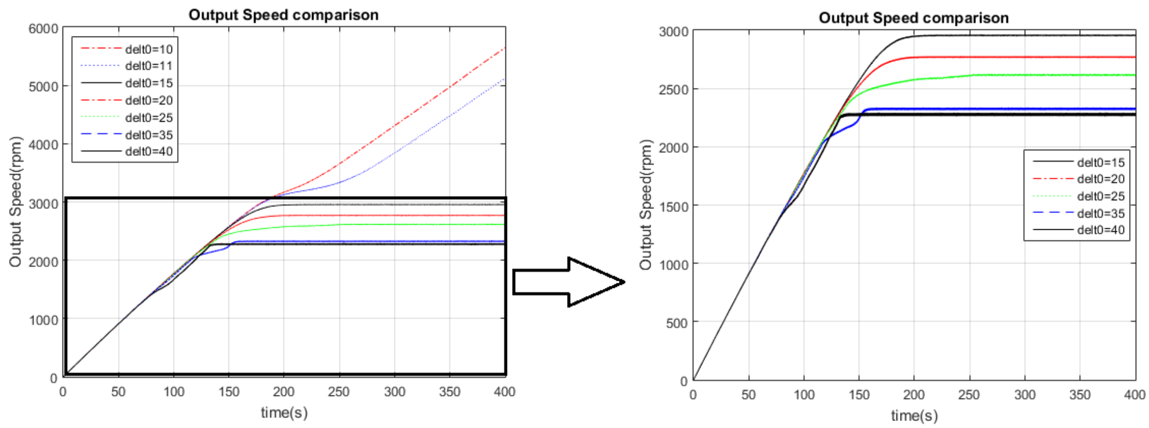

Figure 3.11 Supercritical Case: Rotating Speed Comparison: $\delta_0 = 10°\sim40°$

The right figure in Figure 3.11 illustrates the comparison of rotating speed captured. The larger the static misalignment angle is, the lower the speed limit is. Results show that the output speed passage the critical speed when the static misalignment angles are no larger than 11°. The capture happens when the static misalignment angles are larger than 15°. The results of the subcritical case are shown in figures from Figure 3.12 to Figure 3.20. The torsional natural frequency, in this case, is lower than the lateral natural frequency. As similar as results of the supercritical case, both passage and capture phenomenon is observed. The passage phenomenon occurs in figures from Figure 3.12 to Figure 3.14. However, the different result from the supercritical case is the passage phenomenon is observed in the 13° static misalignment condition, not like the result of the supercritical case in Figure 3.4.

As well as the supercritical case, the capture phenomenon is observed in results from Figure 3.15 to Figure 3.20. The different resonance speed can be observed in lateral response δ_h in capture and passage results. Since the system is nonlinear, which consists of the high frequency terms, then there are excitations when the high torsional critical frequencies passage the lateral natural frequency. This phenomenon can be verified by frequency analysis in the following section. As the similar results of supercritical case, the left figure of Figure 3.21 shows the comparison of the all output speeds with different static misalignment conditions. The right figure in Figure 3.21 illustrates the comparison of rotating speed captured.

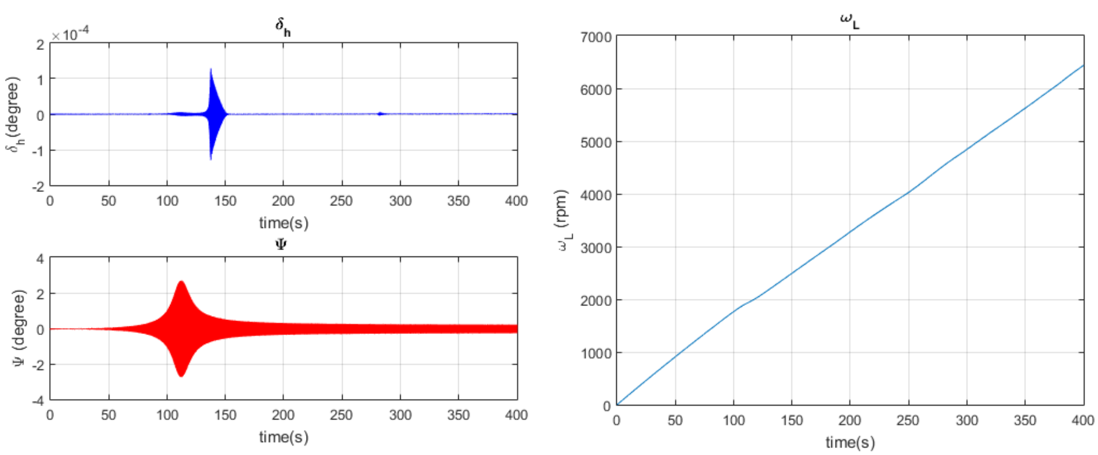

Figure 3.12 Subcritical Passage: $\delta_0 = 10°$

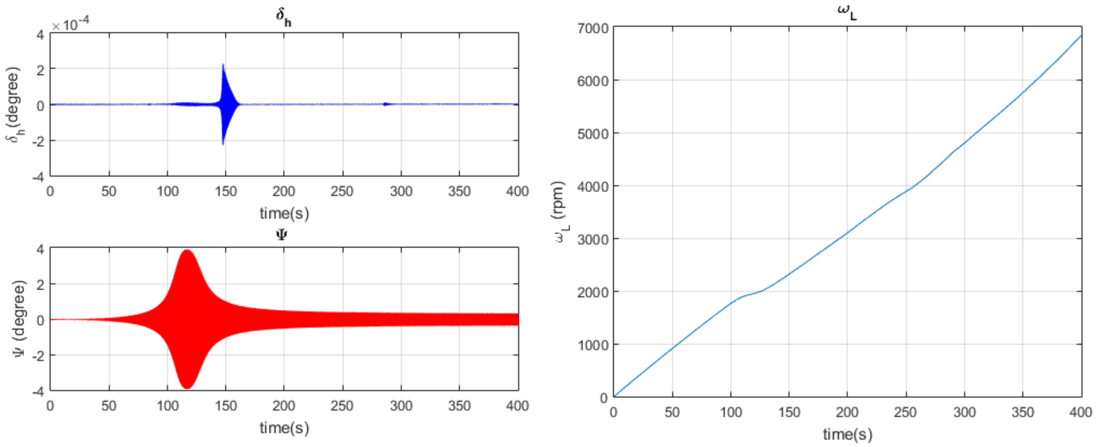

Figure 3.13 Subcritical Passage: $\delta_0 = 12°$

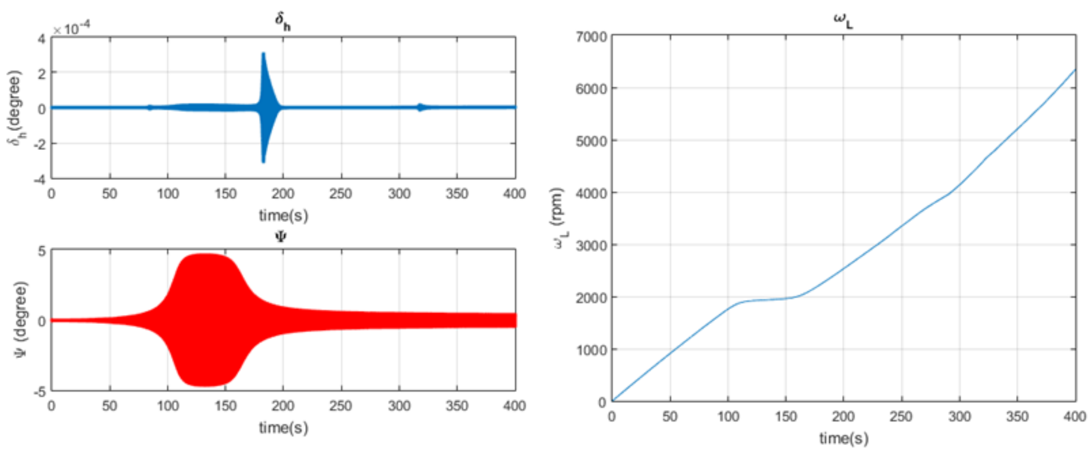

Figure 3.14 Subcritical Passage: $\delta_0 = 13°$

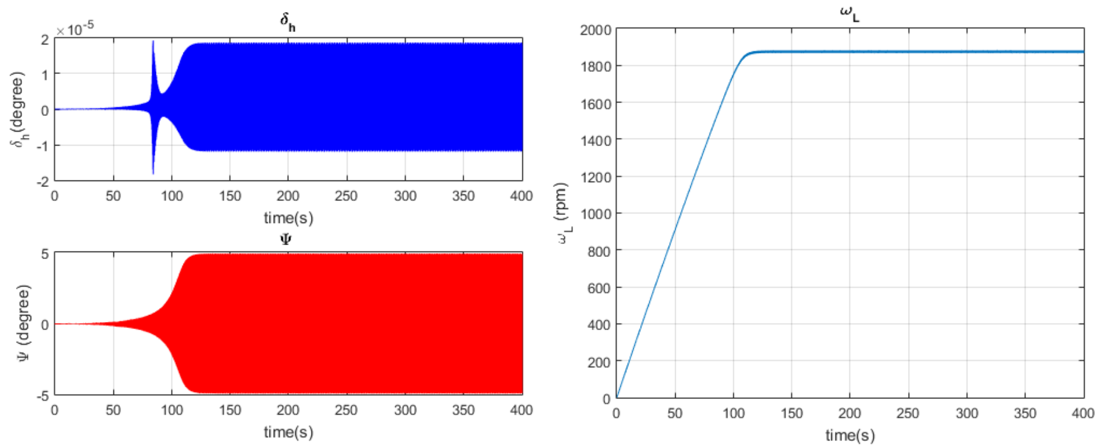

Figure 3.15 Subcritical Passage: $\delta_0 = 15°$

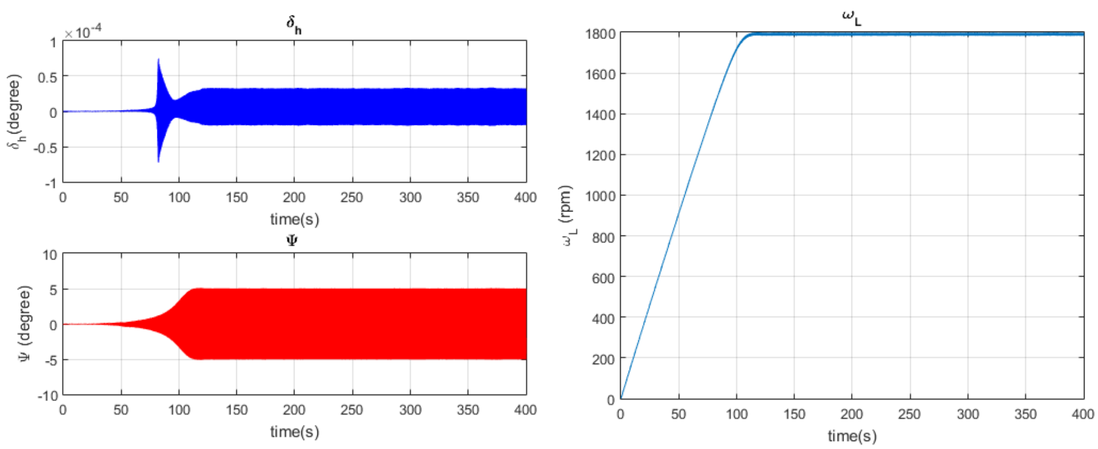

Figure 3.16 Subcritical Passage: $\delta_0 = 20°$

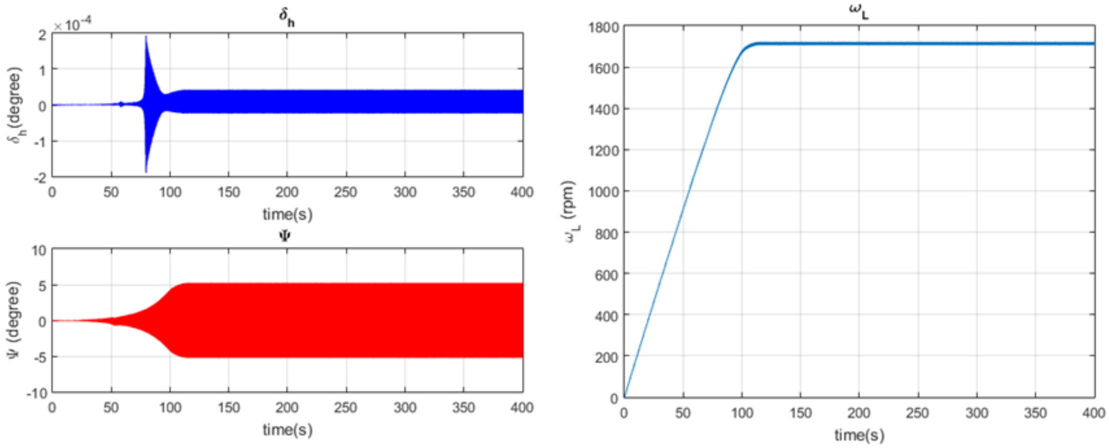

Figure 3.17 Subcritical Capture: $\delta_0 = 25°$

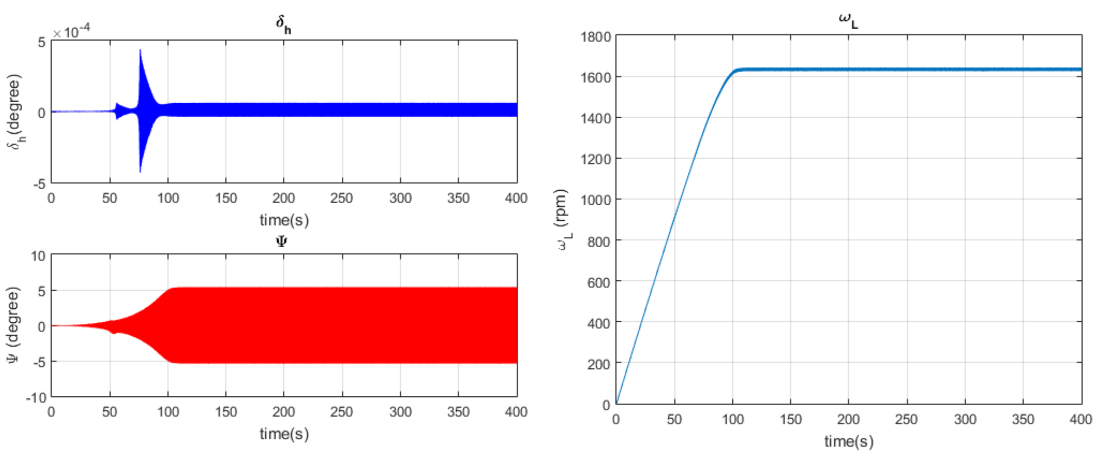

Figure 3.18 Subcritical Capture: $\delta_0 = 30°$

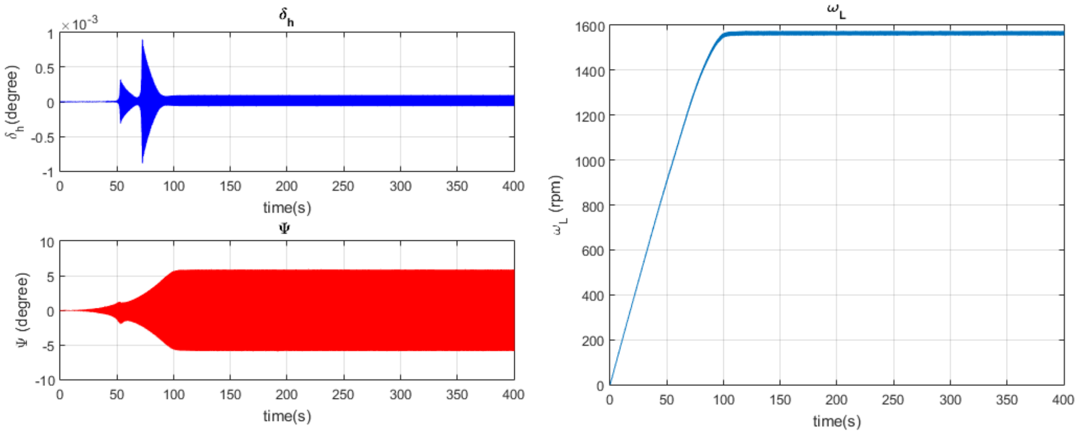

Figure 3.19 Subcritical Passage: $\delta_0 = 35°$

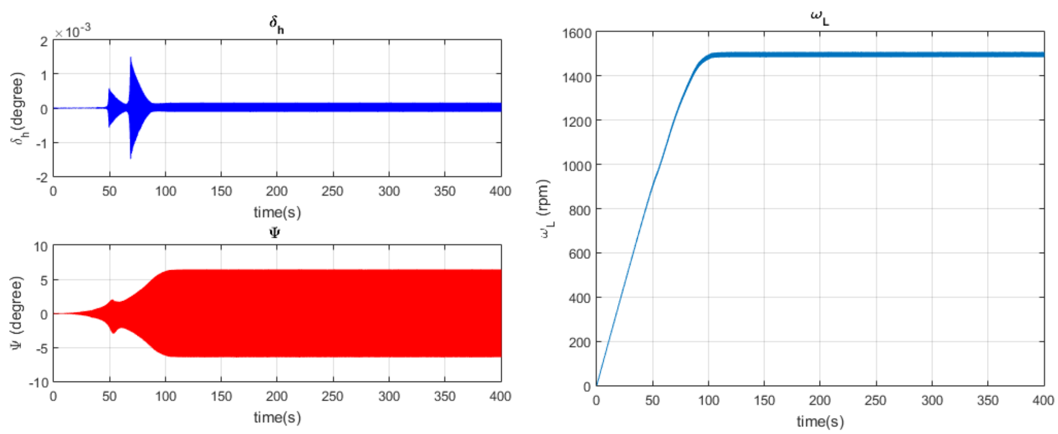

Figure 3.20 Subcritical Passage: $\delta_0 = 40°$

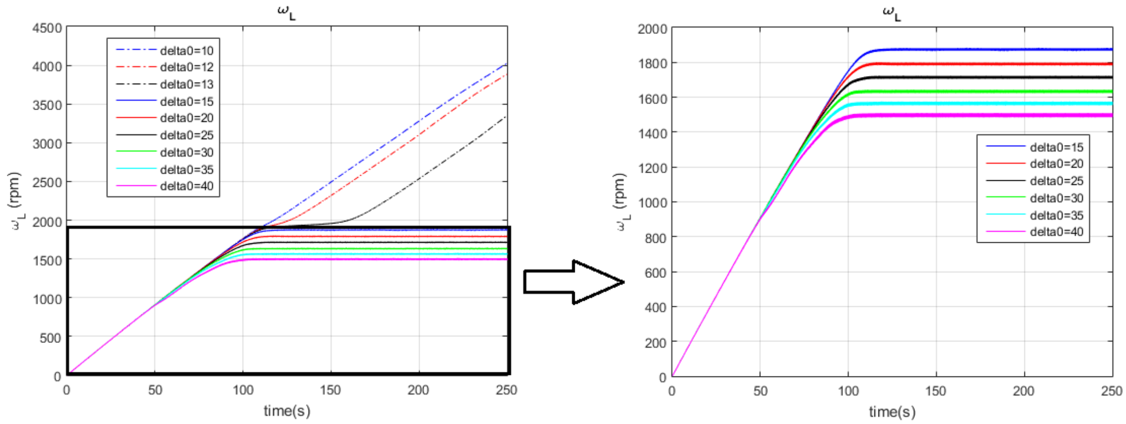

Figure 3.21 Subcritical Case: Rotating Speed Comparison: $\boldsymbol{\delta_0 = 10° \sim 40°}$

Then the second condition of load torque is determined by equation (3.4). Then the twist component is considered by determining the load torque constant as well that is proportional to the static angles. The constant load torque is determined by equation (3.4). The viscous load torque is not considered in this study since the viscous terms are too small by comparing to the static load torque. The input torque is determined in equation (3.6)

$$T_m = a(J_s + J_L) - T_{Lc} \tag{3.6}$$

Figure 3.22 to Figure 3.26 show the response of the perturbation dynamic misalignment angle, twist angle, and output speed as same as the previous simulation with viscous load torque. The static misalignment condition is set as $\delta_0 = 10°$. Figure 3.22 shows the result when the twist angle is near the region of 5°, the driveline shaft passage through the critical speed. Then when the twist angle is in the region of 10°, the capture phenomenon occurs in Figure 3.23.

Therefore, the results indicate that the large load torque causes the Sommerfeld effect in the small misalignment condition. Moreover, the 2° initial perturbation dynamic misalignment angle is defined. As we can see in the lateral deflection response in Figure 3.25, the lateral deflection motion is still stable under this simulation condition. furthermore, the rotating speed indicates the more significant lateral vibration motion slightly reduce the speed limit value. Last but not least, the difference between Figure 3.24 and Figure 3.25 is that the twist angle response in the latter one is in the larger twist level. Furthermore, the speed limit value is lower with a large twist angle in 12° than the one in the region of 10° that is illustrated in Figure 3.26. As the previous result shows that there is a critical misalignment angle which is the critical values that have an effect on the rotating speed whether captured or passaged.

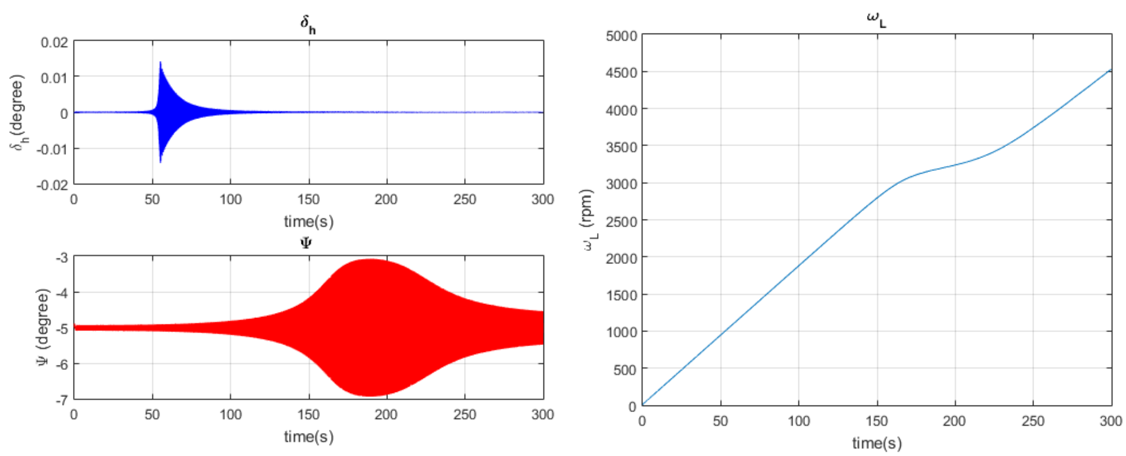

Figure 3.22 Rotating Speed passage the Resonance Region $\boldsymbol{\delta_0 = 10°, \varphi_0 = 5°}$

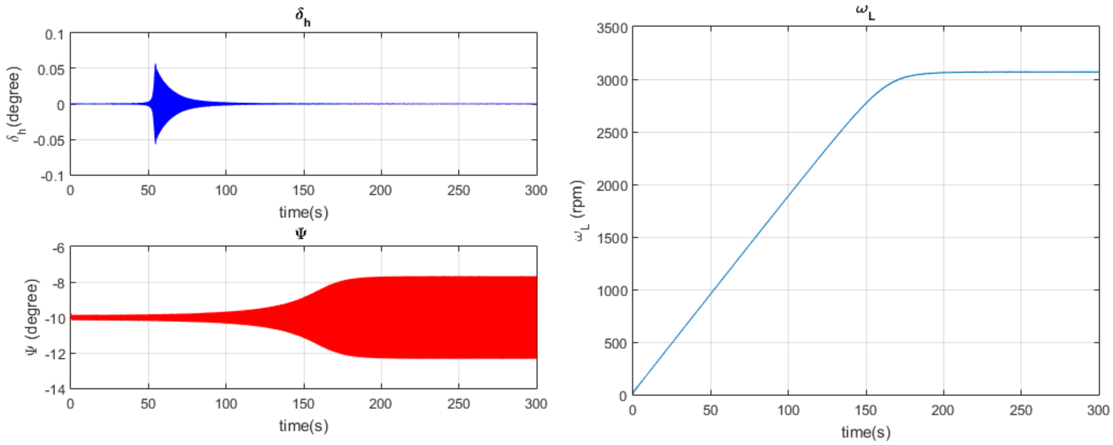

Figure 3.23 Rotating Speed Capture at the Resonance Region $\delta_0 = 10°$, $\varphi_0 = 10°$

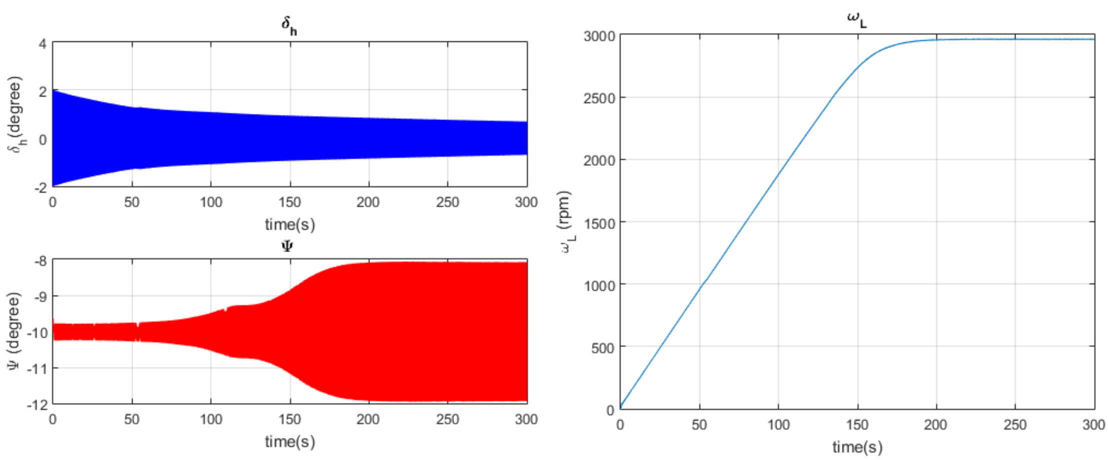

Figure 3.24 Rotating Speed Capture: $\varphi_0 = 10°, \delta_1(0) = 12°$

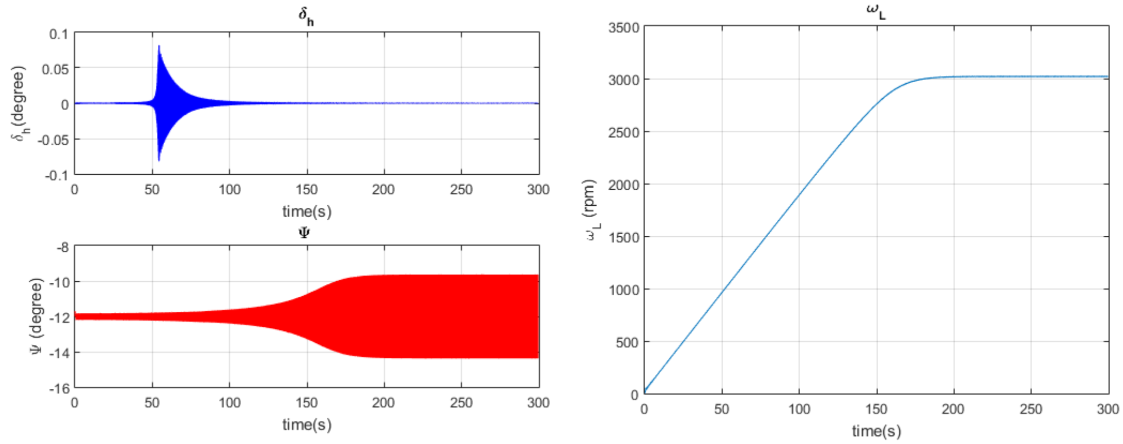

Figure 3.25 Rotating Speed Capture at the Resonance Region $\delta_0 = 10°,\ \varphi_0 = 12°$

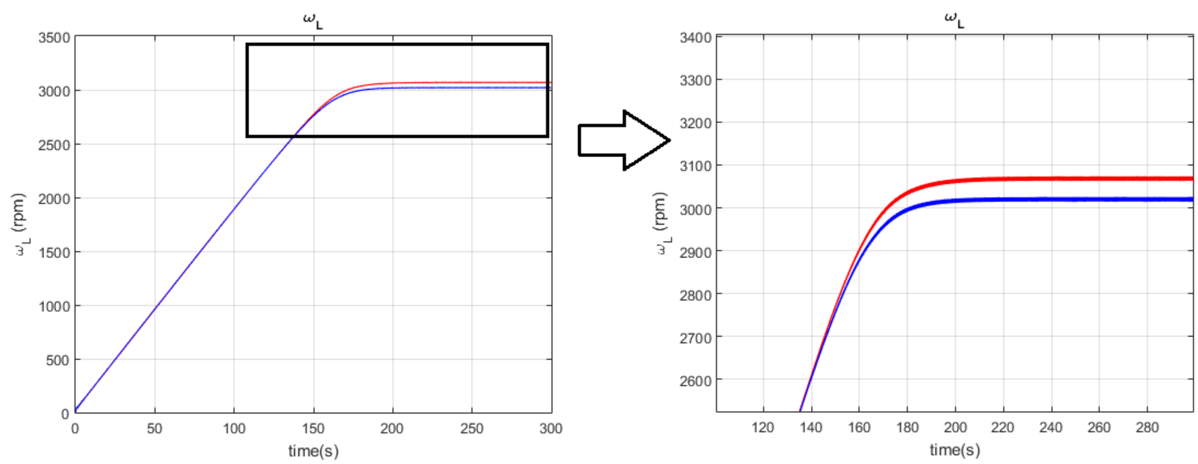

Figure 3.26 Rotating Speed Comparison $\delta_0 = 10°,\ \varphi_0 = 10°\ \&\ 12°$

3.2.2 Critical Static Misalignment Angle

The accurate critical static misalignment angle is determined by exploring the rate of change of the rotating speed slope. The critical static misalignment angle can be measured from the higher figure corresponding to the critical time when the slope of the acceleration of the rotating speed reaches the maximum value. The acceleration sequence of the rotating speed is defined in equation (3.7), and the corresponding time sequence is determined in equation (3.8).

$$a_c(i) = \frac{\Omega(i) - \Omega(i-1)}{t(i) - t(i-1)} \qquad i = 2,3,\dots,n \tag{3.7}$$

$$t_c(i) = t(i-1) + \frac{t(i) - t(i-1)}{2} \qquad i = 2,3,\dots,n \tag{3.8}$$

With the determined slope sequence of the acceleration as in equation (3.9) and (3.10).

$$s_a(i) = \frac{a_c(i) - a_c(i-1)}{t_c(i) - t_c(i-1)} \qquad i = 2,3,\dots,n \tag{3.9}$$

$$t_s(i) = t_c(i-1) + \frac{t_c(i) - t_c(i-1)}{2} \qquad i = 2,3,\dots,n \tag{3.10}$$

The approximate critical time that is used to define the critical static misalignment angle is determined by the s_a sequence reaches the maximum value. Although this method is no guarantee for the accurate critical misalignment value, it is more accurate than the manual determination from the plot directly. Figure 3.27 and Figure 3.28 show the critical time value when the static misalignment angle reaches the critical value.

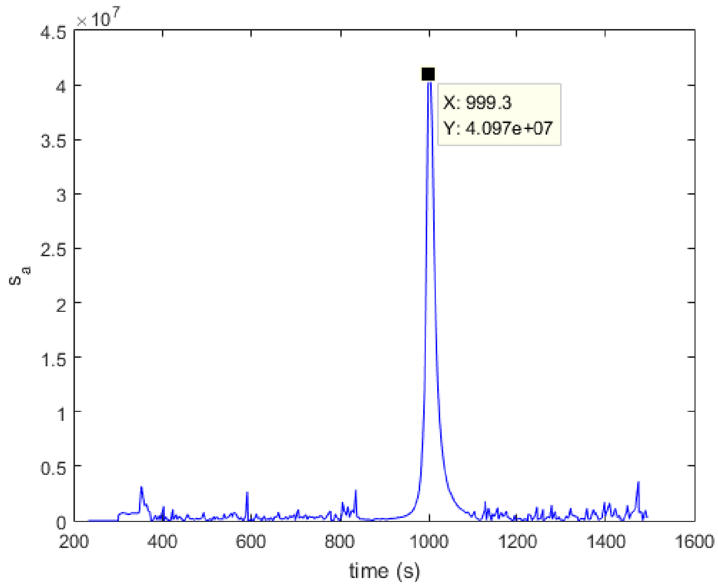

Figure 3.27 Subcritical case: Approximate Critical Time (D_g)

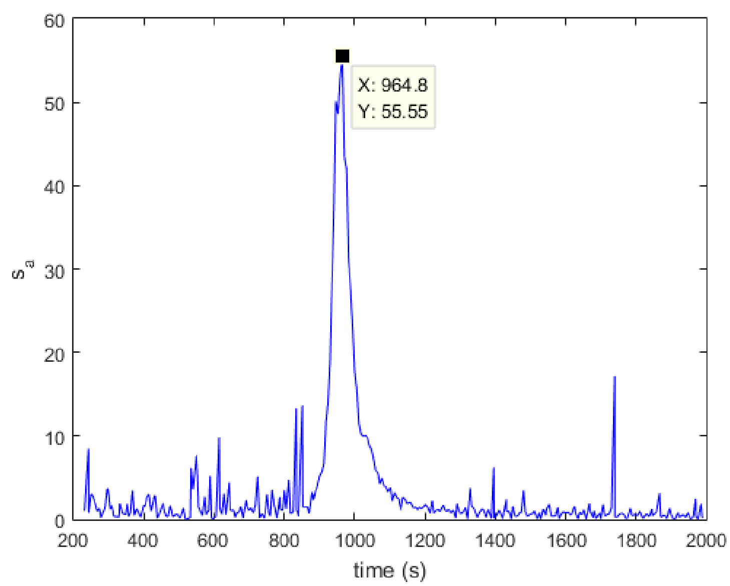

Figure 3.28 Supercritical Case: Approximate Critical Time (D_g)

Figure 3.29 and Figure 3.30 indicate that there is a critical static misalignment angle where the rotating speed is captured or get through. The region of the static misalignment angle locates in the beginning of the torsional natural frequencies curve, where the slop and the difference of the curves are close to zero. Then the rotating speed of the starts to be captured when the static misalignment angles are above the safe region. The critical static misalignment angle is close to 11^{o} with the parameters shown in Table 3.1

Figure 3.29 shows the result of the supercritical case, and Figure 3.30 is the result of the subcritical case. The initial static misalignment angle is set as 15^{o} with a decreasing rate as 0.00005^{o} which is illustrated in the above figures. Then the below figure shows the output speed. As the below figures illustrate, the rotating speed is captured as the results in the previous section. The rotating speed is increasing gradually corresponds to the gradually decreasing static misalignment angle. The effect of the load viscous coefficient is also explored in the section. The critical speed varies when the viscous load torque is twice and third times of the original value. Moreover, the critical static misalignment angle corresponding to the critical speed passaging the resonance speed region reduced. The figures illustrate that the larger the load viscous coefficient value is, the smaller the critical static misalignment angle is. It is proven that the load torque would reduce the critical static misalignment angle value.

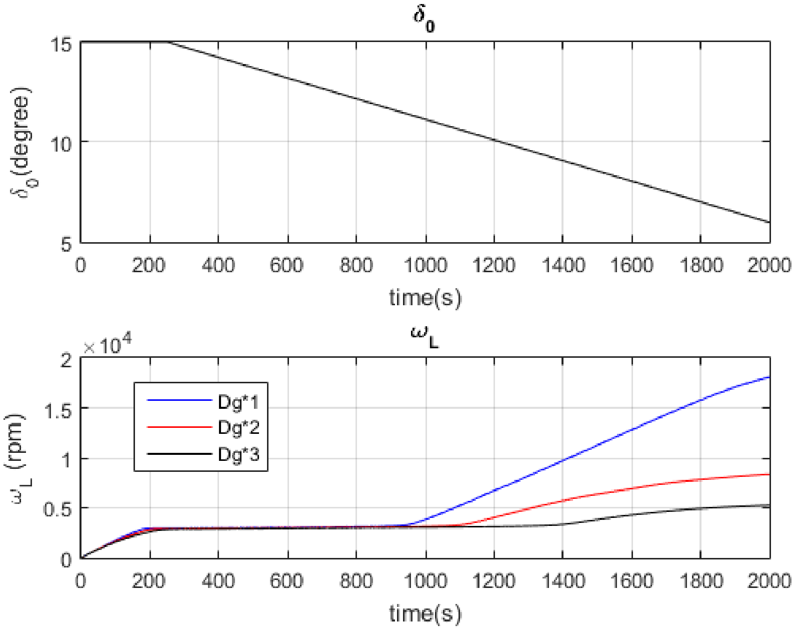

Figure 3.29 Supercritical Case: Approximate critical δ_0

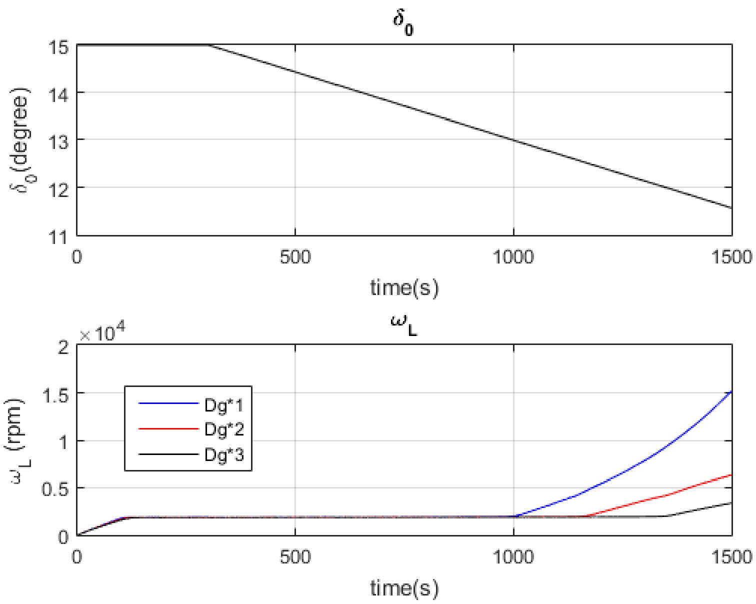

Figure 3.30 Subcritical Case: Approximate critical δ_0

In other word, the driveline system in the small misalignment condition will consequent in the Sommerfeld effect with large load torque. Referring to the approximate critical time obtained from Figure 3.27 and Figure 3.28, the corresponding critical misalignment angles are 13° and 11.32° from Figure 3.29 and Figure 3.30 for the original D_g condition. The approximate critical static misalignment angles are listed in Table 3.2.

When the approximate critical static misalignment angle is close to 11.32°, which matches the simulation result in Figure 3.3 that the passage phenomenon is observed with the 11° static misalignment condition. The similar method can be used to obtain the critical value from Figure 3.30 that indicates the approximate static misalignment angle is extremely close to 13°, which also matches the passage phenomenon in Figure 3.14. The plot of Table 3.2 is shown in Figure 3.31. Figure 3.31 illustrates that for each case with the different D_g value, the speed capture phenomenon will not be observed when the static misalignment angles δ_0 are not above the curve of the critical misalignment condition.

Table 3.2 Approximate Critical Static Misalignment Angles

	Supercritical	**Subcritical**
Viscous Coefficient	Critical δ_0 (°)	Critical δ_0 (°)
D_g	11.32	13
$2D_g$	10.48	12.51
$3D_g$	9.07	11.99

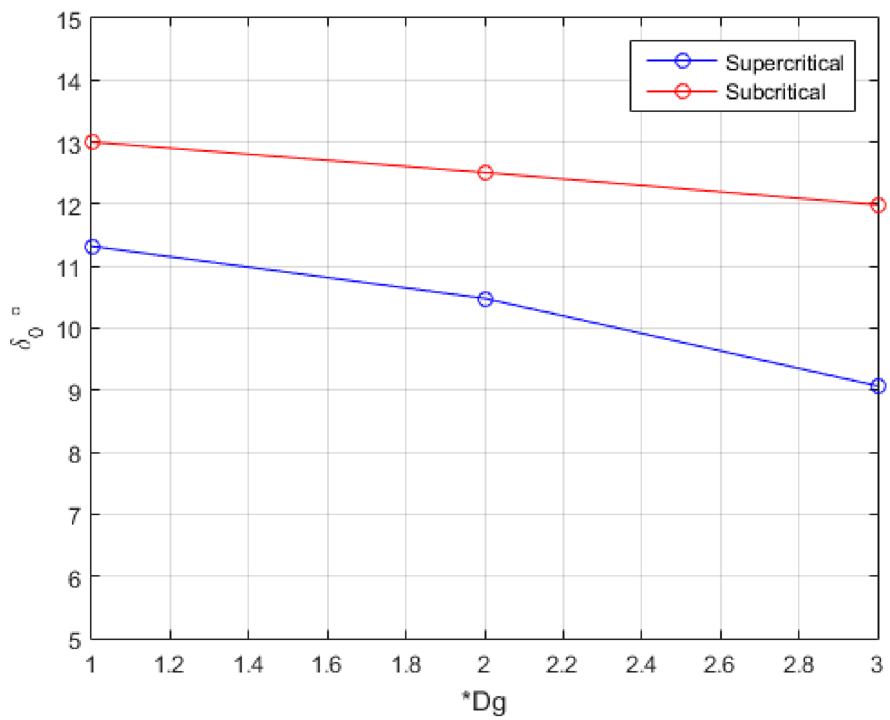

Figure 3.31: Approximate Critical δ_0 vs nD_g

3.2.3 Response Analysis in Frequency Domain

The previous section indicates that the speed limits occurs when the static misalignment angles are equal or larger than 15º. Then the detailed exploring on the results with speed limit is required. The short-time fast Fourier theory is applied to analyze the critical frequencies from the responses in time. Figure 3.32 to Figure 3.33 illustrate the critical frequency keeps ramping up when the rotating speed of the shaft is spinning up. When the rotating speed reaches the speed limit, the critical frequency remains constant instead of ramping up, which are observed from Figure 3.34 to Figure 3.39 as the supercritical case. Furthermore, there are the apparent both lateral critical frequency and torsional critical frequency in the lateral response presented in frequency domain, however, no apparent lateral critical frequencies are observed in torsional response for the supercritical case. If turning back to the time domain responses of supercritical case, when the speed is passing through the torsional critical frequency, the lateral response does not converge to equivalent range even though the lateral critical frequency is below the current speed. Therefore, there is a weak coupling of the torsional motion to lateral motion under small misalignment condition even though there is no apparent resonance frequency shown in spectrograms.

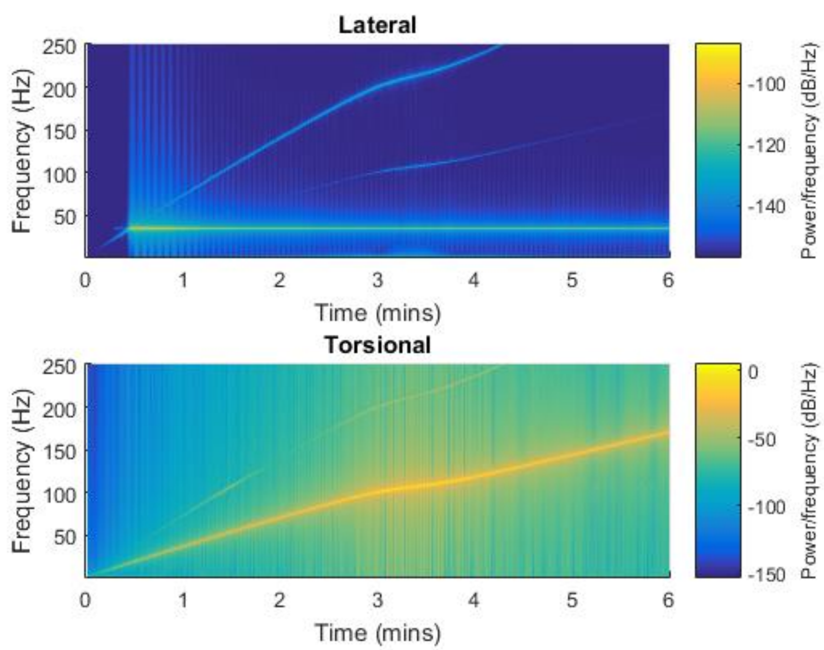

Figure 3.32 Spectrogram Supercritical Passage: $\delta_0 = 10°$

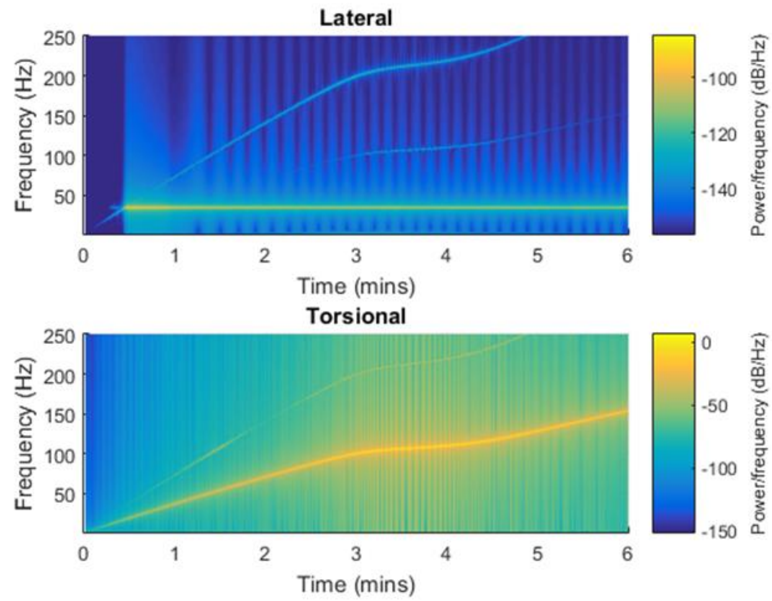

Figure 3.33 Spectrogram Supercritical Passage: $\delta_0 = 11°$

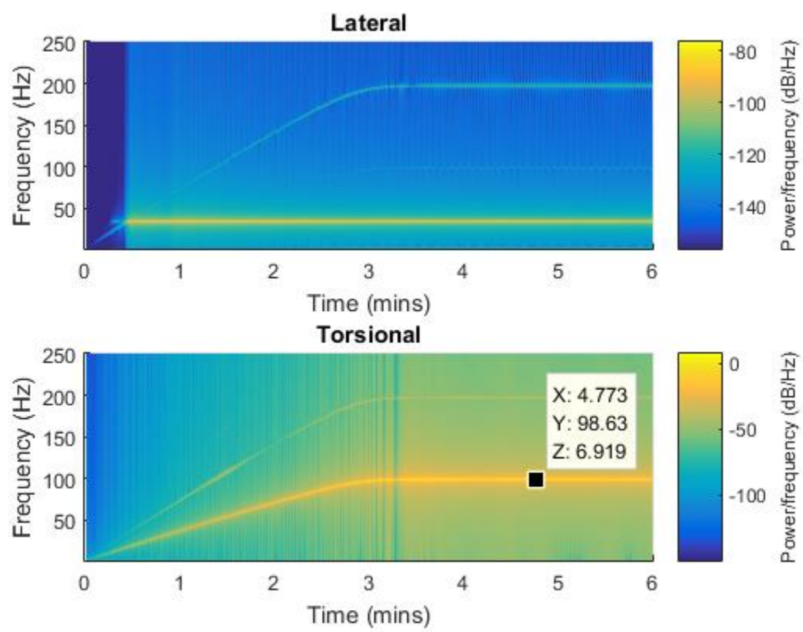

Figure 3.34 Spectrogram Supercritical Capture: $\delta_0 = 15°$

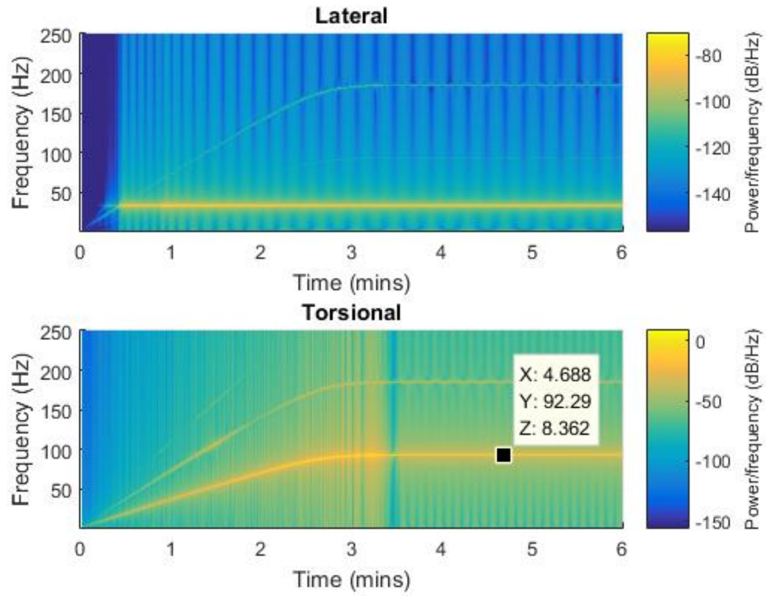

Figure 3.35 Spectrogram Supercritical Capture: $\delta_0 = 20°$

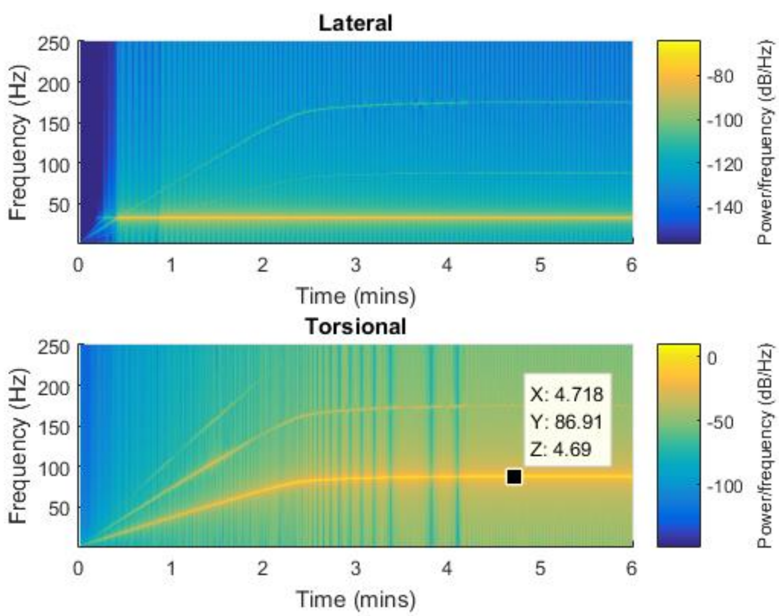

Figure 3.36 Spectrogram Supercritical Capture: $\delta_0 = 25°$

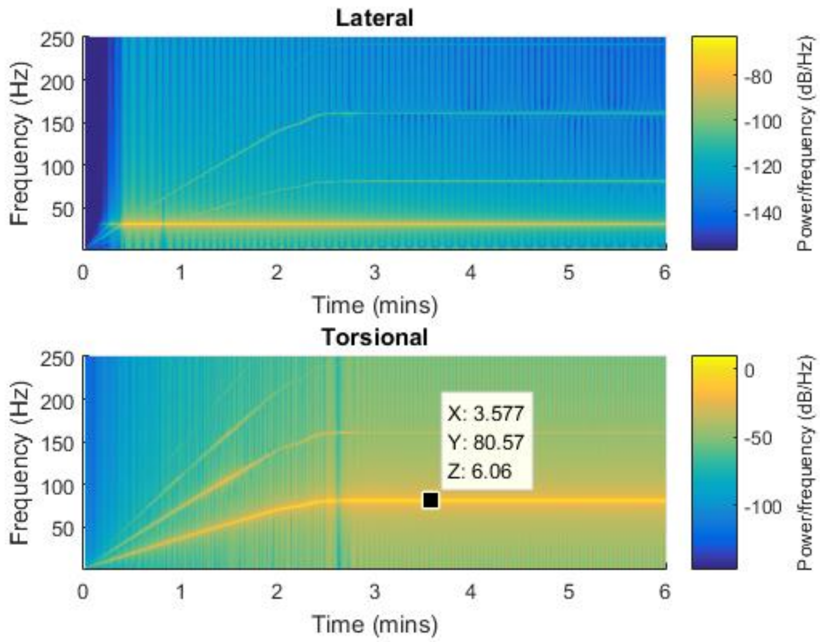

Figure 3.37 Spectrogram Supercritical Passage: $\delta_0 = 30°$

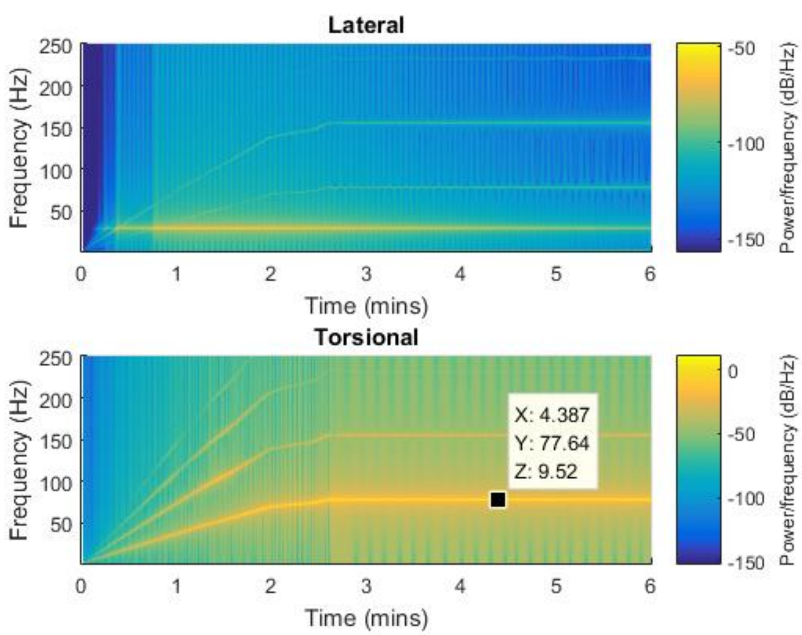

Figure 3.38 Spectrogram Supercritical Passage: $\delta_0 = 35°$

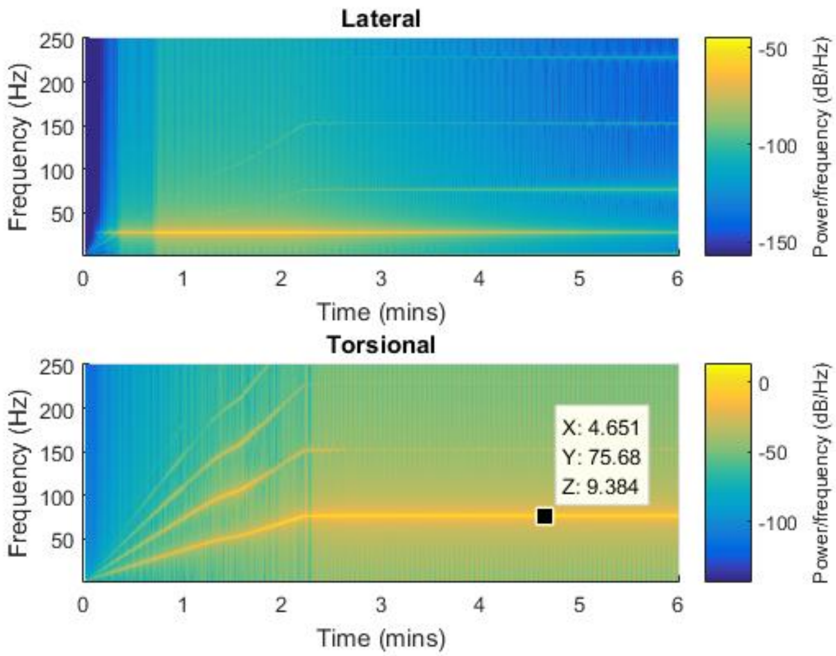

Figure 3.39 Spectrogram Supercritical Passage: $\delta_0 = 40°$

Figure 3.40 and Figure 3.41 illustrate the critical frequency keeps ramping up when the rotating speed of the shaft is spinning up. When the rotating speed reaches the speed limit, the critical frequency remains constant instead of ramping up, which are observed from Figure 3.42 to Figure 3.46 as the subcritical case.

As the spectrograms show, there is a response excitation when the second torsional critical frequency passes through the lateral critical frequency. Moreover, the lateral response becomes in the limited cycle when the Sommerfeld effect occurs since the second torsional critical frequency is closed to the lateral critical frequency. The time domain responses in the previous section have shown the excitations.

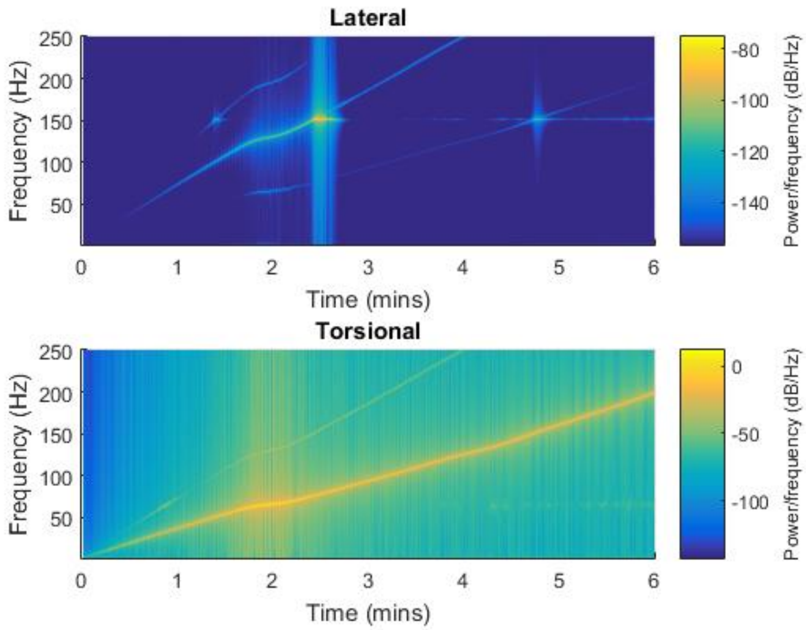

Figure 3.40 Spectrogram Subcritical Passage: $\delta_0 = 12°$

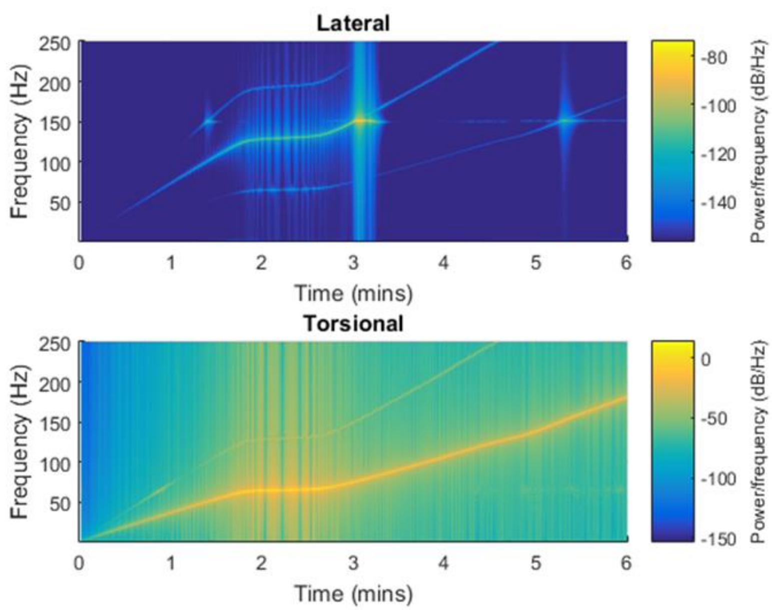

Figure 3.41 Spectrogram Subcritical Passage: $\delta_0 = 13°$

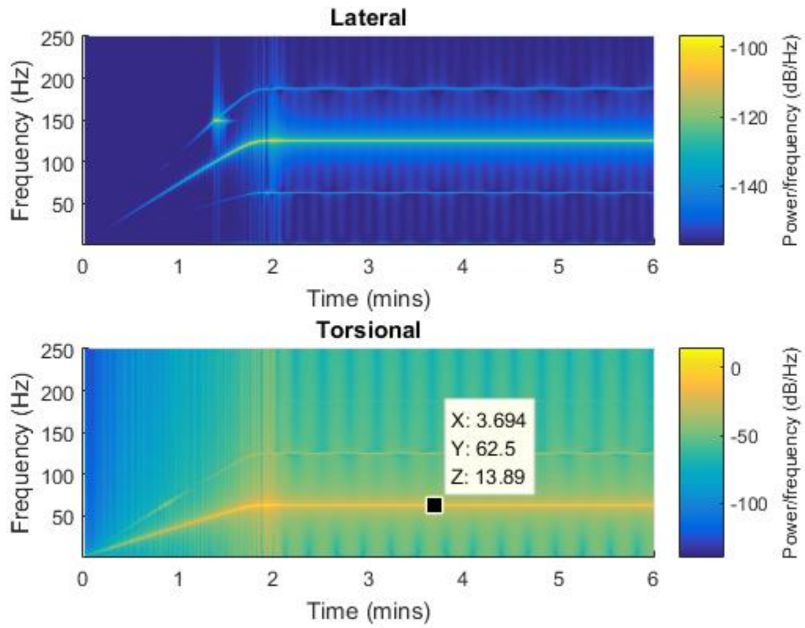

Figure 3.42 Spectrogram Subcritical Capture: $\delta_0 = 15°$

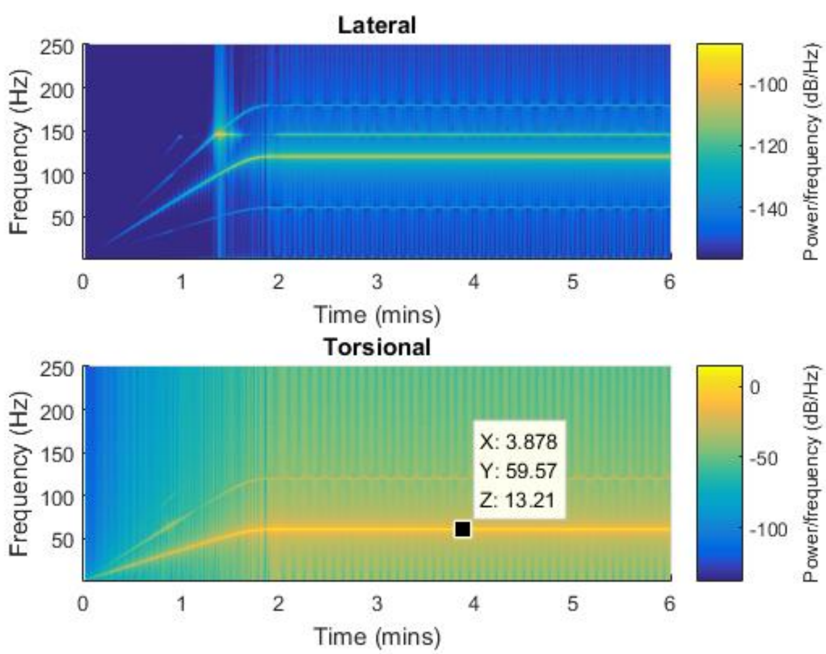

Figure 3.43 Spectrogram Subcritical Capture: $\delta_0 = 20°$

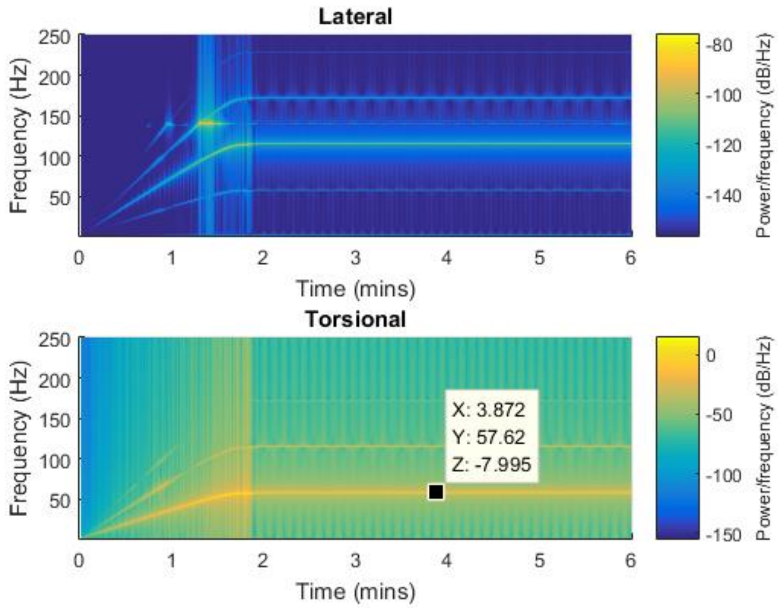

Figure 3.44 Spectrogram Subcritical Capture: $\delta_0 = 25°$

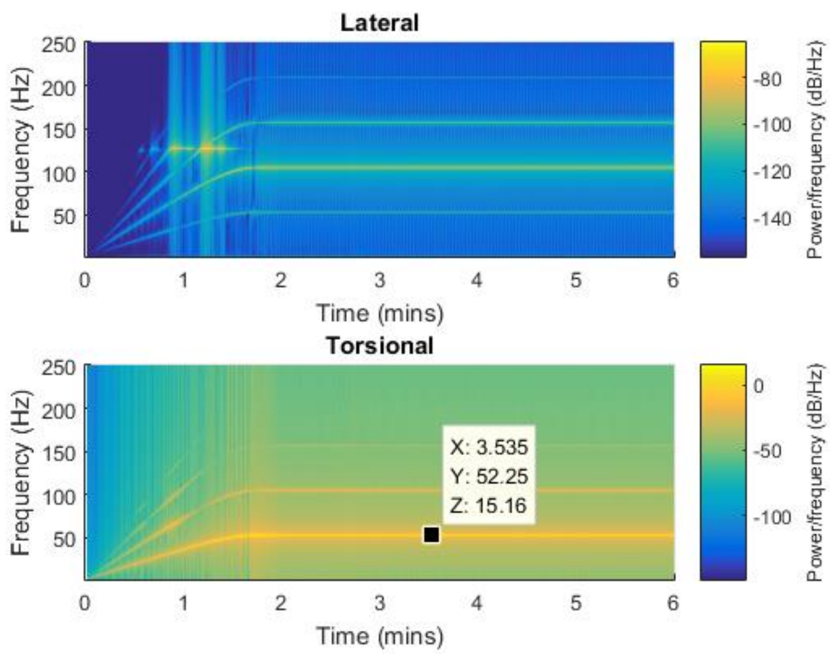

Figure 3.45 Spectrogram Subcritical Capture: $\delta_0 = 35°$

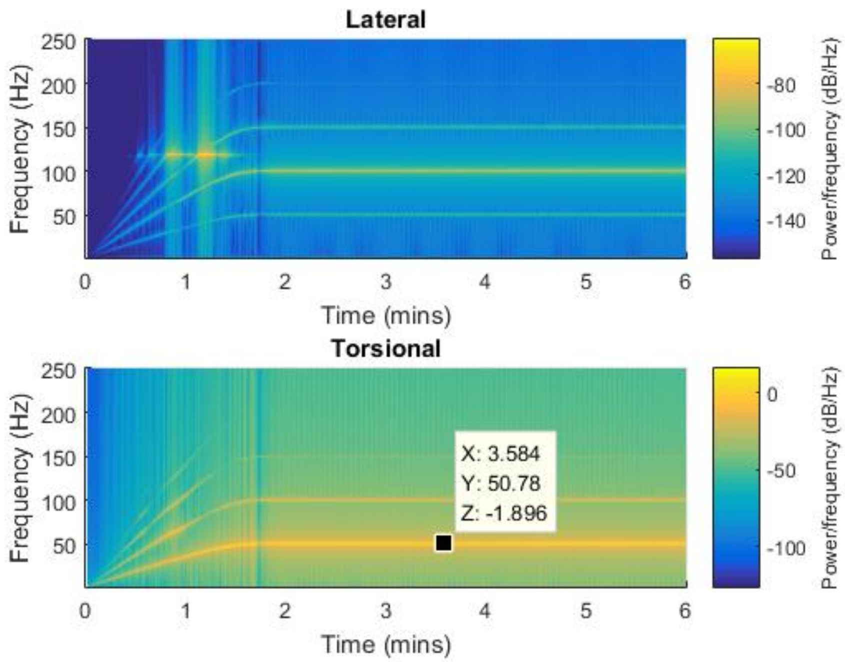

Figure 3.46 Spectrogram Subcritical Capture: $\delta_0 = 40°$

Referring to the figures in frequency domain, the larger static misalignment angle is, the more dominating the high critical frequency term becomes in subcritical case. Furthermore, the weak lateral critical frequency is observed in the torsional response under large static misalignment condition. Referring to Table 3.3, both the lateral and torsional critical frequencies keep gradually decreasing corresponding to the slight increase of the static misalignment angle. This conclusion satisfies that the rotating speed limit is lower corresponding to the larger misalignment condition in the time domain.

Table 3.3 1st Lateral and Torsional Critical Frequencies with Different δ_0

	Supercritical		Subcritical	
Static misalignment angles δ_0 (^{o})	1st lateral peak f_n (Hz)	1st torsional peak f_t (Hz)	1st torsional peak f_t (Hz)	1st lateral peak f_n (Hz)
15	33.69	98.63	62.5	148.4
20	32.71	92.29	59.57	145
25	31.25	86.91	57.62	139.2
30	29.79	80.57	54.69	133.8
35	28.32	77.64	52.25	126
40	26.37	75.68	50.78	118.2

The fundamental torsional critical frequency under capture phenomenon in this section can be calculated via equation (3.11)

$$f_t = \begin{cases} 2\dot{\phi}_L & 0 \le t \le t_c \\ 2\dot{\phi}_c & t > t_c \end{cases} \tag{3.11}$$

Where $\dot{\phi}_L$ is the rotating speed of output shaft before capture phenomenon, $\dot{\phi}_c$ is the captured rotating speed, and t_c is the time when the capture happens that can be obtained from the previous section.

3.3 Simulation with Constant Torque Input: 2-DOF

3.3.1 Time Domain Response

As the same input value and the system parameters are used in the previous section, the simulation result of the reduced 2 DOF model is shown in this section for both case I and case II. There is no lateral natural frequency in the 2-DOF model due to the zero lateral motion assumption, therefore, the case I parameters are as same as the supercritical case, and so on, such as case II parameters are as same as the subcritical case. All results from Figure 3.47 to Figure 3.60 show the response of the 2-DOF driveline model with the constant torque input. The similar results are shown in this section with the results of the 3-DOF model. there is a critical static misalignment angle determines whether the Sommerfeld effect is observed. The concentration is placed on the difference between the two models. As the results show that the responses and speed limit value are similar between two models under small static misalignment conditions. The only difference that is shown in the results of the 2-DOF and 3-DOF model is that the speed limit value of the 2-DOF model is lower than the value of the 3-DOF model. This phenomenon is more manifestly under the large static misalignment condition.

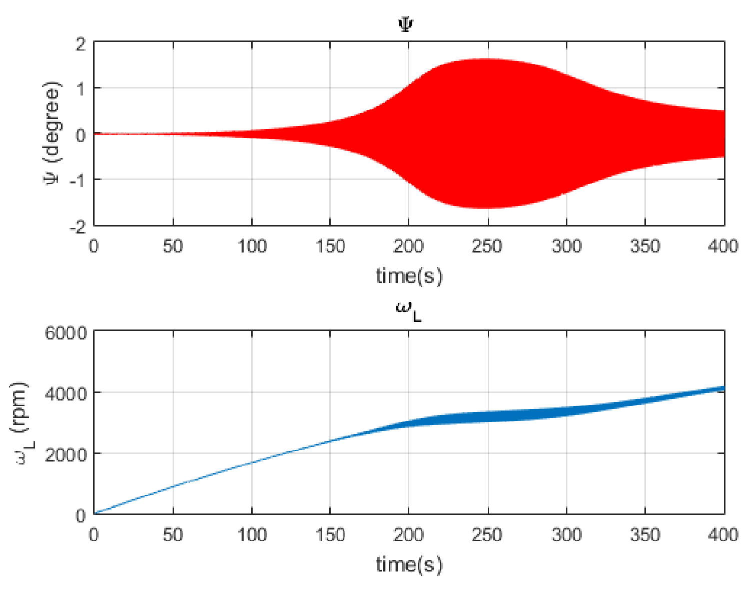

Figure 3.47 2-DOF Case I Passage: $\delta_0 = 10°$

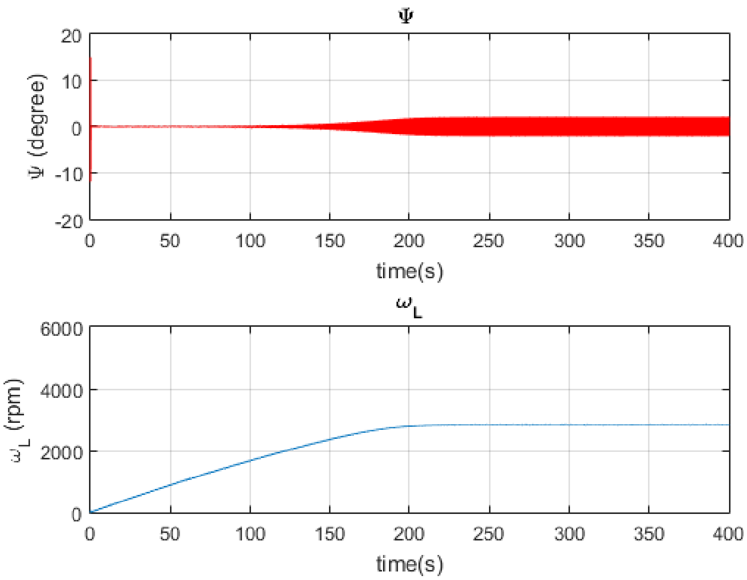

Figure 3.48 2-DOF Case I Capture: $\delta_0 = 15°$

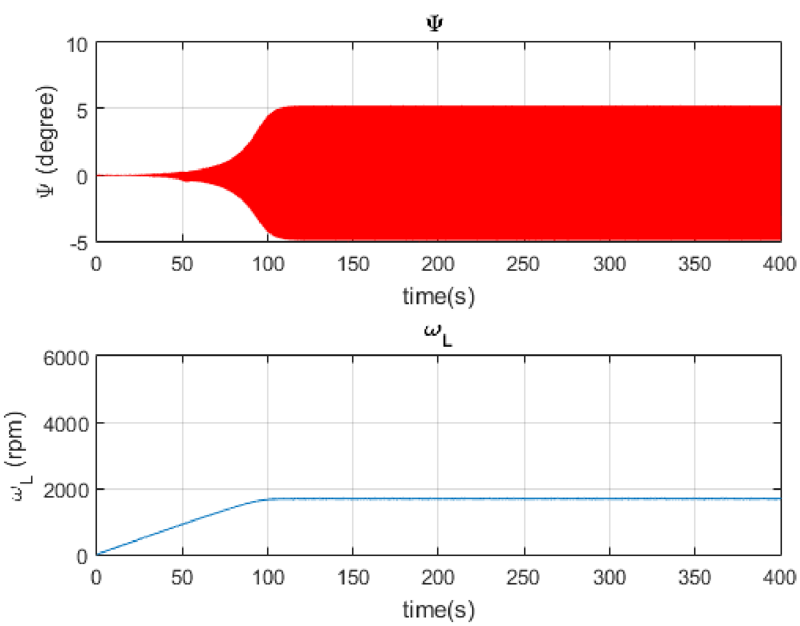

Figure 3.49 2-DOF Case I Capture: $\delta_0 = 20°$

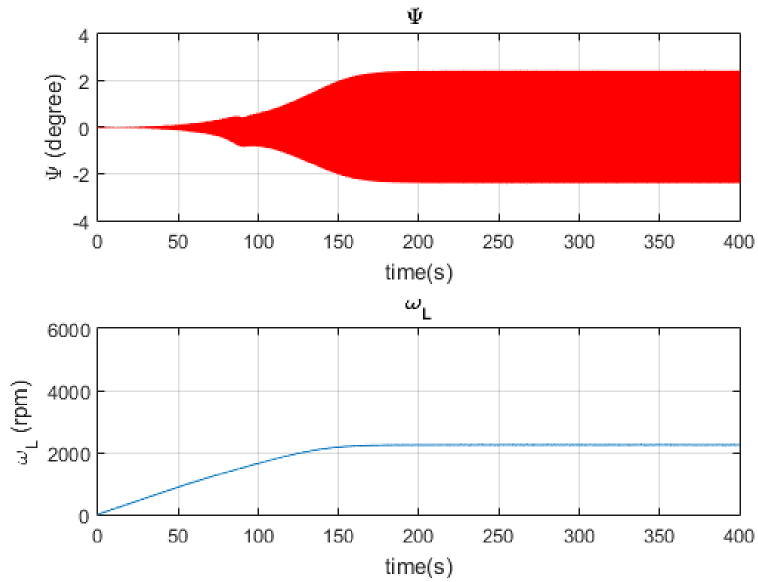

Figure 3.50 2-DOF Case I Capture: $\delta_0 = 25°$

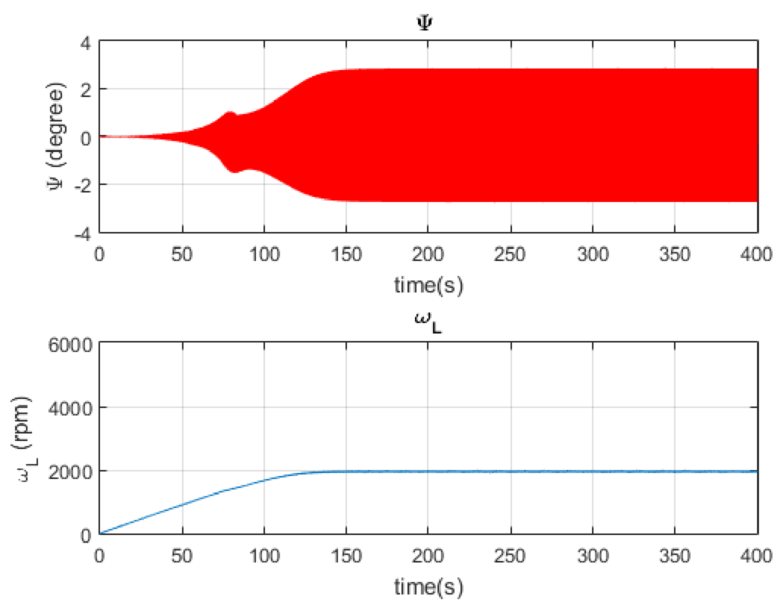

Figure 3.51 2-DOF Case I Capture: $\delta_0 = 30°$

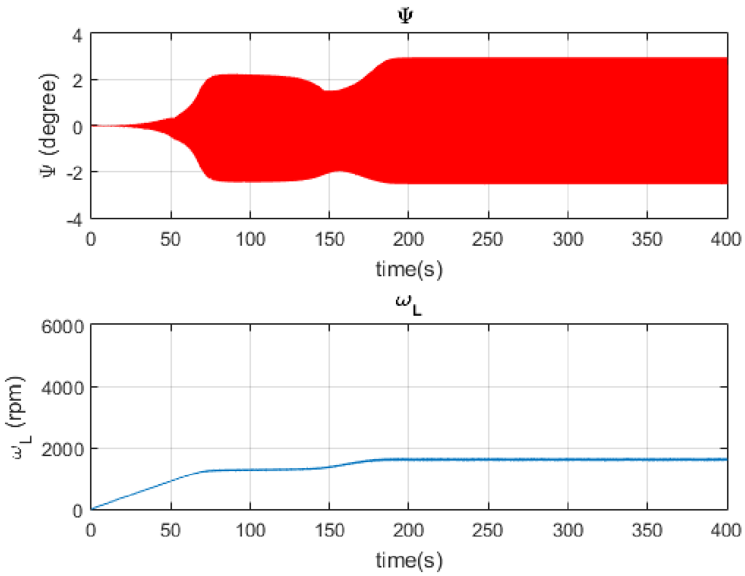

Figure 3.52 2-DOF Case I Capture: $\delta_0 = 35°$

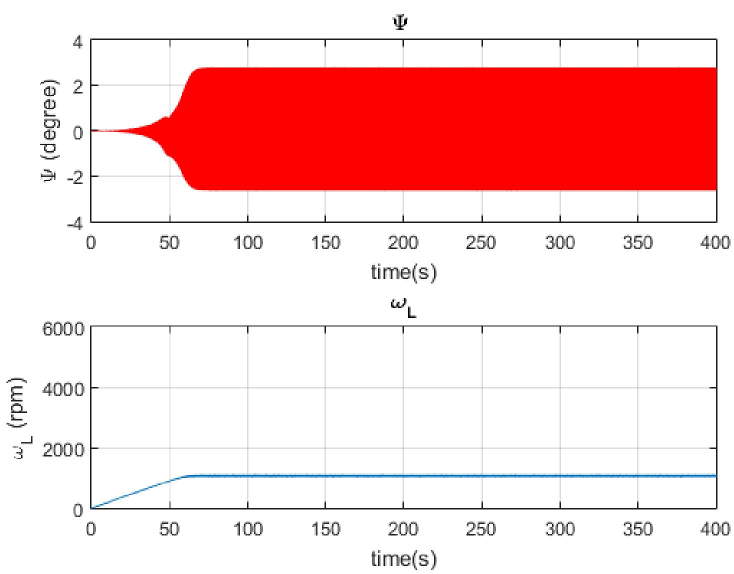

Figure 3.53 2-DOF Case I Capture: $\delta_0 = 40°$

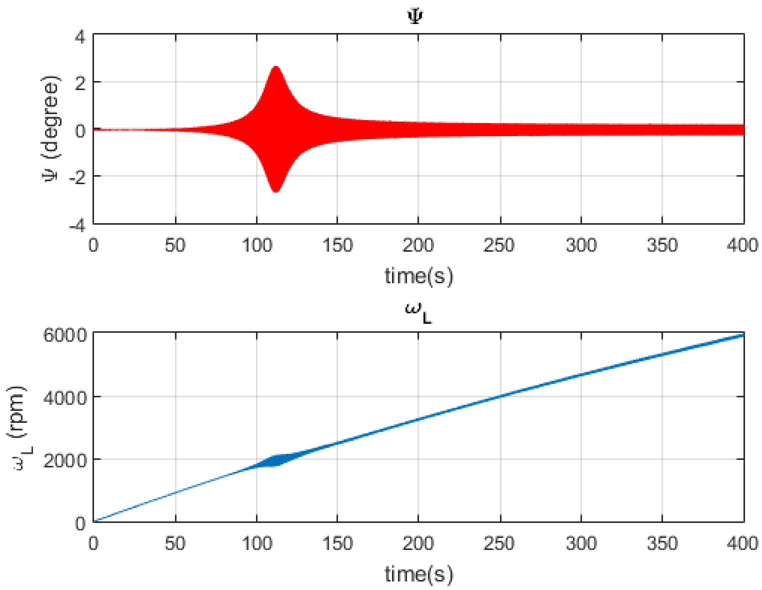

Figure 3.54 2-DOF Case II Passage: $\delta_0 = 10°$

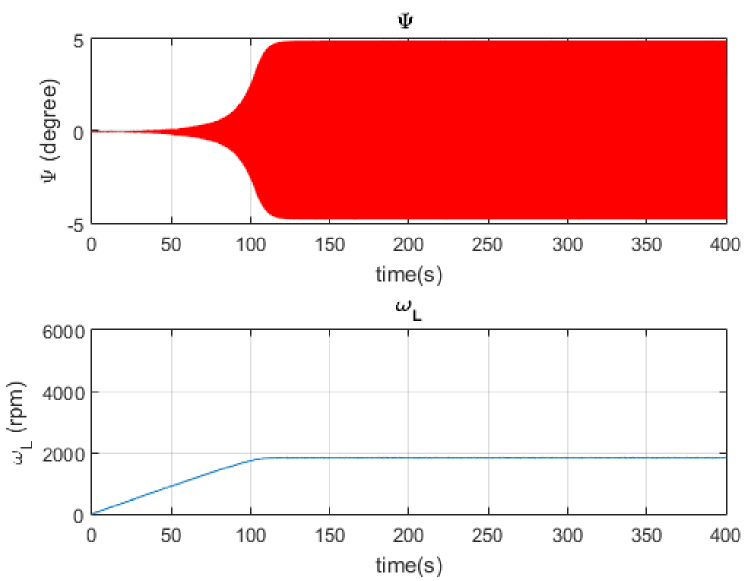

Figure 3.55 2-DOF Case II Capture: $\delta_0 = 15°$

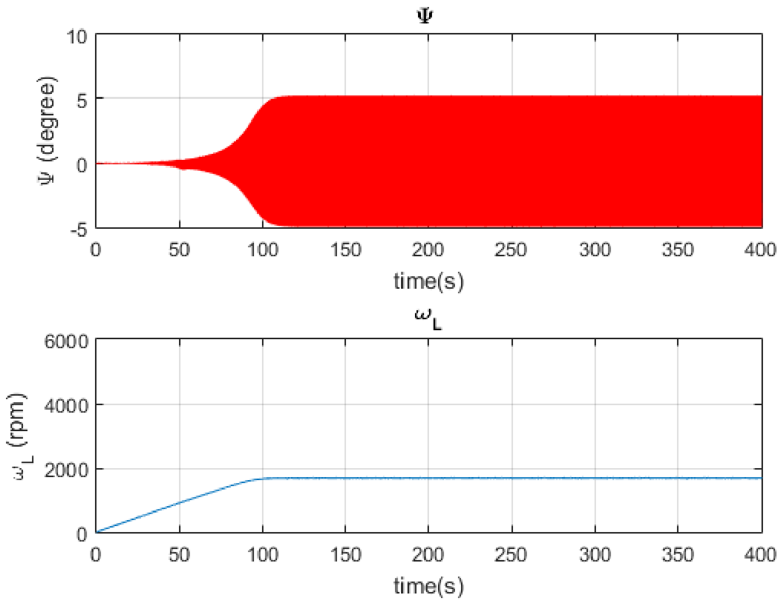

Figure 3.56 2-DOF Case II Capture: $\delta_0 = 20°$

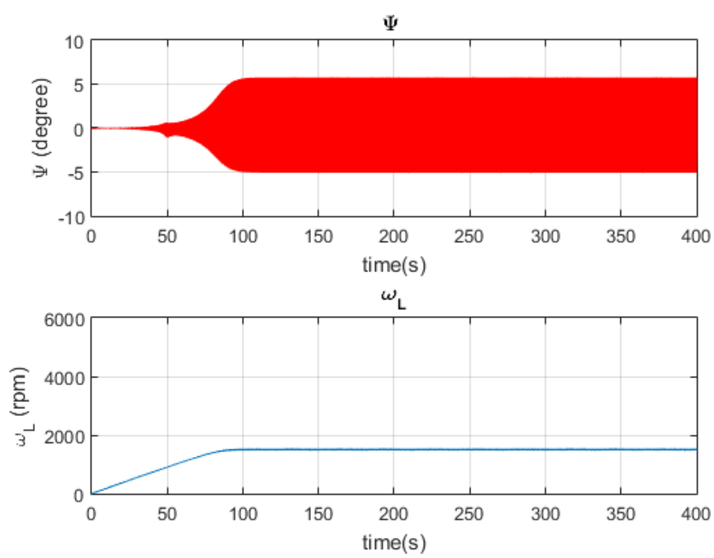

Figure 3.57 2-DOF Case II Capture: $\delta_0 = 25°$

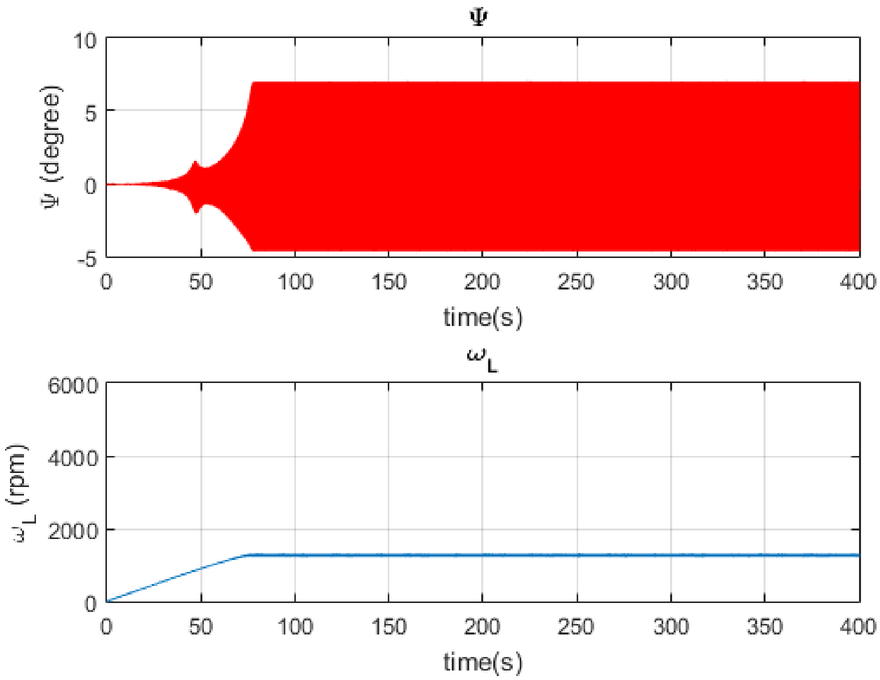

Figure 3.58 2-DOF Case II Capture: $\delta_0 = 30°$

However, the difference is significant when the static misalignment angle is set at 35º and 40º. Referring to the comparison of Figure 3.19 and Figure 3.59, and the comparison of Figure 3.20 as the subcritical case and Figure 3.60 as case II, there is the obvious unstable and phenomenon in the rotating speed response. Moreover, not only the speed limit value is marginally lower than the values of the 3-DOF model, but more vibration and instability are observed as well from Figure 3.59 and Figure 3.60 comparing to the 3-DOF model results in subcritical case. This is fascinating to notice that the lateral movement of the driveline system stabilizing the rotating speed and improve the speed limit level.

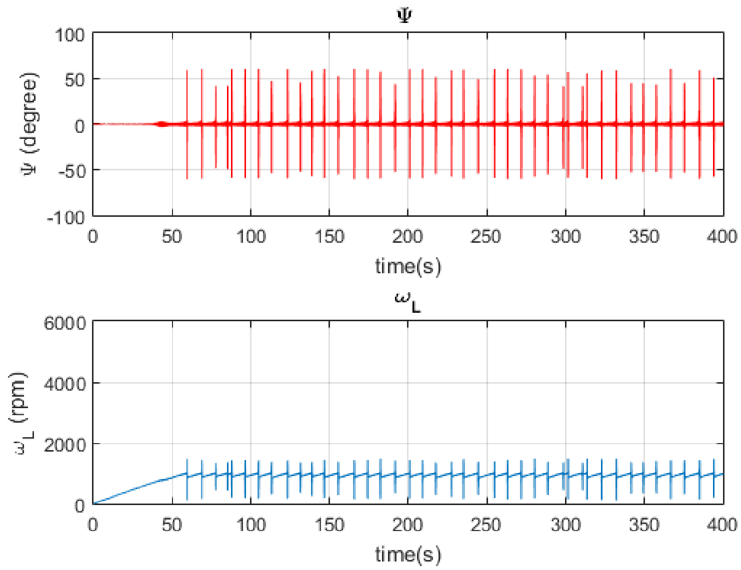

Figure 3.59 2-DOF Case II Capture: $\delta_0 = 35°$

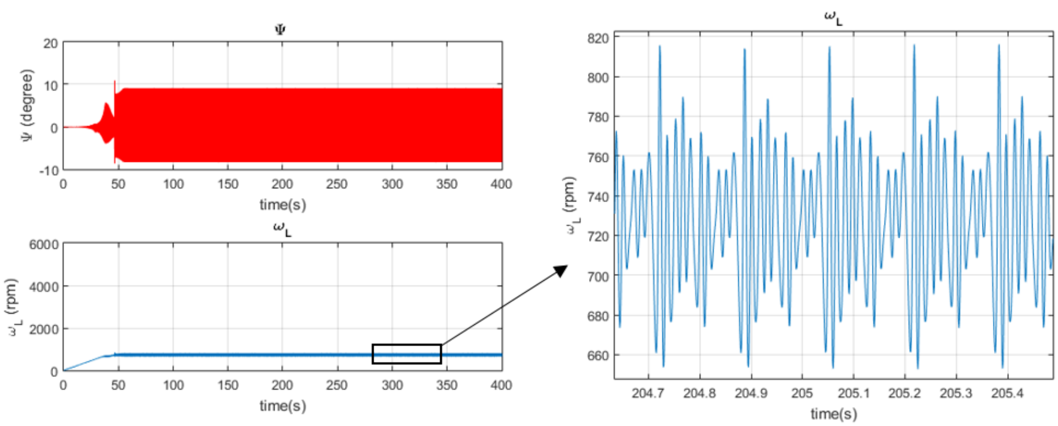

Figure 3.60 2-DOF Case II Capture: $\delta_0 = 40°$

The lateral oscillation stabilizing the torsional vibrations, which indicates the coupling between the lateral and torsional motion in the nonlinear model.

3.3.3 Response Analysis in Frequency Domain

Spectrograms from Figure 3.61 to Figure 3.72 show the critical frequencies in frequency domain. Only the results involving the Sommerfeld effect are explored in this section due to the purpose of this section is to obtain the critical frequencies of the 2-DOF model and comparing them with the results of the 3-DOF model. It is easy to obtain the critical frequencies from the results under the small static misalignment condition.

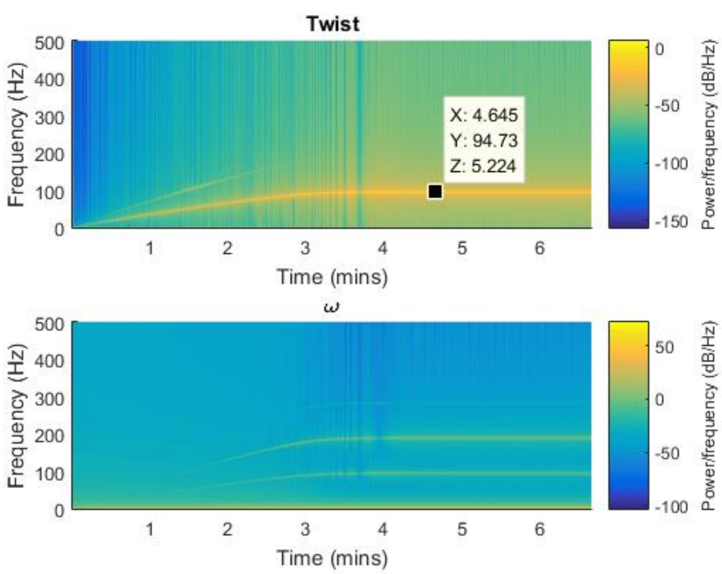

Figure 3.61 Spectrogram Case I Capture: $\delta_0 = 15°$

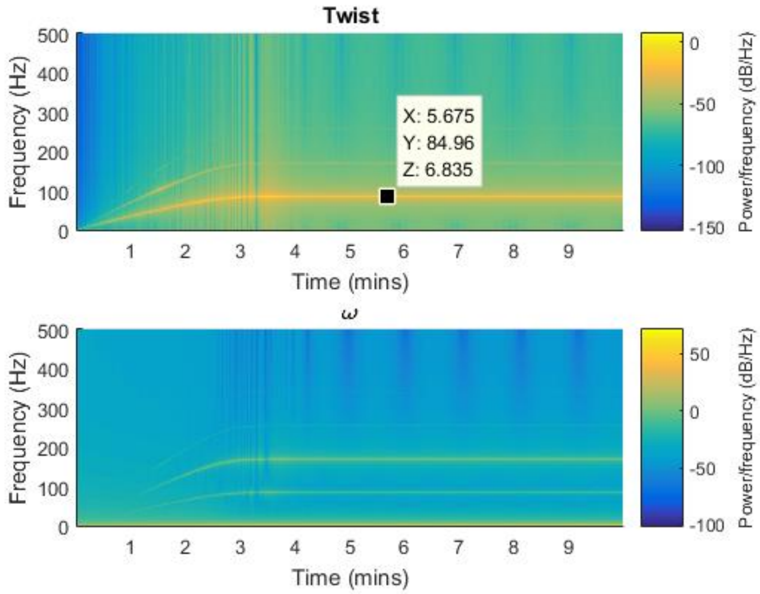

Figure 3.62 Spectrogram Case I Capture: $\delta_0 = 20°$

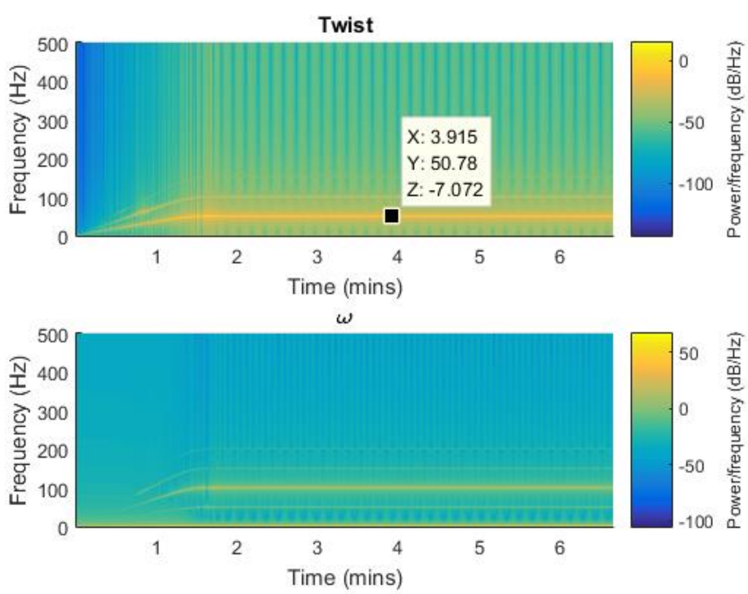

Figure 3.63 Spectrogram Case I Capture: $\delta_0 = 25°$

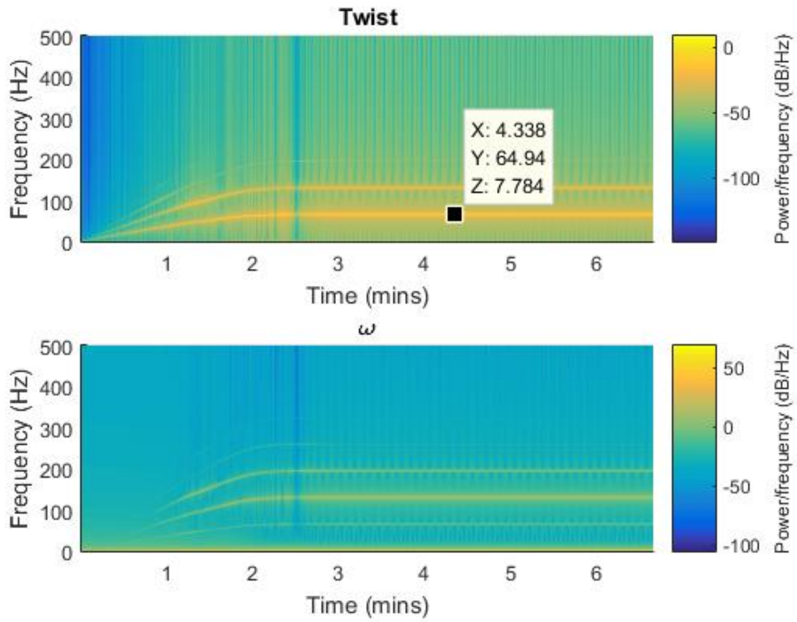

Figure 3.64 Spectrogram Case I Capture: $\delta_0 = 30°$

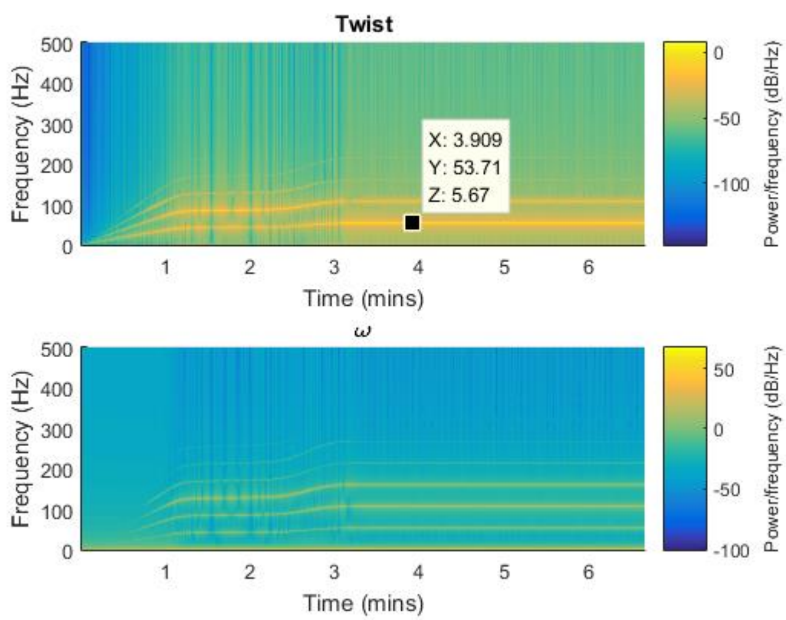

Figure 3.65 Spectrogram Case I Capture: $\delta_0 = 35°$

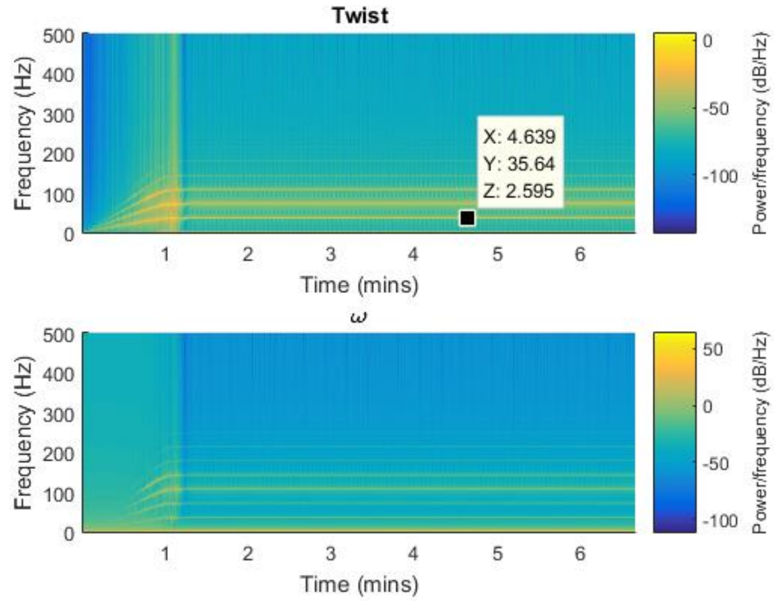

Figure 3.66 Spectrogram Case I Capture: $\delta_0 = 40°$

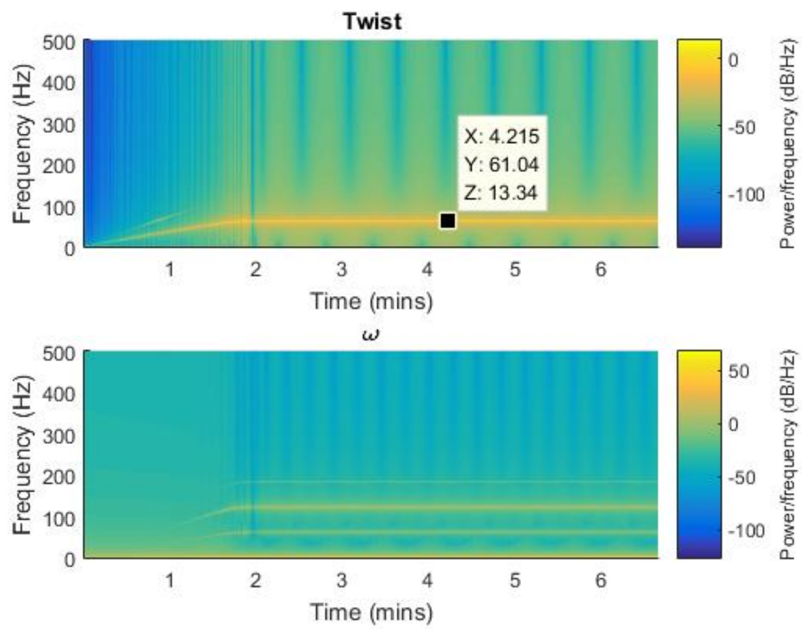

Figure 3.67 Spectrogram Case II Capture: $\delta_0 = 15°$

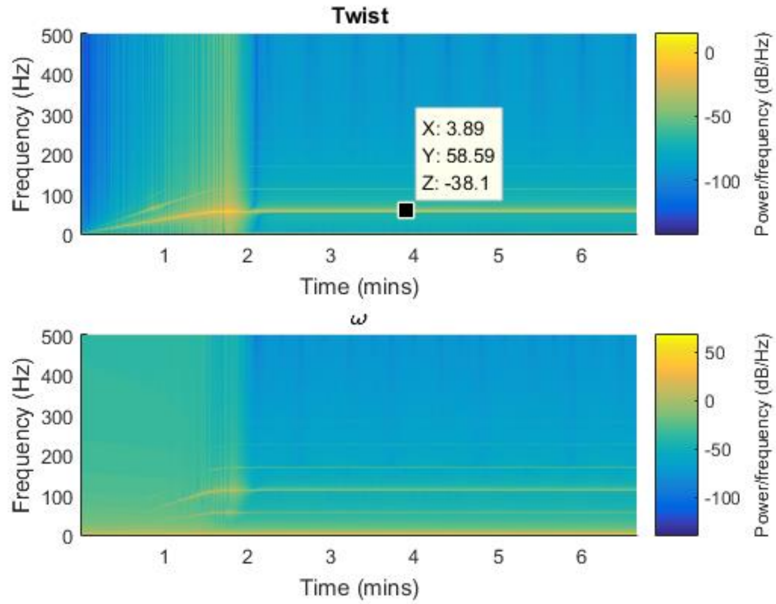

Figure 3.68 Spectrogram Case II Capture: $\delta_0 = 20°$

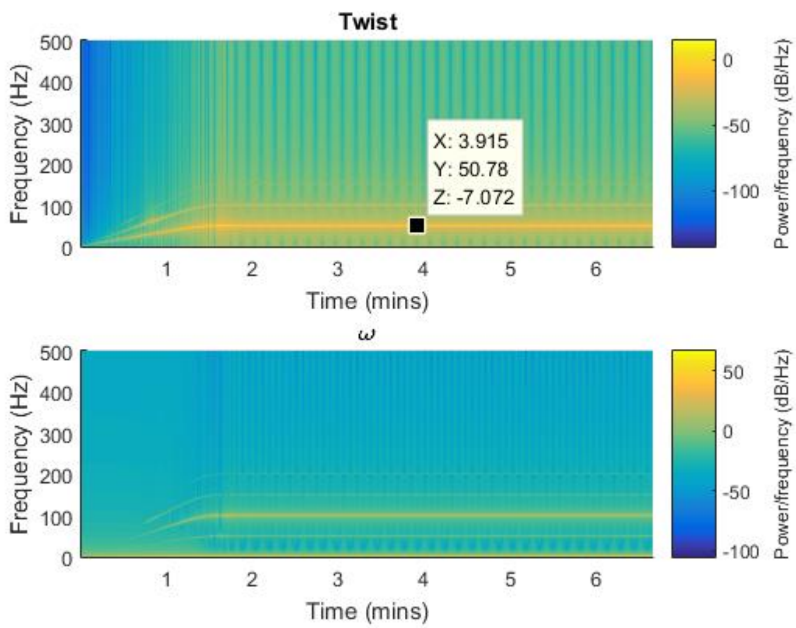

Figure 3.69 Spectrogram Case II Capture: $\delta_0 = 25°$

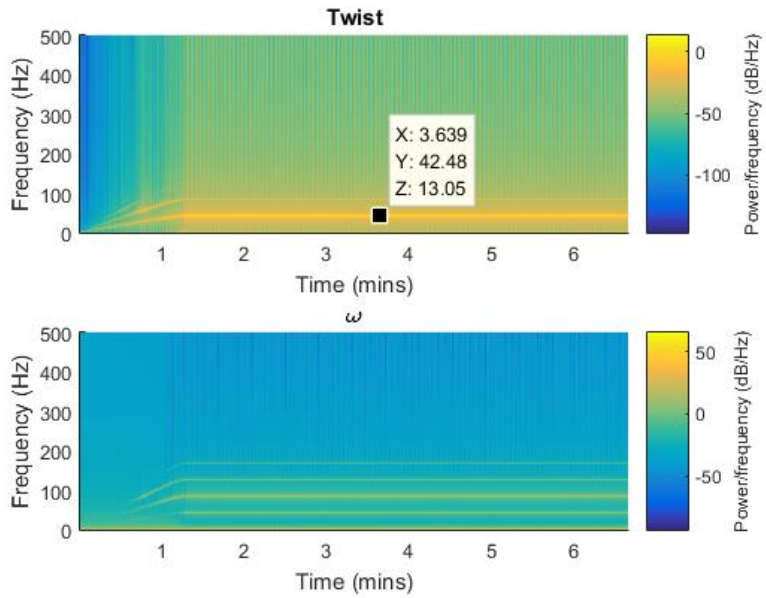

Figure 3.70 Spectrogram Case II Capture: $\delta_0 = 30°$

However, it is hard to determine the frequencies from Figure 3.71 and Figure 3.72 at the first time. Then the following frequency ramping curve method is used to determine the fundamental critical frequencies. The obtained critical frequencies are listed in Table 3.4.

Figure 3.73 and Figure 3.74 show the critical frequencies of the 3-DOF and 2-DOF model listed in Table 3.3 and Table 3.4. Two figures illustrate manifestly that the critical frequencies are closed under small misalignment conditions. Figure 3.73 illustrates that the difference between the critical frequencies is becoming wider corresponding to the different static misalignment conditions.

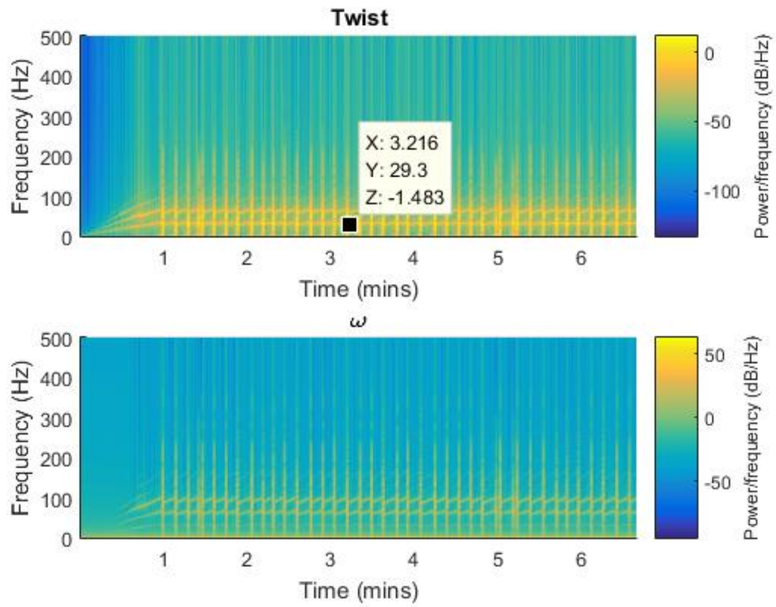

Figure 3.71 Spectrogram Case II Capture: $\delta_0 = 35°$

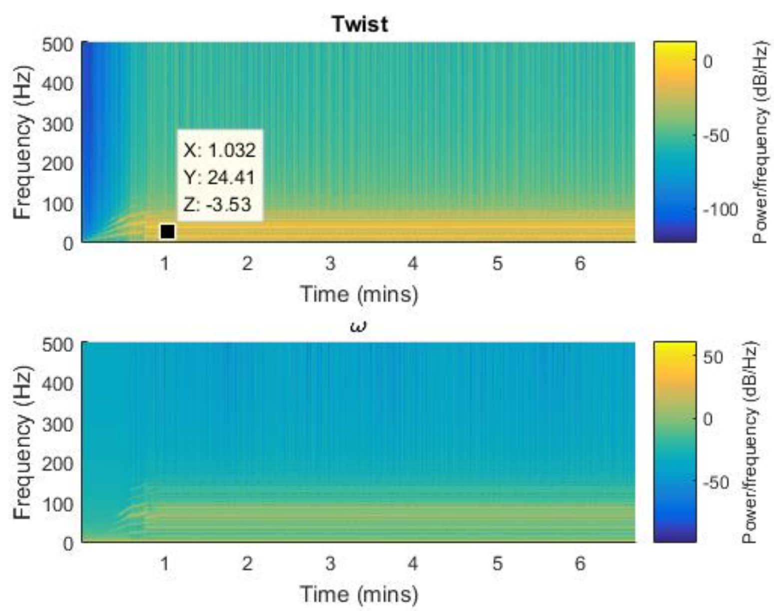

Figure 3.72 Spectrogram Case II Capture: $\delta_0 = 40°$

Table 3.4 1st Torsional Critical frequencies with Different δ_0

	Case I	Case II
Static misalignment angles δ_0 (°)	1st torsional peak f_t (Hz)	1st torsional peak f_t (Hz)
15	94.73	61.04
20	84.96	58.59
25	74.71	50.78
30	64.94	42.48
35	53.71	29.3
40	35.64	24.41

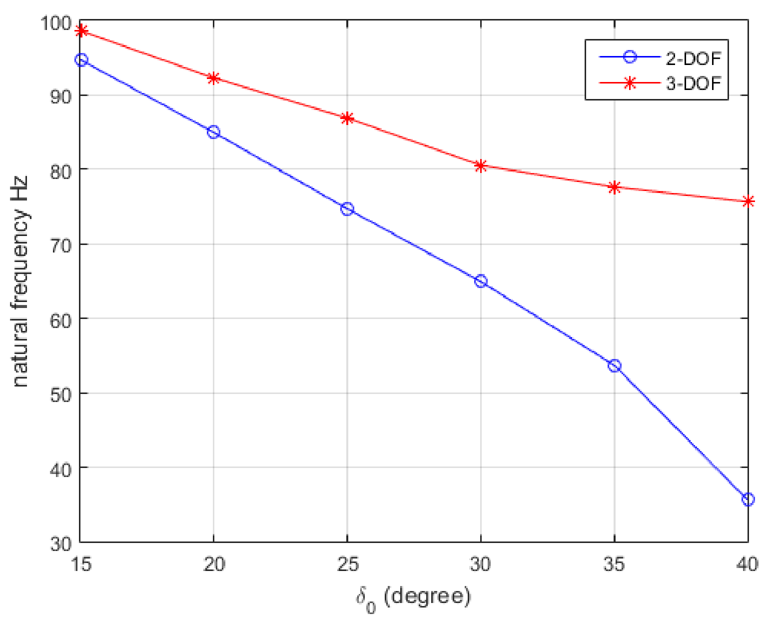

Figure 3.73 Critical Frequencies Comparison: Supercritical Case and Case I

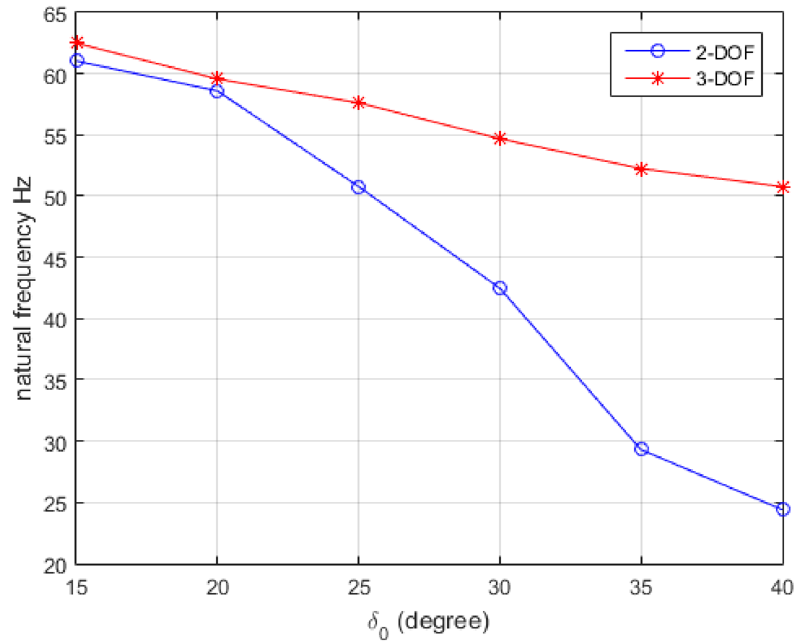

Figure 3.74 Critical Frequencies Comparison: Subcritical Case and Case II

The similar results in Figure 3.74 of the subcritical and case II results show the magnificent stabilizing effect of the lateral motion when the misalignment angle is larger than 20°.

3.5 Conclusion

This chapter explores the Sommerfeld effect in the nonlinear driveshaft system with a constant torque input. The numerical simulation results are shown in this chapter for two different nonlinear driveline system: 2-DOF and 3-DOF nonlinear model. Two parameter cases are used for each model, supercritical and subcritical case for the 3-DOF model, and case I and case II for the 2-DOF model.

A critical static misalignment angle is determined for the 3-DOF case that defines whether the Sommerfeld effect is observed. Time domain responses are presented for both the 2-DOF and 3-DOF model. The comparison between the results of two models indicates that the lateral motion stabilizes and alleviate the rotational motion. Moreover, the spectrogram is applied to obtain the critical frequencies when the Sommerfeld effect is observed. The critical frequencies are listed in Table 3.3 and Table 3.4. The comparison of the critical frequencies of the two models is shown in this chapter as well. Referring to the results, the critical frequencies are reducing while the static misalignment angle keeps ramping up. The determination of the static misalignment condition whether the Sommerfeld effect will occur in the nonlinear driveline system has been presented in this chapter. Next question that needs to be answered is that understanding the physical proposition of the critical frequencies shown in this chapter.

Chapter 4

NATURAL FREQUENCIES ANALYSIS OF THE NONLINEAR DRIVESHAFT SYSTEM

4.1 Introduction

The stability of the driveshaft system is analyzed in this chapter. The Floquet theory is the fundamental and effective method for the stability analysis of the linear time-varying period system. The Floquet method is applied for stability analysis on the other models (Guan & DeSmidt, 2018). The previous research works focus on the stability of the transient solutions, the real part of the eigenvalues of the Floquet Transition Matrix (FTM) is governing in the stability analysis. However, in this chapter, the imaginary parts of the eigenvalues are also obtained to indicate the natural frequencies varying (Zhao, DeSmidt, & Yao, 2015). In the previous chapter, the results indicate that the speed limits are independent of the lateral frequency, therefore the analysis on the natural frequencies is essential for understanding the phenomenon.

A linear numerical approximate system is reached from transferring the original linear time-varying analytical system by the Fourier series expansion method. The numerical approximate system is used to replace the analytical linear time-varying system for the natural frequencies analysis.

4.2 3-DOF Numerical Approximate Linear Time-Varying System

4. 2.1 Linearized Equations of Motion

The nonlinear equation (2.58) includes the nonlinearity of the driveline shaft system. Then a linearized model is proposed for the control purpose.

The degree-of-freedom of the nonlinear system is $q = \{\phi(t), \delta_1(t), \varphi(t)\}^T$. The twist angle and misalignment angles are

$$\begin{aligned} \phi(t) &= \phi_c(t) + \phi_h(t) \\ \delta_1(t) &= \delta_c(t) + \delta_h(t) \\ \varphi(t) &= \varphi_c(t) + \varphi_h(t) \end{aligned} \tag{4.1}$$

$\phi_c(t)$ is the assumed constant angular velocity, $\phi_h(t)$ is the perturbation term of the input angle. $\delta_c(t)$ is the major misalignment angle that is close to the $\delta_1(t)$, $\delta_h(t)$ is the perturbation term of the misalignment angle of U-joint A. $\varphi_c(t)$ is the major twist angle that is close to the $\varphi(t)$, $\varphi_h(t)$ is the perturbation term of the twist angle of the intermediate shaft. The nonlinear system is linearized here around large values by Taylor series expansion. Equation (4.3) is the Taylor series expansion for f(x) about *x*=*a*. then the nonlinear system can be linearized around the large values defined in equation (4.2)

$$\begin{aligned} q_0 &= [\ \phi_c(t) = \phi_c(t), \delta_c(t) = \delta_0, \varphi_c(t) = 0]^T \\ \dot{q}_0 &= [\dot{\phi}_c(t) = \dot{\phi}_c(t), \dot{\delta}_c(t) = 0, \dot{\varphi}_c(t) = 0]^T \\ \ddot{q}_0 &= [\ddot{\phi}_c(t) = \ddot{\phi}_c(t), \ddot{\delta}_c(t) = 0, \ddot{\varphi}_c(t) = 0]^T \end{aligned} \tag{4.2}$$

Defining the new degree of freedom vector, $q_h = [\phi(t), \delta_h(t), \varphi_h(t)]^T$

$$Eqnl_i = [[\boldsymbol{M_n}(t)]\ddot{q} + f(q,\dot{q})]_i|_{(\boldsymbol{q_0},\dot{\boldsymbol{q}}_0,\ddot{\boldsymbol{q}}_0)}$$
$$+ \frac{\partial[\boldsymbol{M_n}(t)]\ddot{q} + f(q,\dot{q})]_i}{\partial q_i}|_{(\boldsymbol{q_0},\dot{\boldsymbol{q}}_0,\ddot{\boldsymbol{q}}_0)} q_{h_i}$$
$$+ \frac{\partial[[\boldsymbol{M_n}(t)]\ddot{q} + f(q,\dot{q})]_i}{\partial \dot{q}_i}|_{(\boldsymbol{q_0},\dot{\boldsymbol{q}}_0,\ddot{\boldsymbol{q}}_0)} \dot{q}_{h_i} \tag{4.3}$$
$$+ \frac{\partial[[\boldsymbol{M_n}(t)]\ddot{q} + f(q,\dot{q})]_i}{\partial \ddot{q}_i}|_{(\boldsymbol{q_0},\dot{\boldsymbol{q}}_0,\ddot{\boldsymbol{q}}_0)} \ddot{q}_{h_i}\,, \qquad i = 1,2,3$$

Using the same method, we can also linearize the generalized term around the large values defined in equation (4.4) and equation (4.5)

$$\boldsymbol{QF} = \boldsymbol{F}_m(q,\dot{q}) + \boldsymbol{F}_L(q,\dot{q}) \tag{4.4}$$

$$QFl_i = [F_m(q,\dot{q}) + F_L(q,\dot{q})]_i|_{(\boldsymbol{q_0},\dot{\boldsymbol{q}}_0)} + \frac{\partial[F_m(q,\dot{q}) + F_L(q,\dot{q})]_i}{\partial q_i}|_{(\boldsymbol{q_0},\dot{\boldsymbol{q}}_0)} q_{h_i}$$
$$+ \frac{\partial[F_m(q,\dot{q}) + F_L(q,\dot{q})]_i}{\partial \dot{q}_i}|_{(\boldsymbol{q_0},\dot{\boldsymbol{q}}_0)} \dot{q}_{h_i}\,, \qquad i = 1,2,3 \tag{4.5}$$

After dropping off the high order terms and small value terms, the new equations of motion of the linearized system are delivered by equation (4.3) and equation (4.5), are shown in equation (4.6)

$$\boldsymbol{M}(t)\ddot{q}_h + \boldsymbol{Cd}(t)\dot{q}_h + (\boldsymbol{K}(t) - \boldsymbol{K_Q}(t))q_h = \boldsymbol{Q_f}(t) - \boldsymbol{f}(t) \tag{4.6}$$

Where $\boldsymbol{M}(t)$ is the time-varying mass matrix, $\boldsymbol{Cd}(t)$ is the time-varying damping matrix, $\boldsymbol{K}(t)$ is the time-varying stiffness matrix, $\boldsymbol{K_Q}(t)$ is the auxiliary stiffness matrix that is obtained from the linearized general force. $\boldsymbol{Q_f}(t)$ is the linearized generalized force, and $\boldsymbol{f}(t)$ is the auxiliary force.

4.2.2 Numerical Approximate Equations of Motion

All the time-varying matrices in linearized system equations are functions of $\frac{f_1(\phi_c(t))}{f_2(\phi_c(t))}$, where $f_i(\phi_c(t))$ means the function of $\phi_c(t)$. This expression is hard for further analysis and transformation. Then to separate the time-varying matrices into the form such as:

$$\boldsymbol{A}(t) = \boldsymbol{A} + \Delta\boldsymbol{A}(t) \tag{4.7}$$

Following equations from (4.8) to (4.13) are obtained by applying the Fourier series expansion. A reference constant angular velocity Ω is applied on Fourier series.

$$\begin{aligned}\boldsymbol{M} + \Delta\boldsymbol{M}(t) = &\sum_{n=0}^{N}[\frac{1}{2L}\int_{-L}^{L}\boldsymbol{M}(t)\cos\left(\frac{n\pi t}{L}\right)dt * cos\,(n\Omega t)] \\ &+ \sum_{m=1}^{N}[\frac{1}{2L}\int_{-L}^{L}\boldsymbol{M}(t)\sin\left(\frac{m\pi t}{L}\right)dt * sin\,(m\Omega t)]\end{aligned} \tag{4.8}$$

Also, with

$$\begin{aligned}\boldsymbol{Cd} + \Delta\boldsymbol{Cd}(t) = &\sum_{n=0}^{N}[\frac{1}{2L}\int_{-L}^{L}\boldsymbol{Cd}(t)\cos\left(\frac{n\pi t}{L}\right)dt * cos\,(n\Omega t)] \\ &+ \sum_{m=1}^{N}[\frac{1}{2L}\int_{-L}^{L}\boldsymbol{Cd}(t)\sin\left(\frac{m\pi t}{L}\right)dt * sin\,(m\Omega t)]\end{aligned} \tag{4.9}$$

$$\begin{aligned}\boldsymbol{K} + \Delta\boldsymbol{K}(t) = &\sum_{n=0}^{N}[\frac{1}{2L}\int_{-L}^{L}\boldsymbol{K}(t)\cos\left(\frac{n\pi t}{L}\right)dt * cos\,(n\Omega t)] \\ &+ \sum_{m=1}^{N}[\frac{1}{2L}\int_{-L}^{L}\boldsymbol{K}(t)\sin\left(\frac{m\pi t}{L}\right)dt * sin\,(m\Omega t)]\end{aligned} \tag{4.10}$$

$$\boldsymbol{K_Q} + \Delta\boldsymbol{K_Q}(t) = \sum_{n=0}^{N}[\frac{1}{2L}\int_{-L}^{L}\boldsymbol{K_Q}(t)\cos\left(\frac{n\pi t}{L}\right)dt * cos\,(n\Omega t)]$$
$$+ \sum_{m=1}^{N}[\frac{1}{2L}\int_{-L}^{L}\boldsymbol{K_Q}(t)\sin\left(\frac{m\pi t}{L}\right)dt * sin\,(m\Omega t)] \tag{4.11}$$

$$\boldsymbol{Q_f} + \Delta\boldsymbol{Q_f}(t) = \sum_{n=0}^{N}[\frac{1}{2L}\int_{-L}^{L}\boldsymbol{Q_f}(t)\cos\left(\frac{n\pi t}{L}\right)dt * cos\,(n\Omega t)]$$
$$+ \sum_{m=1}^{N}[\frac{1}{2L}\int_{-L}^{L}\boldsymbol{Q_f}(t)\sin\left(\frac{m\pi t}{L}\right)dt * sin\,(m\Omega t)] \tag{4.12}$$

$$\boldsymbol{f} + \Delta\boldsymbol{f}(t) = \sum_{n=0}^{N}[\frac{1}{2L}\int_{-L}^{L}\boldsymbol{f}(t)\cos\left(\frac{n\pi t}{L}\right)dt * cos\,(n\Omega t)]$$
$$+ \sum_{m=1}^{N}[\frac{1}{2L}\int_{-L}^{L}\boldsymbol{f}(t)\sin\left(\frac{m\pi t}{L}\right)dt * sin\,(m\Omega t)] \tag{4.13}$$

After dropping off the small value term from above Fourier series expansion, the equations of motion are rewritten as

$$[\boldsymbol{M} + \Delta\boldsymbol{M}(t)]\ddot{q}_h + [\boldsymbol{Cd} + \Delta\boldsymbol{Cd}(t)]\dot{q}_h + [\boldsymbol{K} + \Delta\boldsymbol{K}(t) - \boldsymbol{K_Q} - \Delta\boldsymbol{K_Q}(t)]q_h$$
$$= \boldsymbol{Q_f} + \Delta\boldsymbol{Q_f}(t) - \boldsymbol{f} - \Delta\boldsymbol{f}(t) \tag{4.14}$$

$\boldsymbol{M}$**,** $\boldsymbol{Cd}$**,** $\boldsymbol{K}$**,** $\boldsymbol{K_Q}$**,** $\boldsymbol{Q_f}$**,** $\boldsymbol{f}$ are constant mass, damping, stiffness, auxiliary stiffness matrix, generalized constant force, and auxiliary force. $\Delta\boldsymbol{M}(t)$**,** $\boldsymbol{\Delta Cd}(t)$**,** $\boldsymbol{\Delta K}(t)$**,** $\boldsymbol{\Delta K_Q}(t)$ **,** $\Delta\boldsymbol{Q_f}(t)$, and $\Delta\boldsymbol{f}(t)$ are time-varying mass, damping, stiffness, and auxiliary stiffness matrices, generalized force, and auxiliary force.

Where $\boldsymbol{Q_f}$ is defined as

$$\boldsymbol{Q_f} = \boldsymbol{B_u u} + \boldsymbol{Q_F} \tag{4.15}$$

And then let

$$\begin{aligned} \boldsymbol{Q_F}(\boldsymbol{t}) &= \boldsymbol{Q_F} + \Delta\boldsymbol{Q_f}(t) \\ \boldsymbol{F}(\boldsymbol{t}) &= \boldsymbol{f} + \Delta\boldsymbol{f}(t) \end{aligned} \tag{4.16}$$

4.2.3 Floquet Theory

The Floquet theory is the method that is proposed to obtain the solution of the linear time-varying periodic system.

The general linear time-varying system is expressed as

$$\dot{x} = \boldsymbol{A}(t)x \tag{4.17}$$

The general solution of the linear time-varying system is formed as

$$x(t) = \boldsymbol{\Phi}(t, t_0)x(t_0) \tag{4.18}$$

Where the $\boldsymbol{\Phi}(t, t_0)$ is the state transition matrix. The FTM is determined as

$$x(t_p) = \boldsymbol{\Phi}(t_p)x(t_p) \tag{4.19}$$

Where the $\mathbf{A}(t)$ is the periodic matrix with the period of t_p. Since the mass matrix in equation (4.14) is in a periodic time-varying form, which causes the complicity expression for the inverse of mass matrix, such that another form of solution is used to obtain the natural frequencies of the numerical approximate system. Then the solution is assumed as in equation (4.20)

$$q_h(t) = \sum_{n=1}^{2} e^{\lambda t}[\boldsymbol{Q_{s2n}} sin(2\text{n}\Omega t) + \boldsymbol{Q_{c2n}} cos(2\text{n}\Omega t)] \tag{4.20}$$

Substituting equation (4.17) back into the numerical approximate equation shown in equation (4.14). To obtain the eigenvalues of the FTM, the forcing terms are not included in the above equations. Therefore, the linear system can be transferred to the state space form, which is expressed in equation (4.21) after collecting the coefficients of harmonic terms.

$$\sum_{n=1}^{k}[p_{s2n}(\lambda^2,\lambda)\sin(2n\Omega t)+p_{c2n}(\lambda^2,\lambda)\cos(2n\Omega t)]=0 \tag{4.21}$$

Where $L_n, n=1,2\cdots 6$ are coefficient matrices those are in R^6

$$p_{s2n}(\lambda^2,\lambda)=L_1\lambda^2+L_2\lambda+L_3 \tag{4.22}$$

$$p_{c2n}(\lambda^2,\lambda)=L_4\lambda^2+L_5\lambda+L_6 \tag{4.23}$$

Then to obtain the Jacobi matrix by the equation (4.24)

$$Jacob=\{\frac{\partial p_{s2n}(\lambda^2,\lambda)}{\partial \boldsymbol{Q_{s2n}}}, \qquad \frac{\partial p_{c2n}(\lambda^2,\lambda)}{\partial \boldsymbol{Q_{c2n}}}\}^T=0 \tag{4.24}$$

Therefore, the eigenvalues of the FTM are obtained from the equation (4.22) by solving the λ. The real part of the solutions of λ indicates the stability of the system, and the imaginary part of the solutions indicate the natural frequencies of the system.

Only one harmonic frequency is assumed in solution, which is expressed in equation (4.25)

$$q_h(t)=e^{\lambda t}[\boldsymbol{Q_{s2}}sin(2\Omega t)+\boldsymbol{Q_{c2}}cos(2\Omega t)] \tag{4.25}$$

Where $\boldsymbol{Q_{s2}}=\{\phi_{s2},\delta_{s2},\varphi_{s2}\}^{\boldsymbol{T}}, \boldsymbol{Q_{c2}}=\{\phi_{c2},\delta_{c2},\varphi_{c2}\}^{\boldsymbol{T}}$ are coefficients of each variable state.

By substituting the equation (4.25) into the system dynamics equation (4.14). Then the harmonic balance method is applied to collect the coefficient of the harmonic terms regardless of the forcing terms.

After the Jacobi matrix is obtained by equation (4.24), then the equations are reorganized in the form shown in equation (4.26)

$$(\boldsymbol{M_L}\lambda^2 + \boldsymbol{C_L}\lambda + \boldsymbol{K_L})\boldsymbol{Q_c} = 0 \tag{4.26}$$

The eigenvalues of the system are obtained by solving λ in equation (4.26). Where $\boldsymbol{M_L}, \boldsymbol{C_L}, \boldsymbol{K_L}$ are coefficient matrices in $R^{6\times 6}$, and $\boldsymbol{Q_c} = \begin{Bmatrix} \boldsymbol{Q_{s2}} \\ \boldsymbol{Q_{c2}} \end{Bmatrix}$.

4.2.4 Natural Frequency Curve

The natural frequencies of the LTV system can be obtained from the imaginary part of the λ. The plot in following Figure 4.1 and Figure 4.2 indicates the natural frequencies of the system under different static misalignment angles for both supercritical and subcritical case.

Figure 4.1 and Figure 4.2 show the natural frequencies of the driveshaft system varying respect to the variable static misalignment conditions. Star points in the figures are the critical frequencies of the system under the different misalignment conditions listed in Table 3.3. The figures indicate that the 1st critical frequency of lateral response in both cases is matching the varying of the lateral natural frequencies. The above results indicate that the natural frequencies of the driveshaft system are not constant for different misalignment conditions.

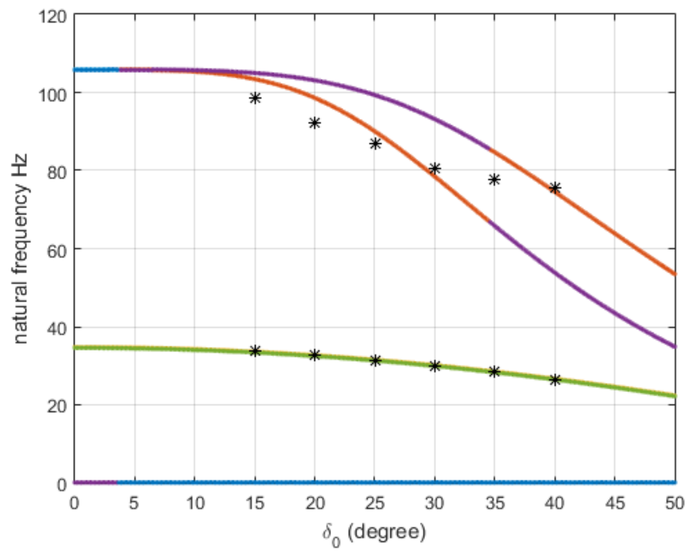

Figure 4.1 3-DOF Natural Frequencies: supercritical case

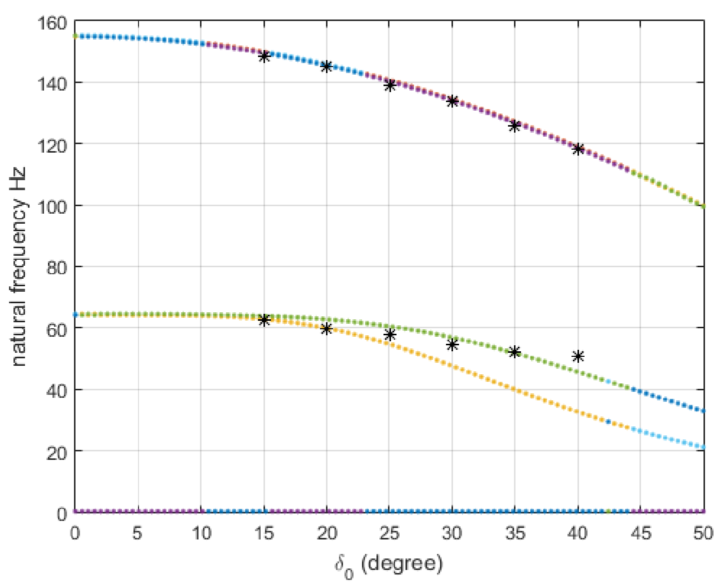

Figure 4.2 3-DOF Natural Frequencies: subcritical case

The important information is given in this section explore the system property of the driveshaft system under variable misalignment conditions. As we can see from both figures, the 1st critical frequencies in torsional response are close to the curve of the torsional natural frequencies. Figure 4.2 shows the natural frequencies varying in the subcritical case. As the same as the result of the supercritical case in Figure 4.1, the critical frequencies of the lateral frequency match the curve of the lateral natural frequencies, moreover, the critical frequencies of torsional responses are close to the curves of the torsional natural frequencies. These two figures are essential to indicate the physical explanations of the critical frequencies in Table 3.3. As the figures point out that the torsional critical frequency is not only dependent on the torsional natural frequency. Furthermore, though the torsional critical frequencies may not be related to combinations of the lateral and torsional frequencies, it is definitely affected by the lateral motion. The natural frequency curves present the phenomenon that the natural frequencies of this nonlinear driveshaft system reduce corresponding to the rising of the static misalignment angle. This curve provides the physical proposition of the gradual reduction of the critical speed values.

4.3 2-DOF Numerical Approximate Linear Time-Varying System

4.3.1 Numerical Approximate Linearized System

The degree-of-freedom of the reduced nonlinear system is $q_r = \{\phi(t), \varphi(t)\}^T$. The twist angle and misalignment angles are

$$\begin{aligned} \phi(t) &= \phi_c(t) + \phi_h(t) \\ \varphi(t) &= \varphi_c(t) + \varphi_h(t) \end{aligned} \tag{4.27}$$

$\phi_c(t)$ is the assumed rotating angular, $\phi_h(t)$ is the perturbation term of the input angle. $\varphi_c(t)$ is the major twist angle that is close to the $\varphi(t)$, $\varphi_h(t)$ is the perturbation term of the twist angle of the intermediate shaft. The nonlinear system is linearized here around large values by Taylor series expansion.

$$\begin{aligned} q_{r0} &= [\ \phi_c(t) = \phi_c(t), \varphi_c(t) = 0]^T \\ \dot{q}_{r0} &= [\dot{\phi}_c(t) = \dot{\phi}_c(t), \dot{\varphi}_c(t) = 0]^T \\ \ddot{q}_{r0} &= [\ddot{\phi}_c(t) = \ddot{\phi}_c(t), \ddot{\varphi}_c(t) = 0]^T \end{aligned} \tag{4.28}$$

Defining the new degree of freedom vector, $q_{hr} = [\phi_h(t), \varphi_h(t)]^T$

$$\begin{aligned} Eqnl_{ri} = {} & [[\boldsymbol{M_{nr}}(q_r)]\ddot{q}_r + f(q_r, \dot{q}_r)]_i|_{(\boldsymbol{q_{r0}}, \dot{\boldsymbol{q}}_{\boldsymbol{r0}}, \ddot{\boldsymbol{q}}_{\boldsymbol{r0}})} \\ & + \frac{\partial[\boldsymbol{M_{nr}}(\boldsymbol{q_r})]\ddot{q}_r + f(q_r, \dot{q}_r)]_i}{\partial q_{ri}}|_{(\boldsymbol{q_{r0}}, \dot{\boldsymbol{q}}_{\boldsymbol{r0}}, \ddot{\boldsymbol{q}}_{\boldsymbol{r0}})} q_{hr_i} \\ & + \frac{\partial[[\boldsymbol{M_{nr}}(\boldsymbol{q_r})]\ddot{q}_r + f(q_r, \dot{q}_r)]_i}{\partial \dot{q}_{ri}}|_{(\boldsymbol{q_{r0}}, \dot{\boldsymbol{q}}_{\boldsymbol{r0}}, \ddot{\boldsymbol{q}}_{\boldsymbol{r0}})} \dot{q}_{hr_i} \\ & + \frac{\partial[[\boldsymbol{M_{nr}}(q_r)]\ddot{q}_r + f(q_r, \dot{q}_r)]_i}{\partial \ddot{q}_{ri}}|_{(\boldsymbol{q_{r0}}, \dot{\boldsymbol{q}}_{\boldsymbol{r0}}, \ddot{\boldsymbol{q}}_{\boldsymbol{r0}})} \ddot{q}_{hr_i}, \qquad i = 1,2 \end{aligned} \tag{4.29}$$

Using the same method, we can also linearize the generalized term around the large values defined in equation (4.30) and equation (4.31)

$$\boldsymbol{QF} = \boldsymbol{F}_{mr}(q_r, \dot{q}_r) + \boldsymbol{F}_{Lr}(q_r, \dot{q}_r) \tag{4.30}$$

$$\begin{aligned} QFl_i = {} & [F_{mr}(q_r, \dot{q}_r) + F_{Lr}(q_r, \dot{q}_r)]_i|_{(\boldsymbol{q_{r0}}, \boldsymbol{\dot{q}_{r0}})} \\ & + \frac{\partial [F_{mr}(q_r, \dot{q}_r) + F_{Lr}(q_r, \dot{q}_r)]_i}{\partial q_{ri}}|_{(\boldsymbol{q_{r0}}, \boldsymbol{\dot{q}_{r0}})} q_{hr_i} \\ & + \frac{\partial [F_{mr}(q_r, \dot{q}_r) + F_{Lr}(q_r, \dot{q}_r)]_i}{\partial \dot{q}_{ri}}|_{(\boldsymbol{q_{r0}}, \boldsymbol{\dot{q}_{r0}})} \dot{q}_{hr_i}, \qquad i = 1,2 \end{aligned} \tag{4.31}$$

After dropping off the high order terms and small value terms, the new equations of motion of the linearized system are delivered by equation (4.3) and equation (4.5), are shown in equation (4.6)

$$\boldsymbol{M_r}(t)\ddot{q}_{hr} + \boldsymbol{Cd_r}(t)\dot{q}_{hr} + (\boldsymbol{K_r}(t) - \boldsymbol{K_{Qr}}(t))q_{hr} = \boldsymbol{Q_{fr}}(t) - \boldsymbol{f_r}(t) \tag{4.32}$$

Where $\boldsymbol{M_r}(t)$ is the time-varying mass matrix, $\boldsymbol{Cd_r}(t)$ is the time-varying damping matrix, $\boldsymbol{K_r}(t)$ is the time-varying stiffness matrix, $\boldsymbol{K_{Qr}}(t)$ is the auxiliary stiffness matrix that is obtained from the linearized general force. $\boldsymbol{Q_{fr}}(t)$ is the linearized generalized force, and $\boldsymbol{f_r}(t)$ is the auxiliary force.

After following the steps in section 4.2.3, the numerical approximate matrices are obtained. After dropping off the small value term from above Fourier series expansion, the equations of motion are rewritten as,

$$\begin{aligned} & [\boldsymbol{M_r} + \Delta\boldsymbol{M_r}(t)]\ddot{q}_{hr} + [\boldsymbol{Cd_r} + \Delta\boldsymbol{Cd_r}(t)]\dot{q}_{hr} + [\boldsymbol{K_r} + \Delta\boldsymbol{K_r}(t) - \boldsymbol{K_{Qr}} \\ & - \Delta\boldsymbol{K_{Qr}}(t)]q_{hr} = \boldsymbol{Q_{fr}} + \Delta\boldsymbol{Q_{fr}}(t) - \boldsymbol{f_r} - \Delta\boldsymbol{f_r}(t) \end{aligned} \tag{4.33}$$

$\boldsymbol{M_r}$, $\boldsymbol{Cd_r}$, $\boldsymbol{K_r}$, $\boldsymbol{K_{Qr}}$, $\boldsymbol{Q_{fr}}$, $\boldsymbol{f_r}$ are constant mass, damping, stiffness, auxiliary stiffness matrix, generalized constant force, and auxiliary force. $\Delta\boldsymbol{M_r}(t)$, $\boldsymbol{\Delta Cd_r}(t)$,

$\boldsymbol{\Delta K_r}(t)$**,** $\boldsymbol{\Delta K_{Qr}}(t)$**,** $\Delta\boldsymbol{Q_{fr}}(t)$, and $\Delta\boldsymbol{f_r}(t)$ are time-varying mass, damping, stiffness, and auxiliary stiffness matrices, generalized force, and auxiliary force.

Where $\boldsymbol{Q_{fr}}$ is defined as

$$\boldsymbol{Q_{fr}} = \boldsymbol{B_{ur}}u + \boldsymbol{Q_{Fr}} \tag{4.34}$$

And then let

$$\begin{gathered} \boldsymbol{Q_{Fr}}(\boldsymbol{t}) = \boldsymbol{Q_{Fr}} + \Delta\boldsymbol{Q_{fr}}(t) \\ \boldsymbol{F_r}(\boldsymbol{t}) = \boldsymbol{f_r} + \Delta\boldsymbol{f_r}(t) \end{gathered} \tag{4.35}$$

4.3.3 Floquet Method and Natural Frequencies

The same Floquet method is applied to the system, the steady-state solution is proposed as in the form

$$q_{hr}(t) = e^{\lambda t}[\boldsymbol{Q_{s2r}} sin(2\Omega t) + \boldsymbol{Q_{c2r}} cos(2\Omega t)] \tag{4.36}$$

Where $\boldsymbol{Q_{s2r}} = \{\phi_{s2}, \varphi_{s2}\}^{\boldsymbol{T}}, \boldsymbol{Q_{c2r}} = \{\phi_{c2}, \varphi_{c2}\}^{\boldsymbol{T}}$ are coefficients of each variable state. By substituting the equation (4.36) into the system dynamics equation (4.33). Then the harmonic balance method is applied to collect the coefficient of the harmonic terms regardless of the forcing terms.

After the Jacobi matrix is obtained by equation (4.24), then the equations are reorganized in the form shown in equation (4.37)

$$(\boldsymbol{M_{Lr}}\lambda^2 + \boldsymbol{C_{Lr}}\lambda + \boldsymbol{K_{Lr}})\boldsymbol{Q_{cr}} = 0 \tag{4.37}$$

The eigenvalues of the system are obtained by solving λ in the equation (4.37) Where $\boldsymbol{M_{Lr}}, \boldsymbol{C_{Lr}}, \boldsymbol{K_{Lr}}$ are coefficient matrices in $R^{4\times4}$, and $\boldsymbol{Q_{cr}} = \begin{Bmatrix} \boldsymbol{Q_{s2r}} \\ \boldsymbol{Q_{c2r}} \end{Bmatrix}$.

The figures show the natural frequency curve of the 2-DOF LTV system for both cases. The star points are critical speed collected from Table 3.4. Referring to Figure 4.3 and Figure 4.4, the critical frequencies are closely following the shape of the natural frequencies curve in both cases. As a comparison with Figure 4.1 and Figure 4.2, the critical frequencies are in the middle of the natural frequency curve at the large static misalignment angles regardless of the shape of the curve. This phenomenon happened due to the lateral movement and the effect of the lateral natural frequencies. Therefore, the results of the comparison indicate that there is weak coupling between the lateral and torsional motion in the nonlinear model.

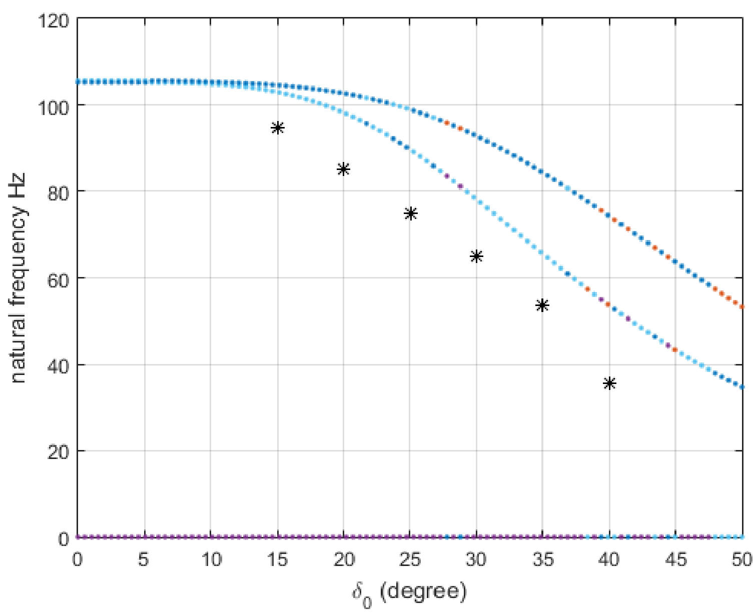

Figure 4.3 2-DOF Natural Frequencies: Supercritical Case

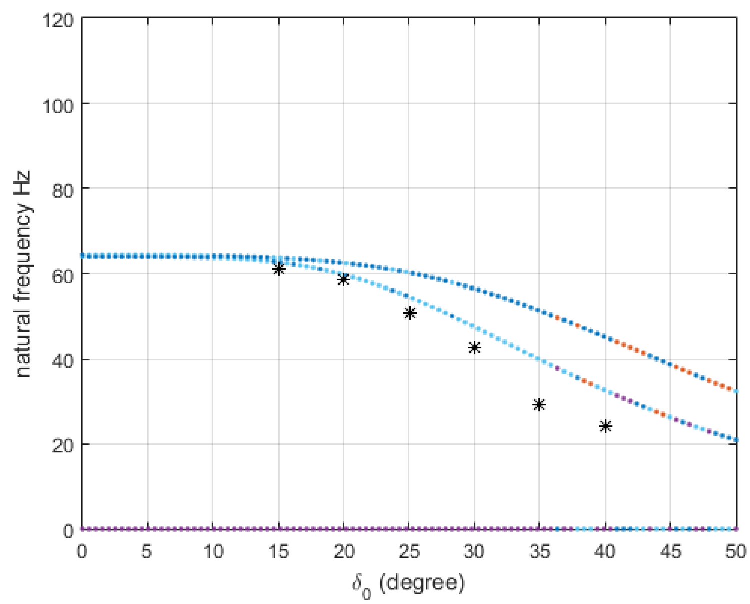

Figure 4.4 2-DOF Natural Frequencies: Subcritical Case

However, the critical frequencies are just affected by the lateral motion slightly even though in the nonlinear system. As the trend of the critical frequencies, the natural frequencies of the nonlinear system are slightly different from the curve obtained from the approximate LTV system. The Floquet method is valid for the reference in this section other than the tool for obtaining the critical frequencies.

4.4 Conclusion

In this chapter, a numerical approximate linear time-varying model is proposed at first. Since the complicity of the nonlinear system model, the mathematical tool for stability analysis is hard to apply to it. However, the matrices of the linearized are still too complicated to be applied to any analytical assumed solutions. Therefore, the Fourier series expansion is used to obtain the numerical approximate linear time-varying system whose matrices do not involve the trigonometric functions in denominator terms. Then the Floquet method is applied on the approximate LTV model to obtain the natural frequencies of the driveline system for both models and both case for each model. Comparison of the natural frequencies and the critical frequencies of the system, the results show that the torsional critical frequencies are more related to the torsional natural frequencies of the system. The critical frequencies of the 2-DOF model are more adjacent to the shape of the natural frequency curve. However, the critical frequencies of the 3-DOF are manifestly under the effect from the lateral motion of the driveline system.

The lateral critical frequencies of the 3-DOF model are harmonized with the natural frequency curve. This means that the lateral critical frequency is normally independent of the coupled torsional motion. Moreover, the torsional motion has few effects on the stability of the lateral motion. Reversely, the lateral motion coupled to the torsional motion in the nonlinear model has an effect on the torsional critical frequency. Referring to that the critical frequencies are still adjacent to the torsional natural frequency curve, the coupled lateral motion marginally affect the torsional critical frequency in the nonlinear system under the offset misalignment condition. Furthermore, the larger the static misalignment condition is, the more manifestly effect from the lateral motion has on the torsional critical frequency.

Chapter 5
SLIDING MODE CONTROL DESIGN FOR MISALIGNED DRIVESHAFT SYSTEM

5.1 Introduction

In this chapter, a numerical control strategy is designed for the nonlinear system whose output speed is controlled to follow a reference speed on the output feedback control condition. A sliding mode control method is applied to the linearized model. Then the robust control theorem is applied on the reduced order system when the reaching condition of sliding mode control is satisfied. The steps to obtain the linear time-varying terms are introduced first. Then the sliding mode control is designed base on the above linear time-varying model. A linear quadratic regulator (LQR) is applied to determine the feedback gain that stabilizes the reduced order system when the system reaches the sliding surface. The whole control strategy is designed under the output-feedback system.

5.2 Sliding Mode Control Design for the Linearized System

The above linear time-varying system is used for the further controller design. The designed numerical sliding mode control is used to control the nonlinear system that is shown in equation (2.58). The control flow figure is shown in Figure 5.1

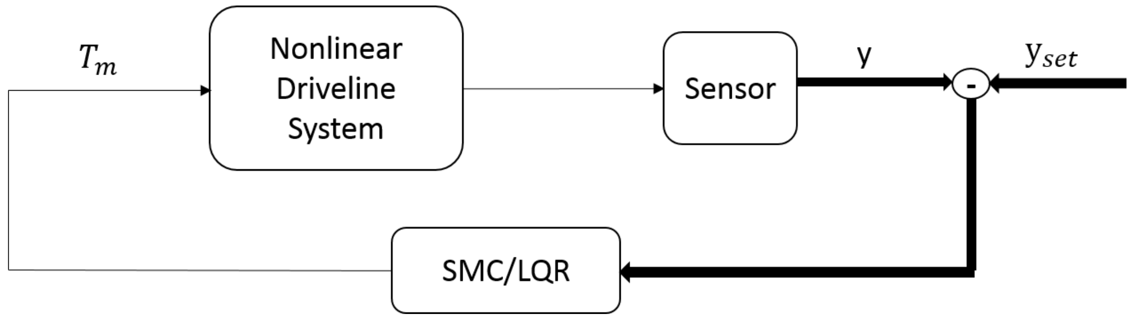

Figure 5.1 Hybrid SMC/LQR Structure

The sliding mode control is designed for the linear time-varying system. For the purpose of controller design, the equations of motion need to be transferred to state space form. The equation (4.14) is multiplied with $\boldsymbol{M^{-1}}$ on both sides, then we have the equation (5.1)

$$[\boldsymbol{I} + \boldsymbol{M^{-1}}\Delta\boldsymbol{M}(t)]\ddot{q}_h + \boldsymbol{M^{-1}}[\boldsymbol{Cd} + \Delta\boldsymbol{Cd}(t)]\dot{q}_h + \boldsymbol{M^{-1}}[\boldsymbol{K} + \Delta\boldsymbol{K}(t) - \boldsymbol{K_Q} - \Delta\boldsymbol{K_Q}(t)]q_h = \boldsymbol{M^{-1}}[\boldsymbol{B_u u} + \boldsymbol{Q_F}(t) - \boldsymbol{F}(\boldsymbol{t})] \quad (5.1)$$

The approach in Linear Algebra Book is employed for the approximate the term $[\boldsymbol{I} + \boldsymbol{M^{-1}}\Delta\boldsymbol{M}(t)]^{-\boldsymbol{1}}$, which is in equation (5.2)

$$[\boldsymbol{I} + \boldsymbol{M^{-1}}\Delta\boldsymbol{M}(t)]^{-\boldsymbol{1}} \approx [\boldsymbol{I} - \boldsymbol{M^{-1}}\Delta\boldsymbol{M}(t)], \quad (5.2)$$

Then using above the approximation equation by pre-multiplying the inverse matrix $[\boldsymbol{I} + \boldsymbol{M^{-1}}\Delta\boldsymbol{M}(t)]^{-\boldsymbol{1}}$ on both sides of equation (5.1). when the following condition that is the $\left|\boldsymbol{eig}(\boldsymbol{I} + \boldsymbol{M^{-1}}\Delta\boldsymbol{M}(t))\right| < 1$ is satisfied. Then we have the new approximation form of equations of motion in equation (5.3)

$$\ddot{q}_h + [\boldsymbol{I} - \boldsymbol{M}^{-1}\Delta\boldsymbol{M}(t)]\boldsymbol{M}^{-1}[\boldsymbol{Cd} + \Delta\boldsymbol{Cd}(t)]\dot{q}_h + [\boldsymbol{I} - \boldsymbol{M}^{-1}\Delta\boldsymbol{M}(t)]\boldsymbol{M}^{-1}[\boldsymbol{K} + \Delta\boldsymbol{K}(t) - \boldsymbol{K_Q} - \Delta\boldsymbol{K_Q}(t)]q_h = [\boldsymbol{I} - \boldsymbol{M}^{-1}\Delta\boldsymbol{M}(t)]\boldsymbol{M}^{-1}[\boldsymbol{B_u u} + \boldsymbol{Q_F}(t) - \boldsymbol{F}(\boldsymbol{t})] \tag{5.3}$$

Now we can transfer the above LTV differential equations into state space form

$$\begin{bmatrix}\dot{q}_h \\ \ddot{q}_h\end{bmatrix} = \begin{bmatrix}\boldsymbol{0} & \boldsymbol{I} \\ \boldsymbol{A_{21}} & \boldsymbol{A_{22}}\end{bmatrix}\begin{bmatrix}q_h \\ \dot{q}_h\end{bmatrix} + \begin{bmatrix}\boldsymbol{0} \\ [\boldsymbol{I} - \boldsymbol{M}^{-1}\Delta\boldsymbol{M}(t)]\boldsymbol{M}^{-1}[\boldsymbol{B_u u} + \boldsymbol{Q_F}(t) - \boldsymbol{F}(\boldsymbol{t})]\end{bmatrix} \tag{5.4}$$

Where

$$\boldsymbol{A_{21}} = -[\boldsymbol{I} - \boldsymbol{M}^{-1}\Delta\boldsymbol{M}(t)]\boldsymbol{M}^{-1}[\boldsymbol{K} + \Delta\boldsymbol{K}(t) - \boldsymbol{K_Q} - \Delta\boldsymbol{K_Q}(t)] \tag{5.5}$$

$$\boldsymbol{A_{22}} = -[\boldsymbol{I} - \boldsymbol{M}^{-1}\Delta\boldsymbol{M}(t)]\boldsymbol{M}^{-1}[\boldsymbol{Cd} + \Delta\boldsymbol{Cd}(t)] \tag{5.6}$$

Let $\boldsymbol{x} = [\boldsymbol{q}_h{}^T, \dot{\boldsymbol{q}}_h{}^T]^T \in \mathbb{R}^{n_x \times 1}$ is the state vector, and $\boldsymbol{y} \in \mathbb{R}^{n_y \times 1}$ is the output vector.

$$\boldsymbol{A_t} = \begin{bmatrix}\boldsymbol{0} & \boldsymbol{I} \\ \boldsymbol{A_{21}} & \boldsymbol{A_{22}}\end{bmatrix} \tag{5.7}$$

$\boldsymbol{A_t} \in \mathbb{R}^{n_X \times n_x}$ is the state matrix. As only the output values are measurable, then the output equation is

$$\boldsymbol{y} = \boldsymbol{Cx} \tag{5.8}$$

Where **C**$\in \mathbb{R}^{n_y \times n_x}$ is the output matrix.

After reorganizing the equation (5.4), the system dynamics is expressed in

$$\begin{gathered}\dot{\boldsymbol{x}} = \boldsymbol{Ax} + \boldsymbol{B_N u} + \boldsymbol{H}(t)\boldsymbol{x} + \Delta\boldsymbol{B_N}(t)\boldsymbol{u} + \boldsymbol{F_N}(t) \\ \boldsymbol{y} = \boldsymbol{Cx}\end{gathered} \tag{5.9}$$

The matrices in equation (5.9) are shown in following,

$$\boldsymbol{A} = \begin{bmatrix} \boldsymbol{0} & \boldsymbol{I} \\ -\boldsymbol{M}^{-1}(\boldsymbol{K} - \boldsymbol{K_Q}) & -\boldsymbol{M}^{-1}\boldsymbol{Cd} \end{bmatrix} \tag{5.10}$$

$$\boldsymbol{B_N} = \begin{bmatrix} 0 \\ \boldsymbol{M}^{-1}\boldsymbol{B_u} \end{bmatrix} \tag{5.11}$$

$$\boldsymbol{H}(t) = \begin{bmatrix} 0 & I \\ \boldsymbol{H_{21}} & -\boldsymbol{M}^{-1}\Delta\boldsymbol{Cd}(t) + \boldsymbol{M}^{-1}\Delta\boldsymbol{M}(t)\boldsymbol{M}^{-1}[\boldsymbol{Cd} + \Delta\boldsymbol{Cd}(t)] \end{bmatrix} \tag{5.12}$$

With

$$\boldsymbol{H_{21}} = -\boldsymbol{M}^{-1}[\Delta\boldsymbol{K}(t) - \Delta\boldsymbol{K_Q}(t)] + \boldsymbol{M}^{-1}\Delta\boldsymbol{M}(t)\boldsymbol{M}^{-1}[\boldsymbol{K} + \Delta\boldsymbol{K}(t) - \boldsymbol{K_Q} - \Delta\boldsymbol{K_Q}(t)] \tag{5.13}$$

$$\Delta\boldsymbol{B_N}(\boldsymbol{t}) = \begin{bmatrix} 0 \\ -\boldsymbol{M}^{-1}\Delta\boldsymbol{M}(t)\boldsymbol{M}^{-1}\boldsymbol{B_u} \end{bmatrix} \tag{5.14}$$

$$\boldsymbol{F_N}(\boldsymbol{t}) = \begin{bmatrix} \boldsymbol{0} \\ [\boldsymbol{I} - \boldsymbol{M}^{-1}\Delta\boldsymbol{M}(t)]\boldsymbol{M}^{-1}[\boldsymbol{Q_F}(\boldsymbol{t}) - \boldsymbol{F}(\boldsymbol{t})] \end{bmatrix} \tag{5.15}$$

The matching condition is essential for the sliding mode control strategy proposed by (Edwards & Spurgeon, 1995). Then transfer the system in equation (5.9) into the numerical approximation form that is valid for the matching condition

$$\begin{gathered} \dot{\boldsymbol{x}} = \boldsymbol{Ax} + \boldsymbol{B_N u} + \boldsymbol{B_N \xi_H}(\boldsymbol{t})\boldsymbol{x} + \boldsymbol{B_N \xi_B}(\boldsymbol{t})\boldsymbol{u} + \boldsymbol{B_N \xi_F}(\boldsymbol{t}) \\ \boldsymbol{y} = \boldsymbol{Cx} \end{gathered} \tag{5.16}$$

Where

$$\begin{gathered} \boldsymbol{\xi_H}(\boldsymbol{t}) = \boldsymbol{B_N^{-1}}\boldsymbol{H}(t) \\ \boldsymbol{\xi_B}(\boldsymbol{t}) = \boldsymbol{B_N^{-1}}\Delta\boldsymbol{B_N}(t) \\ \boldsymbol{\xi_F}(\boldsymbol{t}) = \boldsymbol{B_N^{-1}}\boldsymbol{F}(t) \end{gathered} \tag{5.17}$$

$\boldsymbol{B_N^{-1}}$ is the left inverse matrix of $\boldsymbol{B_N}$, and $\boldsymbol{\xi_H}(\boldsymbol{t})$

Now suppose a new state vector $\boldsymbol{z}$ that is transferred from the original vector **x** in equation (5.18).

$$\boldsymbol{z} = \boldsymbol{T}\boldsymbol{x} \tag{5.18}$$

then the system dynamics are transferred to the equation (5.19) by substituting equation (5.18) into equation (5.9),

$$\begin{gathered} \dot{\boldsymbol{z}} = \boldsymbol{TAT^{-1}z} + \boldsymbol{TB_N u} + \boldsymbol{TB_N \xi_H(t) T^{-1} z} + \boldsymbol{TB_N \xi_B(t) u} + \boldsymbol{TB_N \xi_F(t)} \\ \boldsymbol{y} = \boldsymbol{CT^{-1}z} \end{gathered} \tag{5.19}$$

The $\boldsymbol{T}$ is the transform matrix, which satisfies the condition in equation (5.18)

$$\boldsymbol{TB_N} = \begin{bmatrix} \boldsymbol{0}_{(\boldsymbol{n_x}-\boldsymbol{n_u})\times \boldsymbol{n_u}} \\ \boldsymbol{B} \end{bmatrix} \tag{5.20}$$

Where $\boldsymbol{B} \in \mathbb{R}^{n_u \times n_u}$ is the transferred constant input matrix.

And equation (5.19) can be expressed in equation (5.21) as well,

$$\begin{gathered} \begin{bmatrix} \dot{\boldsymbol{z}}_1 \\ \dot{\boldsymbol{z}}_2 \end{bmatrix} = \begin{bmatrix} \overline{\boldsymbol{A}}_{11} & \overline{\boldsymbol{A}}_{12} \\ \overline{\boldsymbol{A}}_{21} & \overline{\boldsymbol{A}}_{22} \end{bmatrix} \begin{bmatrix} \boldsymbol{z}_1 \\ \boldsymbol{z}_2 \end{bmatrix} + \begin{bmatrix} \boldsymbol{0} \\ \boldsymbol{B} \end{bmatrix} \boldsymbol{u} + \begin{bmatrix} \boldsymbol{0} \\ \boldsymbol{B\xi_H(t)} \end{bmatrix} \boldsymbol{T}^{-1} \begin{bmatrix} \boldsymbol{z}_1 \\ \boldsymbol{z}_2 \end{bmatrix} + \begin{bmatrix} \boldsymbol{0} \\ \boldsymbol{B\xi_B(t)} \end{bmatrix} \boldsymbol{u} \\ + \begin{bmatrix} \boldsymbol{0} \\ \boldsymbol{B\xi_F(t)} \end{bmatrix} \\ \begin{bmatrix} \boldsymbol{y}_1 \\ \boldsymbol{y}_2 \end{bmatrix} = \begin{bmatrix} \overline{\boldsymbol{C}}_1 & \overline{\boldsymbol{C}}_2 \end{bmatrix} \begin{bmatrix} \boldsymbol{z}_1 \\ \boldsymbol{z}_2 \end{bmatrix} \end{gathered} \tag{5.21}$$

Assuming the sliding phase is set as

$$\boldsymbol{s} = \boldsymbol{G}\boldsymbol{y} \tag{5.22}$$

Where $\boldsymbol{s} \in \mathbb{R}^{n_u \times 1}$ is the sliding plane, $G \in \mathbb{R}^{n_u \times n_y}$ is needing to be determined in the rest sections of this chapter

Now propose the input of the system is

$$\boldsymbol{u} = -(\boldsymbol{GCB_N})^{-1}\boldsymbol{Gy} - (\boldsymbol{GCB_N})^{-1} ksat(\boldsymbol{s}) \tag{5.23}$$

Then we derivative the equation

$$\dot{\boldsymbol{s}} = \boldsymbol{G}\dot{\boldsymbol{y}} = \boldsymbol{GC}\dot{\boldsymbol{x}} = \boldsymbol{GC}[\boldsymbol{Ax} + \boldsymbol{B_N u} + \boldsymbol{B_N \xi_H(t)x} + \boldsymbol{B_N \xi_B(t)u} + \boldsymbol{B_N \xi_F(t)}] \quad (5.24)$$

Then substituting the proposed input equation (5.23) into equation (5.22), which is metamorphosed as

$$\begin{aligned}\dot{\boldsymbol{s}} = \boldsymbol{GC}\{&\boldsymbol{Ax} + \boldsymbol{B_N}[-(\boldsymbol{GCB_N})^{-1}\boldsymbol{GCx} + (\boldsymbol{GCB_N})^{-1}ksat(\boldsymbol{s})] + \boldsymbol{B_N \xi_H(t)x} \\ &+ \boldsymbol{B_N \xi_B(t)}[-(\boldsymbol{GCB_N})^{-1}\boldsymbol{GCx} + (\boldsymbol{GCB_N})^{-1}ksat(\boldsymbol{s})] \\ &+ \boldsymbol{B_N \xi_F(t)}\}\end{aligned} \quad (5.25)$$

Suppose the Lyapunov function is

$$\boldsymbol{V} = \frac{\boldsymbol{1}}{\boldsymbol{2}}\boldsymbol{s^T s} \quad (5.26)$$

Thus, the Lyapunov stability is valid if the condition in equation (5.16) is matched

$$\dot{\boldsymbol{V}} = \boldsymbol{s^T}\dot{\boldsymbol{s}} < \boldsymbol{0} \quad (5.27)$$

Then substituting the equation (5.25) to equation (5.27), we have the definition for *k* that is,

$$\boldsymbol{k} > \frac{\|\boldsymbol{GC(A + H(t) - I(1 + \xi_B(t)))}\|\|\boldsymbol{x}\| + \|\boldsymbol{GCF(t)}\|}{\|\boldsymbol{1 + \xi_B(t)}\|} \quad (5.28)$$

The above equation is the definition of *k* for reaching a condition of the sliding mode control. As long as the reaching condition in equation (5.28) is satisfied, it shows that $s \to 0 \; as \; t \to \infty$. Therefore, the sliding surface is 0 when the states of the system reach the sliding plane.

However, the $\|\boldsymbol{x}\|$ are not measurable since this is an output feedback system. therefore, the simple adaption law is used here to estimate the upper bound.

Previous research (Pai & Sinha, 2006) proposed a form of the estimation of the upper bound of $\|\boldsymbol{x}\|$. Assume that

$$\|\boldsymbol{x}\| \le \boldsymbol{\delta_x} \tag{5.29}$$

Let

$$\boldsymbol{k} > \eta = \frac{\alpha_1 + \alpha_2\|\boldsymbol{x}\|}{L} \tag{5.30}$$

Where

$$\alpha_1 = \|\boldsymbol{GCF}(\boldsymbol{t})\| \tag{5.31}$$

$$\alpha_2 = \|\boldsymbol{GC}(\boldsymbol{A} + \boldsymbol{H}(\boldsymbol{t}) - \boldsymbol{I}(\boldsymbol{1} + \boldsymbol{\xi_B}(\boldsymbol{t})))\| \tag{5.32}$$

$$L = \|\boldsymbol{1} + \boldsymbol{\xi_B}(\boldsymbol{t})\| \tag{5.33}$$

Let $\widehat{\boldsymbol{\delta}}_{\boldsymbol{x}}$ be the estimation of the upper bound $\boldsymbol{\delta_x}$**,** then

$$\boldsymbol{\delta_x} \le \widehat{\boldsymbol{\delta}}_{\boldsymbol{x}} \tag{5.34}$$

Then define

$$\boldsymbol{k} \ge \hat{\eta} = \frac{\alpha_1 + \alpha_2\widehat{\boldsymbol{\delta}}_{\boldsymbol{x}}}{L} \tag{5.35}$$

Then let

$$\tilde{\eta} = \hat{\eta} - \eta = \frac{\alpha_2\left(\widehat{\boldsymbol{\delta}}_{\boldsymbol{x}} - \boldsymbol{\delta_x}\right)}{L} = \frac{\alpha_2\widetilde{\boldsymbol{\delta}}_{\boldsymbol{x}}}{L} \tag{5.36}$$

Now assume that

$$\dot{\widetilde{\boldsymbol{\delta}}}_{\boldsymbol{x}} = \frac{\alpha_2}{\boldsymbol{\tau}}\int_{\boldsymbol{0}}^{\boldsymbol{t}}\|\boldsymbol{s}\|\,\boldsymbol{dt} \tag{5.37}$$

Because of that $\boldsymbol{\delta_x}$ positive constant scalar. Then

$$\dot{\hat{\boldsymbol{\delta}}}_{\boldsymbol{x}} = \dot{\tilde{\boldsymbol{\delta}}}_{\boldsymbol{x}} \tag{5.38}$$

Therefore, the estimation $\hat{\boldsymbol{\delta}}_{\boldsymbol{x}}$ can be transformed as in equation

$$\hat{\boldsymbol{\delta}}_{\boldsymbol{x}} = \tilde{\boldsymbol{\delta}}_{\boldsymbol{x}} = \tilde{\boldsymbol{\delta}}_{\boldsymbol{x0}} + \frac{\alpha_2}{\boldsymbol{\tau}}\|\boldsymbol{s}\| \tag{5.39}$$

Assume the new input form as in equation

$$\boldsymbol{u} = -(\boldsymbol{GCB_N})^{-1}\boldsymbol{Gy} - (\boldsymbol{GCB_N})^{-1}(\hat{\eta} + \sigma)sat(\boldsymbol{s}) \tag{5.40}$$

Where σ is a positive scalar.

The sliding surface that is revised in the function of the new state **z** is expressed in equation (5.18)

$$\boldsymbol{s} = \boldsymbol{Gy} = \boldsymbol{G}[\boldsymbol{\bar{C}_1} \quad \boldsymbol{\bar{C}_1}]\begin{bmatrix}\boldsymbol{z_1}\\ \boldsymbol{z_2}\end{bmatrix} \tag{5.41}$$

When the system reaches the sliding phase and stays on it we have

$$\boldsymbol{s} = \boldsymbol{G\bar{C}_1 z_1} + \boldsymbol{G\bar{C}_2 z_2} = \boldsymbol{0} \tag{5.42}$$

Then we can have the $\boldsymbol{z_2}$ is the function of $\boldsymbol{z_1}$

$$\boldsymbol{z_2} = -(\boldsymbol{G\bar{C}_2})^{-\boldsymbol{1}}\boldsymbol{G\bar{C}_1 z_1} \tag{5.43}$$

Now substituting above equation into state equation in equation (5.21), which is revised as

$$\dot{\boldsymbol{z}}_{\boldsymbol{1}} = (\boldsymbol{\bar{A}_{11}} - \boldsymbol{\bar{A}_{12}}(\boldsymbol{G\bar{C}_2})^{-\boldsymbol{1}}\boldsymbol{G\bar{C}_1})\boldsymbol{z_1} \tag{5.44}$$

The above equation (5.44) shows that the stability of the system depends on the reduced order system when the system satisfies the matching condition and the reaching condition, then the system reaches the sliding plane and stays on it.

Therefore, the $\boldsymbol{G}$ need to be determined to stabilize the reduced order system in equation (5.44)

5.3 LQR for the Reduced Order System

The previous section presents that the stability of the system when it reaches the sliding surface depends on the reduced order system that is shown in equation (5.44). Assuming that:

$$(\boldsymbol{G}\overline{\boldsymbol{C}}_{\boldsymbol{2}})^{-\boldsymbol{1}}\boldsymbol{G}\overline{\boldsymbol{C}}_{\boldsymbol{1}} = \boldsymbol{K} \tag{5.45}$$

Then the reduced order system is transformed as

$$\dot{\boldsymbol{z}}_{\boldsymbol{1}} = (\overline{\boldsymbol{A}}_{\boldsymbol{11}} - \overline{\boldsymbol{A}}_{\boldsymbol{12}}\boldsymbol{K})\boldsymbol{z}_{\boldsymbol{1}} \tag{5.46}$$

And let

$$\boldsymbol{G}_{\boldsymbol{lqr}} = (\boldsymbol{G}\overline{\boldsymbol{C}}_{2})^{-1}\boldsymbol{G} = \boldsymbol{K}\overline{\boldsymbol{C}}_{\boldsymbol{1}}{}^{-\boldsymbol{1}} \tag{5.47}$$

Therefore, the problem of determination of $\boldsymbol{G}$ can be replaced by a new problem of determination of the LQR gain $\boldsymbol{K}$ to stabilize the reduced order system.

For a system with the full state feedback control is shown in equation (5.48):

$$\dot{\boldsymbol{z}}_{\boldsymbol{1}} = \boldsymbol{A}\boldsymbol{z}_{\boldsymbol{1}} + \boldsymbol{B}\boldsymbol{u} \tag{5.48}$$

And the input is expressed as

$$\boldsymbol{u} = -\boldsymbol{K}\boldsymbol{z}_{\boldsymbol{1}} \tag{5.49}$$

The performance index is defined as proposed by (Ogata & Yang, 2002)

$$\boldsymbol{J} = \int_{\mathbf{0}}^{\infty} (\boldsymbol{z_1}^* \boldsymbol{Q} \boldsymbol{z_1} + \boldsymbol{z_1}^* \boldsymbol{K}^* \boldsymbol{R} \boldsymbol{K} \boldsymbol{z_1}) \boldsymbol{dt} = \int_{\mathbf{0}}^{\infty} \boldsymbol{z_1}^* (\boldsymbol{Q} + \boldsymbol{K}^* \boldsymbol{R} \boldsymbol{K}) \boldsymbol{z_1} \boldsymbol{dt} \tag{5.50}$$

Let

$$\boldsymbol{z_1}^* (\boldsymbol{Q} + \boldsymbol{K}^* \boldsymbol{R} \boldsymbol{K}) \boldsymbol{z_1} = -\frac{\boldsymbol{d}}{\boldsymbol{dt}} (\boldsymbol{z_1}^* \boldsymbol{P} \boldsymbol{z_1}) = -\dot{\boldsymbol{z}}_1^* \boldsymbol{P} \boldsymbol{z_1} - \boldsymbol{z_1}^* \boldsymbol{P} \boldsymbol{x} \dot{\boldsymbol{z}}_1 \tag{5.51}$$

Then the equation (5.50) can be organized as

$$-(\boldsymbol{Q} + \boldsymbol{K}^* \boldsymbol{R} \boldsymbol{K}) = (\boldsymbol{A} - \boldsymbol{B} \boldsymbol{K})^* \boldsymbol{P} + \boldsymbol{P} (\boldsymbol{A} - \boldsymbol{B} \boldsymbol{K}) \tag{5.52}$$

And the ***R*** is a positive-definite and real symmetric matrix, it can be written in equation (5.53)

$$\boldsymbol{R} = \boldsymbol{T}^* \boldsymbol{T} \tag{5.53}$$

Then equation (5.52) can be rewritten as

$$\begin{aligned} &\boldsymbol{A}^* \boldsymbol{P} + \boldsymbol{P} \boldsymbol{A} + [\boldsymbol{T} \boldsymbol{K} - (\boldsymbol{T}^*)^{-1} \boldsymbol{B}^* \boldsymbol{P}]^* [\boldsymbol{T} \boldsymbol{K} - (\boldsymbol{T}^*)^{-1} \boldsymbol{B}^* \boldsymbol{P}] - \boldsymbol{P} \boldsymbol{B} \boldsymbol{R}^{-1} \boldsymbol{B}^* \boldsymbol{P} + \boldsymbol{Q} \\ &= \mathbf{0} \end{aligned} \tag{5.54}$$

To minimize the performance index $\boldsymbol{J}$ requiring that the minimization of $[\boldsymbol{T} \boldsymbol{K} - (\boldsymbol{T}^*)^{-1} \boldsymbol{B}^* \boldsymbol{P}]^* [\boldsymbol{T} \boldsymbol{K} - (\boldsymbol{T}^*)^{-1} \boldsymbol{B}^* \boldsymbol{P}]$, The minimization of which is zero. Therefore, the K can be obtained as

$$\boldsymbol{K} = \boldsymbol{T}^{-1} (\boldsymbol{T}^*)^{-1} \boldsymbol{B}^* \boldsymbol{P} = \boldsymbol{R}^{-1} \boldsymbol{B} \boldsymbol{P} \tag{5.55}$$

If there is such a $\boldsymbol{K}$ matrix to stabilize the $\boldsymbol{A} - \boldsymbol{B} \boldsymbol{K}$, then there exists a positive-definite matrix ***P*** satisfies the reduced matrix Riccati Equation (5.56)

$$\boldsymbol{A}^* \boldsymbol{P} + \boldsymbol{P} \boldsymbol{A} - \boldsymbol{P} \boldsymbol{B} \boldsymbol{R}^{-1} \boldsymbol{B}^* \boldsymbol{P} + \boldsymbol{Q} = \mathbf{0} \tag{5.56}$$

As proposition 3.1 proposed by (El-Khazali & Decarlo, 1995) that $\boldsymbol{G} = \boldsymbol{G}_{lqr}$ is an optional solution for the gain of the sliding plane. Then the gain matrix $\boldsymbol{G}$ in the sliding surface is determined to stabilize the reduced order system.

5.4 Conclusion

This chapter introduces the hybrid SMC/LQR control algorithm for the torsional control of the driveline system. The input proposed in this chapter could be pure torque, moreover, it could also be applied to any actuator model that is coupled with the driveshaft system, as long as the input matrix is constant. Additionally, the numerical approximate linear time-varying system is proposed for the controller design. Since the system is output feedback, the adaptive controller is used in this chapter instead of the observer. Therefore, this method reduces the complication of the controller. The method LQR is proposed to determine the sliding surface gain matrix, this is the benefit for the controller design for the most general cases.

Chapter 6

TORSIONAL CONTROL ANALYSIS FOR ROTOR SYSTEM WITH DYNAMIC MISALIGNMENT CONDITION

6.1 Introduction

Using the previously proposed hybrid SMC/LQR control strategy to drive the shaft system as the continuous acceleration as the same rate as mentioned in chapter III. The purpose of this controller designed to drive the nonlinear driveshaft system to overcome any possible resonance frequency and speed limit under different misalignment conditions. The classic PID controller is applied on the nonlinear drive shaft system for the torque control as the comparison with the proposed hybrid SMC/LQR controller. Firstly, two structures of the PID controllers are introduced to control the driveshaft system under two misalignment conditions. Then the SMC/LQR controller is also applied to the nonlinear system under the same misalignment conditions. Finally, the response of the lateral misalignment angle, twist angle, and output speed are used to be compared between two controllers under all misalignment conditions. Only the 3-DOF model is used in this chapter coupling with the controller.

6.2 PID Controller

The PID controller is widely applied to industrial products for its easy to design and the wide valid range. This type of controller is also applied for the torque input control. The sensors are supposed to measure the rotation angle and speed of input shaft, and lateral movement and rate, so that two variable value are able for the feedback tracking control with the PID controller. Two structures of the PID controller are designed in this section. The structure I of the controller that is shown in Figure 6.1 driving the shaft system using only the input speed error. Since there are more variable measurable, therefore, the second structure of the controller is designed. Figure 6.2 shows the structure II of the PID controller. The errors of the input speed and the misalignment deflections are calculated through the PID controller for the torque control.

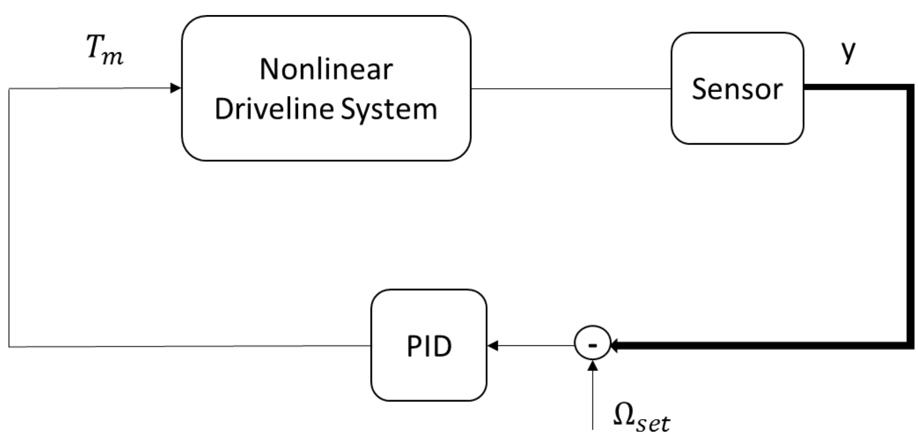

Figure 6.1 Structure of the PID Controller I

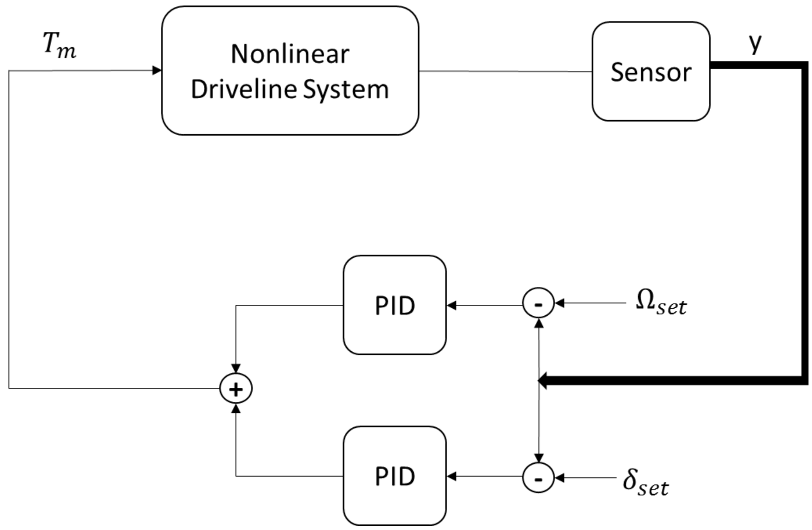

Figure 6.2 Structure of the PID Controller II

As the similar conditions as previous simulations in chapter III, the load torque is assumed to be divided as the viscous and static parts. Only the viscous load torque is considered in the following simulation.

The input of the PID controller I is assumed as equation (6.1)

$$T_m = K_p e_1 + K_i \int_0^t e_1(\tau) d\tau + K_d \dot{e}_1 \tag{6.1}$$

Then the input of structure II is determined as equation (6.2)

$$T_m = \sum_{n=1}^{2} K_p e_n + K_i \int_0^t e_n(\tau) d\tau + K_d \dot{e}_n \tag{6.2}$$

Where the error is set as equation (6.3) and (6.4)

$$e_1 = \Omega_{set} - \dot{\phi} \tag{6.3}$$

$$e_2 = \delta_{set} - \delta \tag{6.4}$$

The results from Figure 6.3 to Figure 6.5 response of the perturbation dynamic misalignment angle, twist angle, and output speed responses of the driveline system. First, the driveline is driven by the PID controller to passage through the critical speed with a 15º static misalignment angle. As the previous result shows in Figure 3.14 the Sommerfeld effect with a constant torque input and a viscous load torque as the speed spinup rate as 2 rad/s^2. Figure 6.3 shows the simulation result under the same parametric condition with the controlled torque input instead of the constant torque input. The speed response indicates the driveline system passage through the critical speed smooth with the controlled input torque. Figure 6.4 shows the speed response under the 35º static misalignment angle with the same controller I. There is a resonance phenomenon in either twist and lateral motion. To suppress the resonance, the controller II is designed to control torque by having more variable involving. Figure 6.5 shows the simulation result of the driveline system driven by controller II that shows the resonance is not obvious suppressed with the increasing power consumed.

Therefore, the simulation results show that the PID controller is capable of ensuring the smooth acceleration under the small static misalignment condition. The lateral critical frequency is not overcome with either controller I or controller II. Referring to the results in chapter 3, the lateral motion is stabilizing the torsional motion under the large misalignment condition. A proper controller that is capable of the smooth acceleration under the large misalignment condition is required.

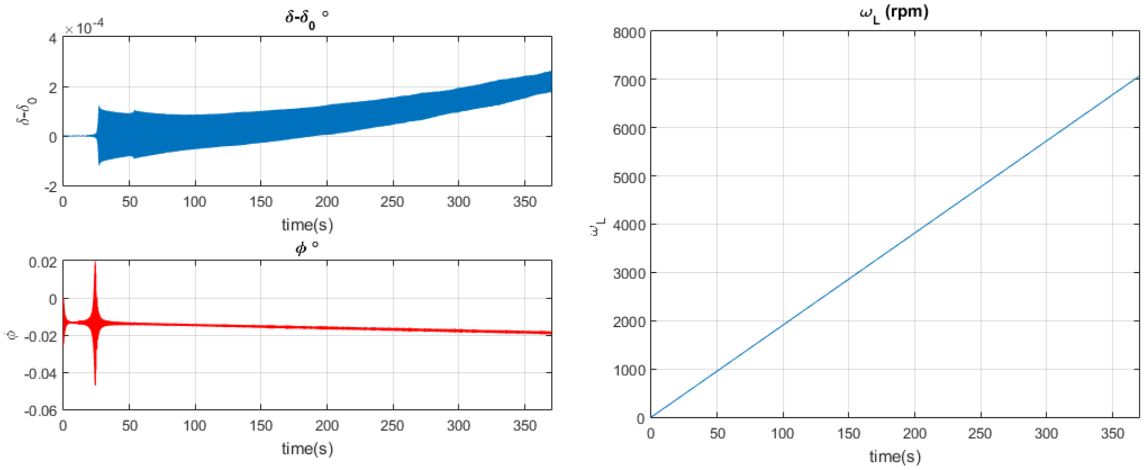

Figure 6.3 PID Controller Supercritical Case: $\delta_0 = 15°$

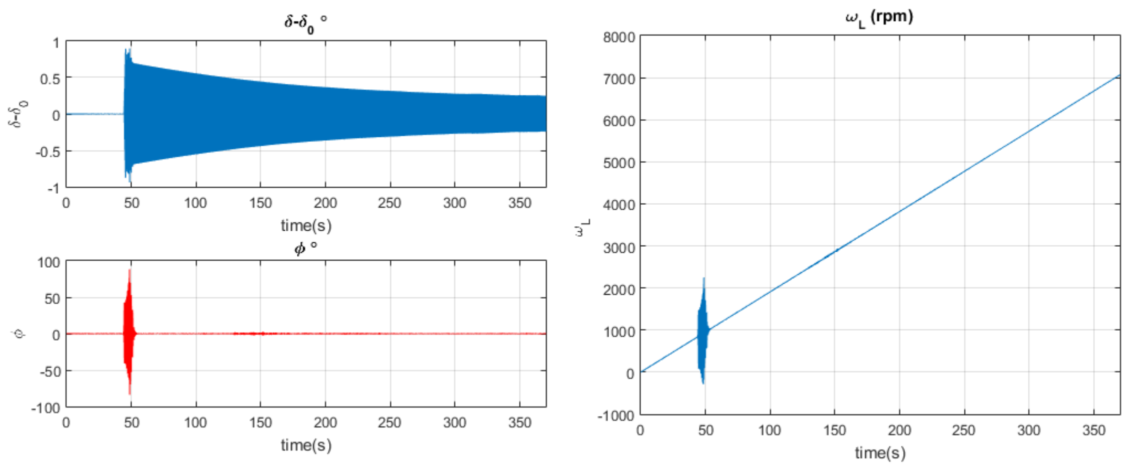

Figure 6.4 PID Controller I Supercritical Case: $\delta_0 = 35°$

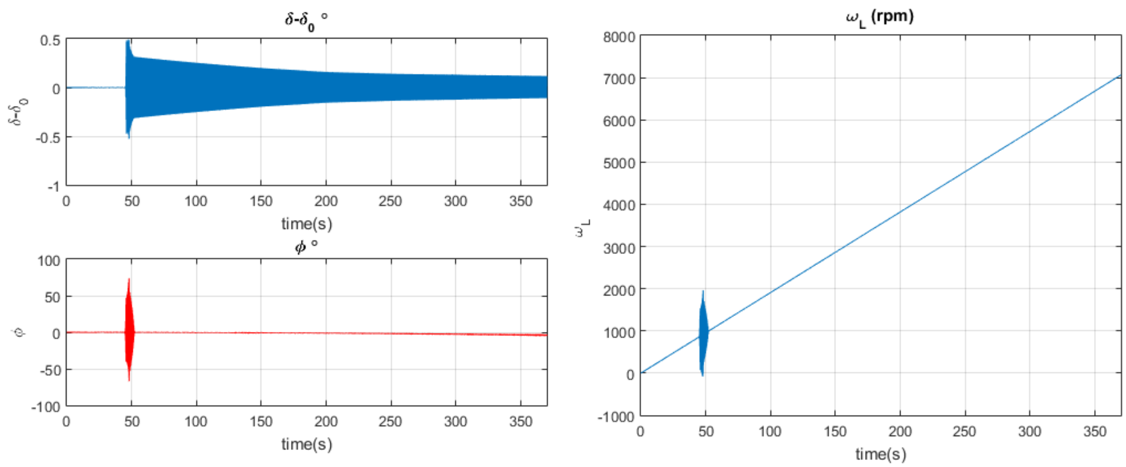

Figure 6.5 PID Controller II Supercritical Case: $\delta_0 = 35°$

6.3 Rotor System in Dynamic Misalignment Condition with SMC

The hybrid SMC/LQR controller is applied to control the driveline system to accelerate at the spinup rate as 2 rad/s^2. The simulation conditions are the same as the previous section only with the different type of controller.

Figure 6.6 shows the result with the 15^o static misalignment angle. The smooth passage through the critical speed is indicated as a similar result as the PID controller case. The significant difference between the results with these two controllers occurs under the large static misalignment angle condition. The speed response shown in Figure 6.7 indicates the smooth passage through the critical speed as similar to the result in Figure 6.6. However, the power consumed for the precise speed tracking control is relatively larger compared with the previous result in Figure 6.6.

The comparison of the output speed error and the power consumed between the two proposed controllers are shown in Figure 6.8 and Figure 6.9. The output speed error is the difference between the output speed and reference speed.

Figure 6.8 shows that both controllers are able to drive the driveline system with the excellent tracking performance under small static misalignment angle case. The speed error with hybrid SMC/LQR is lower with the relative larger power consumed. Figure 6.9 shows the advantage of the proposed SMC strategy that is the relatively lower power consumed to reach the significant better tracking performance on rotating speed.

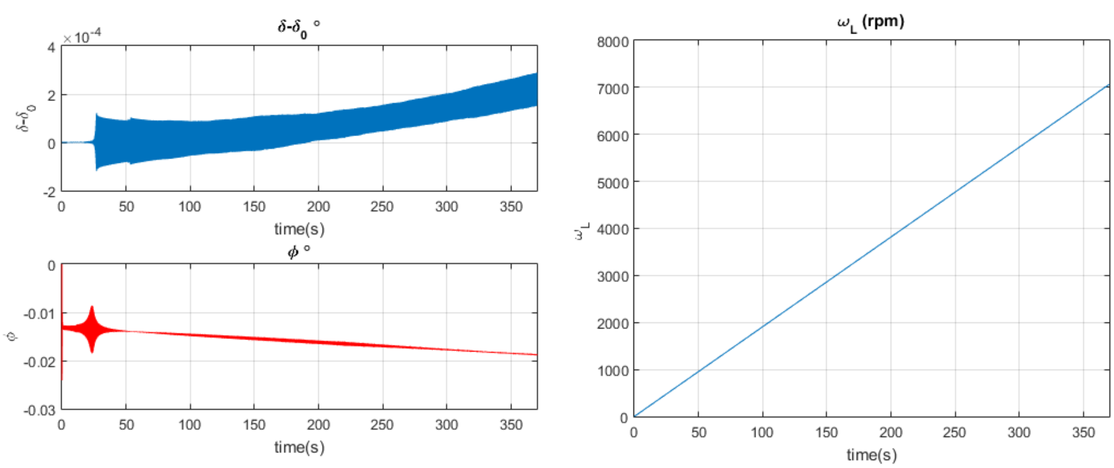

Figure 6.6 SMC/LQR Supercritical Case: $\delta_0 = 15°$ (Supercritical)

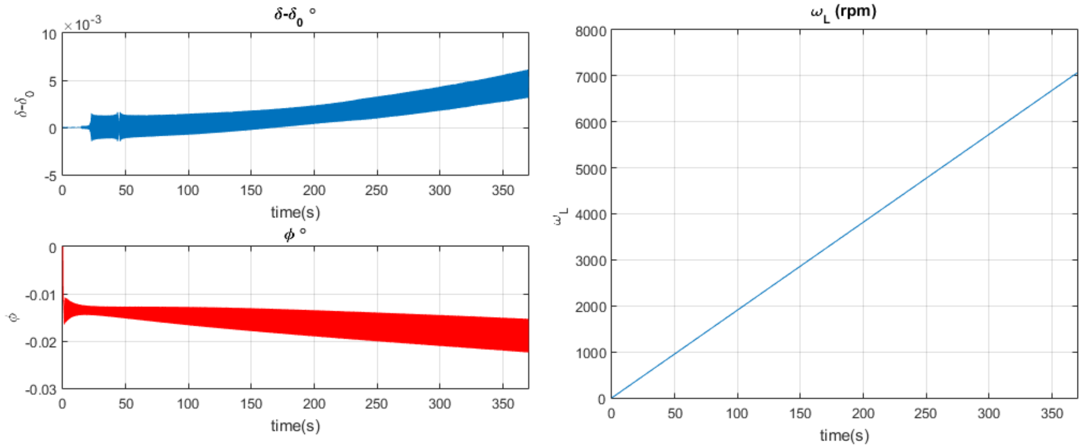

Figure 6.7 SMC/LQR Supercritical Case: $\delta_0 = 35°$ (Supercritical)

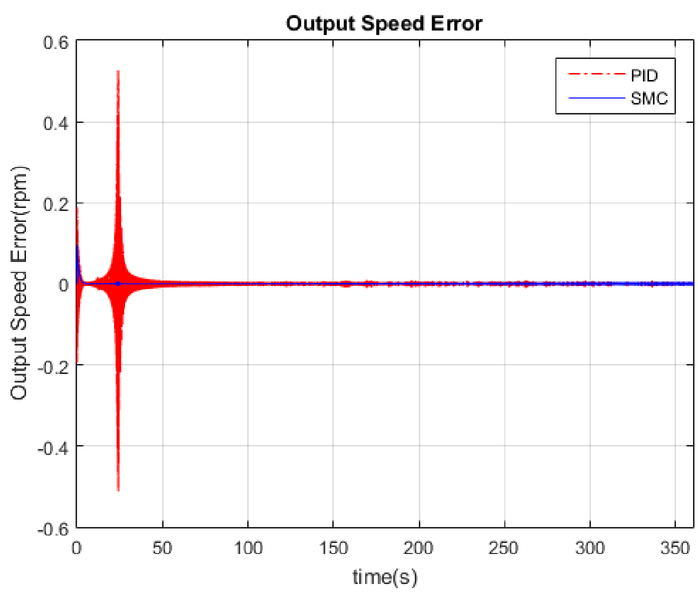

Figure 6.8 Angular Velocity Error Comparison: $\delta_0 = 15°$ (Supercritical)

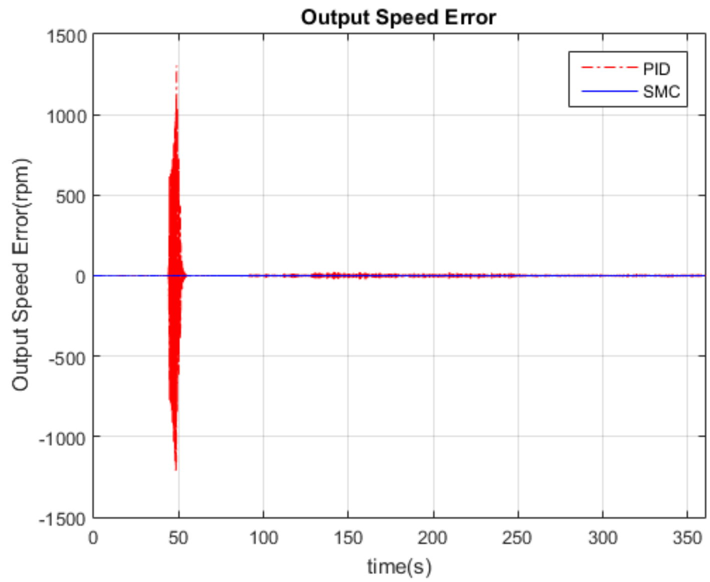

Figure 6.9 Angular Velocity Error Comparison: $\delta_0 = 35°$ (Supercritical)

6.4 Conclusion

This chapter indicates the numerical results of the output rotating speed of the original full nonlinear driveshaft model with the hybrid SMC/LQR controller that is proposed in Chapter 6. The result is also compared with the PID controller. As the results show, the PID controller has a similar capability with SMC/LQR controller under the small misalignment angle condition. However, the PID controller is not capable of driving the nonlinear driveshaft system through the resonance speed under the large misalignment angle condition, as the same time, the SMC/LQR controller performs the extraordinary capability of the driving through the resonance speed. The results illustrate that the controller designed base on the approximate LTV system is precise enough for controlling the nonlinear system.

Chapter 7
CONTROLLER DESIGN FOR THE LIMITED POWER SUPPLIER

7.1 Introduction

The electrical motor is becoming the most popular power source currently due to the environmental issues and the electricity storage technology development. For the practical application, the power supply is always limited and considered as non-idea. The DC motor is considered as the limited power in this chapter. Firstly, the DC model is proposed, validated by integrated of the nonlinear 3-DOF driveline system for the Sommerfeld effect. Then the hybrid control method is designed for the integration of the driveline model and the power source to drive the 3-DOF nonlinear driveline system passage through the resonance under the limited power condition. In this chapter, the input provided from the controller is the supply voltage of the DC motor supplanting the pure torque input. The PID controller is also used in this chapter for the comparison with the hybrid controller under the large static misalignment condition.

7.2 DC Motor Model Development

The general DC motor structure is shown in Figure 7.1. The DC motor parameters are shown in Table 7.1 The equations for the electrical side of the system are

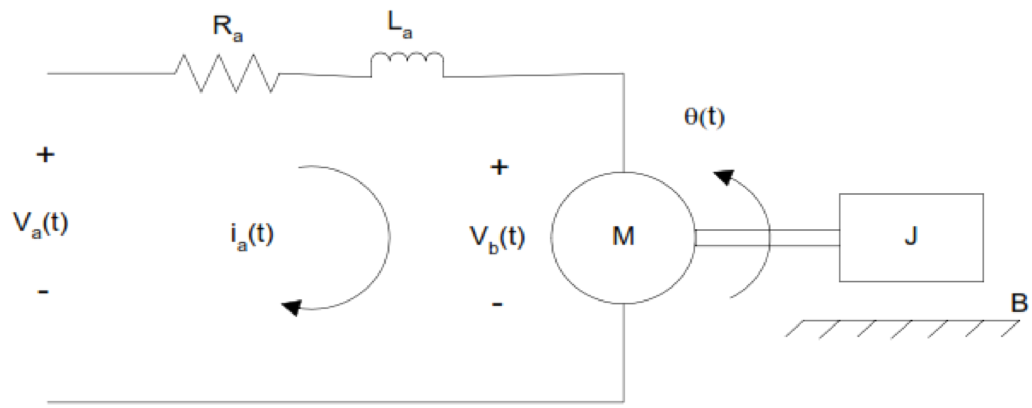

Figure 7.1 DC Motor Structure

$$V_a(t) = L_a \frac{di_a(t)}{dt} + i_a(t)R_a + V_b(t) \tag{7.1}$$

With

$$V_b(t) = k_b \frac{d\theta(t)}{dt} \tag{7.2}$$

Such that we have

$$V_a(t) = L_a \frac{di_a(t)}{dt} + i_a(t)R_a + k_b \frac{d\theta(t)}{dt} \tag{7.3}$$

L_a is the inductance, k_b is the motor's back EMF constant, i_a is the current of the DC circuit, and V_a is the supply voltage for the DC motor.

The equations for the mechanical side of the system are

$$T(t) = J \frac{d^2\theta(t)}{dt^2} + b \frac{d\theta(t)}{dt} \tag{7.4}$$

With

$$T(t) = k_t i_a(t) \tag{7.5}$$

Table 7.1 DC Motor Parameters

K_a	4 V/(rad/s)
k_t	22.7Nm/A
k_b	0.0227V/(rad/s)
L_a	27.6 h
R_a	0.87Ω

Therefore, the equation of the mechanical system side is shown in (7.6)

$$J\frac{d^2\theta(t)}{dt^2} + b\frac{d\theta(t)}{dt} = k_t i_a(t) \qquad (7.6)$$

k_t is the torque constant that relates the torque to the armature current, T is the applied torque. Supply voltage V_a is the input for the DC motor.

7.3 Numerical Simulation Results

This section shows the numerical results of driving the nonlinear driveline system with different voltage. The speed limit is still presented in the subcritical case from Figure 7.2 to Figure 7.4. However, the speed limit occurs in this section not only due to the nonlinear phenomenon that is presented in chapter 4, but the power limit also has an effect on the output speed. Figure 7.2 illustrates the speed limit is due to the power limit since the curve is gradually increasing to the limit, not like the curve in Figure 7.3 with 6V input voltage, or the curve in Figure 7.4. with 15V and 20V input voltage. These curves illustrate that the speed limit happened in the system due to the nonlinear property shown in chapter 4. In these cases, the torque comes from the DC motor is not sufficient enough to passage the critical speed region. The curve in Figure 7.4 with 25V voltage input illustrates that the driveshaft will passage the speed limit with the sufficient large torque. There is the jump phenomenon observed in this figure when the speed passage the critical speed region. The similar results of the supercritical case are also obtained with $\delta_0 = 25°$, which are shown in Figure 7.5 and Figure 7.6. Both capture and passage phenomena are illustrated in Figure 7.5. The speed limit is observed with the input voltage as 5V and 15V. The speed limits are close to the critical frequency when the input voltage is enlarged to 25V and 30V, especially with the 30V input, the provided torque is close sufficient to the critical value overcome the critical frequencies. The detailed clarion curves are shown in Figure 7.6

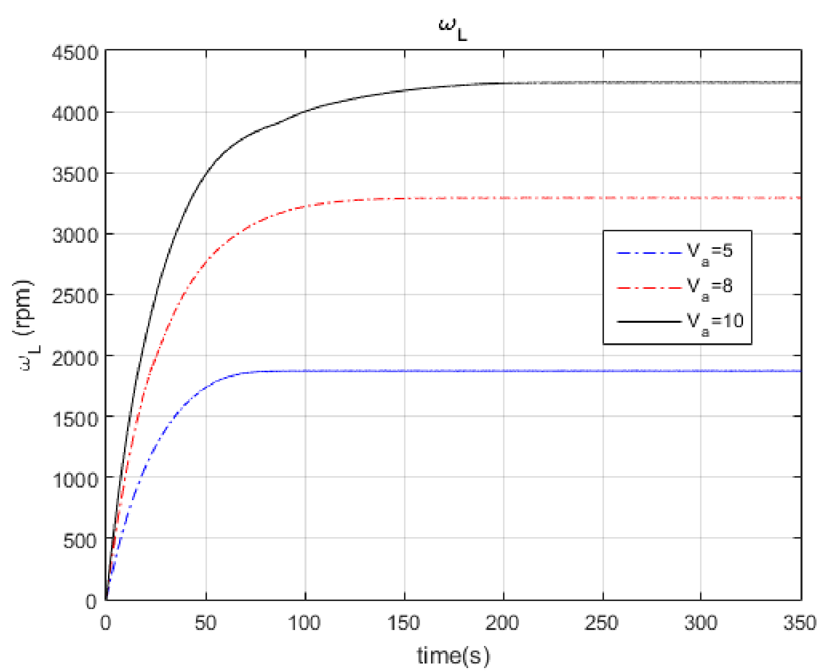

Figure 7.2 Input Voltage from 5V to 10V: $\delta_0 = 12°$ (subcritical)

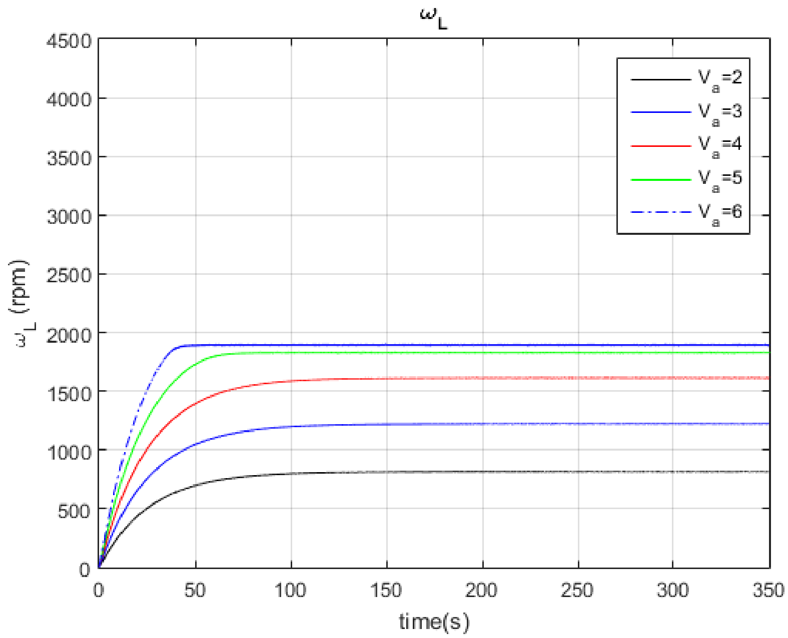

Figure 7.3 Input Voltage from 2V to 6V: $\delta_0 = 15°$ (subcritical)

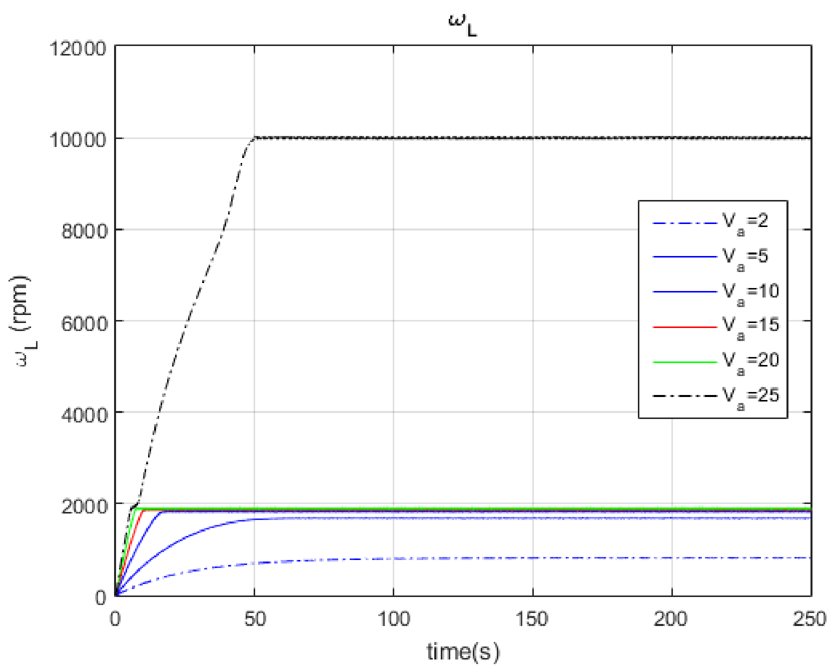

Figure 7.4 Input Voltage from 2V to 25V: $\delta_0 = 25°$ (subcritical)

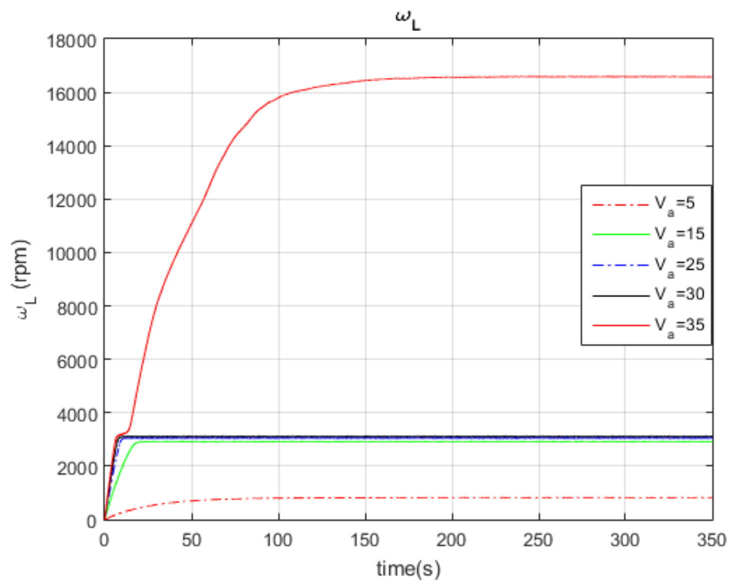

Figure 7.5 Input Voltage from 5V to 35V: $\delta_0 = 25°$ (supercritical)

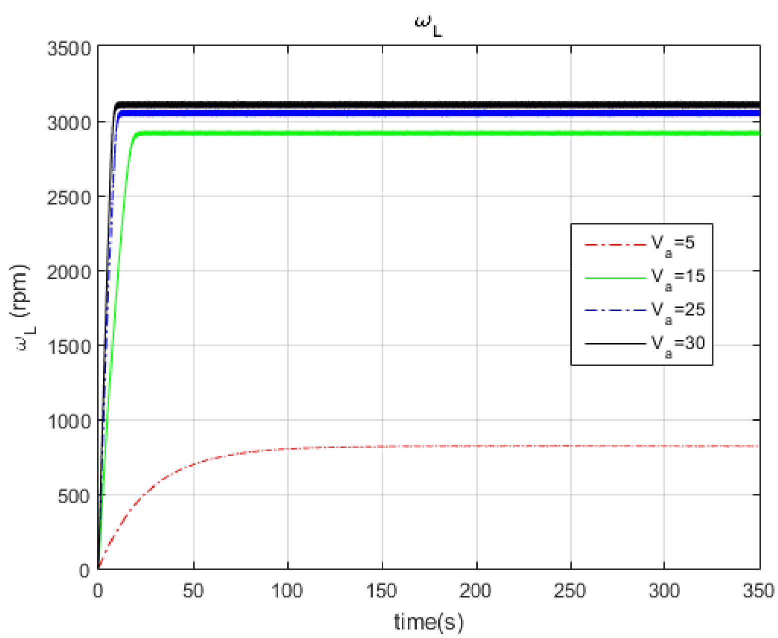

Figure 7.6 Input Voltage from 5V to 30V: $\delta_0 = 25°$ (supercritical)

7.4 DC Motor with PID Controller

Then the designed controller is desired to adjust the driveline rotating speed through varying the supply voltage of the motor. Figure 7.7 shows the simple supply voltage PID controller combining with the DC motor.

The speed error is the only variable involved in the tracking control. The output voltage is assumed as a saturated value for the DC motor, which indicates that the power source is still the limited even coupling with the controller.

$$e_1(t) = \dot{\theta}(t) - \dot{\theta}_{set}(t) \tag{7.7}$$

$$e_V(t) = K_p e_1 + K_i \int_0^t e_1(\tau) d\tau + K_d \dot{e}_1 \tag{7.8}$$

$$V_a(t) = e_V(t) K_a \tag{7.9}$$

$$V_a(t) = L_a \frac{di_a(t)}{dt} + i_a(t) R_a + V_b(t) \tag{7.10}$$

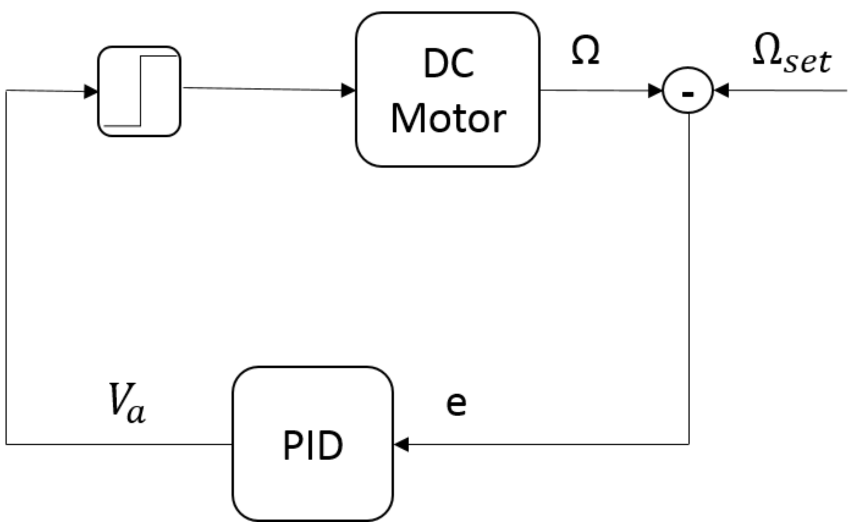

Figure 7.7 Simple DC motor with a PID controller

With

$$V_b(t) = k_b \frac{d\theta(t)}{dt} \tag{7.11}$$

Such that we have

$$e_V(t)K_a = L_a \frac{di_a(t)}{dt} + i_a(t)R_a + k_b \frac{d\theta(t)}{dt} \tag{7.12}$$

Where k_b is the motor's back EMF constant. V_a is the supply voltage for the DC motor, K_a is the voltage constant. The equations for the mechanical part of the system are

$$T(t) = J \frac{d^2\theta(t)}{dt^2} + b \frac{d\theta(t)}{dt} \tag{7.13}$$

Therefore, we have

$$J \frac{d^2\theta(t)}{dt^2} + b \frac{d\theta(t)}{dt} = K_t i_a(t) \tag{7.14}$$

In the simulation of this section, assume that the motor operates under the steady state condition, then the inductance is not involved. The input of the system is the torque which is determined in equation (7.15)

$$T_m = k_t i_a(t) = \frac{k_t e_V(t) K_a - k_t k_b \dot{\phi}}{R_a} \tag{7.15}$$

7.5 Sliding Model Controller with Limited Power

The input of the driveshaft system is assumed as the direct torque came from the SMC/LQR controller in chapter 7. In this chapter, the DC motor is modeled as the actuator for the driveshaft model, the voltage of the DC motor is assumed as an input of the system instead of the torque shown in Figure 7.8.

The input torque T_m is expressed in equation

$$T_m = \frac{k_t V_a - k_t k_b \dot{\phi}}{R_a} \tag{7.16}$$

Then substituting the equation (7.16) into the equation (2.50), therefore the equation (4.15) is written in equation (7.17)

$$\widehat{\boldsymbol{Q}}_{\boldsymbol{f}} = \widehat{\boldsymbol{B}}_{\boldsymbol{u}}\boldsymbol{u} + \widehat{\boldsymbol{Q}}_{\boldsymbol{F}} = \begin{bmatrix} \frac{k_t}{R_a} \\ 0 \\ 0 \end{bmatrix} V_a + Q_F - \begin{bmatrix} \frac{k_t k_b}{R_a} \\ 0 \\ 0 \end{bmatrix} \Omega = \widehat{\boldsymbol{B}}_{\boldsymbol{u}}\boldsymbol{u} + \widehat{\boldsymbol{Q}}_{\boldsymbol{F}} \tag{7.17}$$

Then the system dynamics in equation (4.14) is written as

$$\begin{gathered}[\boldsymbol{M} + \Delta\boldsymbol{M}(t)]\ddot{q}_h + [\boldsymbol{Cd} + \Delta\boldsymbol{Cd}(t) + \boldsymbol{Cd}_{\boldsymbol{M}}]\dot{q}_h + [\boldsymbol{K} + \Delta\boldsymbol{K}(t) - \boldsymbol{K}_{\boldsymbol{Q}} \\ - \Delta\boldsymbol{K}_{\boldsymbol{Q}}(t)]q_h = \widehat{\boldsymbol{Q}}_{\boldsymbol{f}} + \Delta\boldsymbol{Q}_{\boldsymbol{f}}(t) - \boldsymbol{f} - \Delta\boldsymbol{f}(t)\end{gathered} \tag{7.18}$$

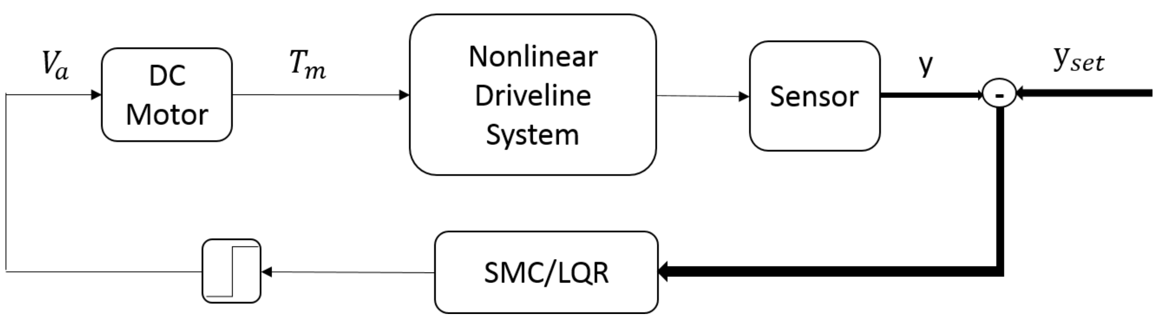

Figure 7.8 DC Motor with SMC/LQR Controller

Where $\boldsymbol{Cd_M}$ is

$$\boldsymbol{Cd_M} = \begin{bmatrix} \frac{k_t k_b}{R_a} & 0 & 0 \\ 0 & 0 & 0 \\ 0 & 0 & 0 \end{bmatrix} \tag{7.19}$$

Where $\widehat{\boldsymbol{Q}}_{\boldsymbol{f}}$ is defined as

$$\widehat{\boldsymbol{Q}}_{\boldsymbol{f}} = \widehat{\boldsymbol{B}}_{\boldsymbol{u}}\boldsymbol{u} + \widehat{\boldsymbol{Q}}_{\boldsymbol{F}} \tag{7.20}$$

And then let

$$\begin{gathered} \widehat{\boldsymbol{Q}}_{\boldsymbol{F}}(\boldsymbol{t}) = \widehat{\boldsymbol{Q}}_{\boldsymbol{F}} + \Delta\boldsymbol{Q}_{\boldsymbol{f}}(t) \\ \boldsymbol{F}(\boldsymbol{t}) = \boldsymbol{f} + \Delta\boldsymbol{f}(t) \end{gathered} \tag{7.21}$$

Then the equation (5.3) is rewritten as equation

$$\begin{aligned} \ddot{q}_h &+ [\boldsymbol{I} - \boldsymbol{M}^{-1}\Delta\boldsymbol{M}(t)]\boldsymbol{M}^{-1}[\boldsymbol{Cd} + \Delta\boldsymbol{Cd}(t) + \boldsymbol{Cd_M}]\dot{\boldsymbol{q}}_h \\ &+ [\boldsymbol{I} - \boldsymbol{M}^{-1}\Delta\boldsymbol{M}(t)]\boldsymbol{M}^{-1}[\boldsymbol{K} + \Delta\boldsymbol{K}(t) - \boldsymbol{K_Q} - \Delta\boldsymbol{K_Q}(t)]\boldsymbol{q}_h \\ &= [\boldsymbol{I} - \boldsymbol{M}^{-1}\Delta\boldsymbol{M}(t)]\boldsymbol{M}^{-1}[\widehat{\boldsymbol{B}}_{\boldsymbol{u}}\boldsymbol{u} + \widehat{\boldsymbol{Q}}_{\boldsymbol{F}}(t) - \boldsymbol{F}(\boldsymbol{t})] \end{aligned} \tag{7.22}$$

Now we can transfer the above LTV differential equations into state space form

$$\begin{aligned} \begin{bmatrix} \dot{q}_h \\ \ddot{q}_h \end{bmatrix} &= \begin{bmatrix} \boldsymbol{0} & \boldsymbol{I} \\ \boldsymbol{A_{21}} & \boldsymbol{A_{22}} \end{bmatrix} \begin{bmatrix} q_h \\ \dot{q}_h \end{bmatrix} \\ &+ \begin{bmatrix} \boldsymbol{0} \\ [\boldsymbol{I} - \boldsymbol{M}^{-1}\Delta\boldsymbol{M}(t)]\boldsymbol{M}^{-1}[\widehat{\boldsymbol{B}}_{\boldsymbol{u}}\boldsymbol{u} + \widehat{\boldsymbol{Q}}_{\boldsymbol{F}}(t) - \boldsymbol{F}(\boldsymbol{t})] \end{bmatrix} \end{aligned} \tag{7.23}$$

Where

$$\boldsymbol{A_{21}} = -[\boldsymbol{I} - \boldsymbol{M}^{-1}\Delta\boldsymbol{M}(t)]\boldsymbol{M}^{-1}[\boldsymbol{K} + \Delta\boldsymbol{K}(t) - \boldsymbol{K_Q} - \Delta\boldsymbol{K_Q}(t)] \tag{7.24}$$

$$\boldsymbol{A_{22}} = -[\boldsymbol{I} - \boldsymbol{M}^{-1}\Delta\boldsymbol{M}(t)]\boldsymbol{M}^{-1}[\boldsymbol{Cd} + \Delta\boldsymbol{Cd}(t) + \boldsymbol{Cd_M}] \tag{7.25}$$

Let $\boldsymbol{x} = [\boldsymbol{q}_h{}^T, \dot{\boldsymbol{q}}_h{}^T]^T \in \mathbb{R}^{n_x \times 1}$ is the state vector, and $\boldsymbol{y} \in \mathbb{R}^{n_y \times 1}$ is the output vector.

$$\boldsymbol{A_t} = \begin{bmatrix} \mathbf{0} & \boldsymbol{I} \\ \boldsymbol{A_{21}} & \boldsymbol{A_{22}} \end{bmatrix} \tag{7.26}$$

$\boldsymbol{A_t} \in \mathbb{R}^{n_X \times n_x}$ is the state matrix. As only the output values are measurable, then the output equation is

$$\boldsymbol{y} = \boldsymbol{Cx} \tag{7.27}$$

Where **C**$\in \mathbb{R}^{n_y \times n_x}$ is the output matrix.

After reorganizing the equation (7.22), the system dynamics is expressed in

$$\begin{gathered} \dot{\boldsymbol{x}} = \boldsymbol{Ax} + \widehat{\boldsymbol{B}}_{\boldsymbol{N}}\boldsymbol{u} + \widehat{\boldsymbol{H}}(t)\boldsymbol{x} + \Delta\widehat{\boldsymbol{B}}_{\boldsymbol{N}}(t)\boldsymbol{u} + \widehat{\boldsymbol{F}}_{\boldsymbol{N}}(t) \\ \boldsymbol{y} = \boldsymbol{Cx} \end{gathered} \tag{7.28}$$

The matrices in equation (7.28) are shown in following,

$$\widehat{\boldsymbol{A}} = \begin{bmatrix} \mathbf{0} & \boldsymbol{I} \\ -\boldsymbol{M}^{-1}(\boldsymbol{K} - \boldsymbol{K_Q}) & -\boldsymbol{M}^{-1}(\boldsymbol{Cd} + \boldsymbol{Cd_M}) \end{bmatrix} \tag{7.29}$$

$$\widehat{\boldsymbol{B}}_N = \begin{bmatrix} 0 \\ \boldsymbol{M}^{-1}\widehat{\boldsymbol{B}}_{\boldsymbol{u}} \end{bmatrix} \tag{7.30}$$

$$\widehat{\boldsymbol{H}}(t) = \begin{bmatrix} 0 & I \\ \boldsymbol{H_{21}} & -\boldsymbol{M}^{-1}\Delta\boldsymbol{Cd}(t) + \boldsymbol{M}^{-1}\Delta\boldsymbol{M}(t)\boldsymbol{M}^{-1}[\boldsymbol{Cd} + \Delta\boldsymbol{Cd}(t) + \boldsymbol{Cd_M}] \end{bmatrix} \tag{7.31}$$

With

$$\begin{aligned} \widehat{\boldsymbol{H}}_{\boldsymbol{21}} = -\boldsymbol{M}^{-1}[\Delta\boldsymbol{K}(t) - \Delta\boldsymbol{K_Q}(t)] + \boldsymbol{M}^{-1}\Delta\boldsymbol{M}(t)\boldsymbol{M}^{-1}[\boldsymbol{K} + \Delta\boldsymbol{K}(t) - \boldsymbol{K_Q} \\ - \Delta\boldsymbol{K_Q}(t)] \end{aligned} \tag{7.32}$$

$$\Delta\widehat{\boldsymbol{B}}_N(\boldsymbol{t}) = \begin{bmatrix} 0 \\ -\boldsymbol{M}^{-1}\Delta\boldsymbol{M}(t)\boldsymbol{M}^{-1}\widehat{\boldsymbol{B}}_{\boldsymbol{u}} \end{bmatrix} \tag{7.33}$$

$$\widehat{\boldsymbol{F}}_N(\boldsymbol{t}) = \begin{bmatrix} \mathbf{0} \\ [\boldsymbol{I} - \boldsymbol{M}^{-1}\Delta\boldsymbol{M}(t)]\boldsymbol{M}^{-1}[\widehat{\boldsymbol{Q}}_{\boldsymbol{F}}(\boldsymbol{t}) - \boldsymbol{F}(\boldsymbol{t})] \end{bmatrix} \tag{7.34}$$

The matching condition is essential for the sliding mode control strategy proposed by (Edwards & Spurgeon, 1995). Then transfer the system in equation (7.28) into the numerical approximation form that is valid for the matching condition

$$\begin{gathered}\dot{\boldsymbol{x}} = \widehat{\boldsymbol{A}}\boldsymbol{x} + \widehat{\boldsymbol{B}}_{\boldsymbol{N}}\boldsymbol{u} + \widehat{\boldsymbol{B}}_{\boldsymbol{N}}\hat{\boldsymbol{\xi}}_{\boldsymbol{H}}(\boldsymbol{t})\boldsymbol{x} + \widehat{\boldsymbol{B}}_{\boldsymbol{N}}\hat{\boldsymbol{\xi}}_{\boldsymbol{B}}(\boldsymbol{t})\boldsymbol{u} + \widehat{\boldsymbol{B}}_{\boldsymbol{N}}\hat{\boldsymbol{\xi}}_{\boldsymbol{F}}(\boldsymbol{t}) \\ \boldsymbol{y} = \boldsymbol{C}\boldsymbol{x}\end{gathered} \tag{7.35}$$

Where

$$\begin{gathered}\hat{\boldsymbol{\xi}}_{\boldsymbol{H}}(\boldsymbol{t}) = \widehat{\boldsymbol{B}}_{\boldsymbol{N}}^{-\mathbf{1}}\widehat{\boldsymbol{H}}(t) \\ \hat{\boldsymbol{\xi}}_{\boldsymbol{B}}(\boldsymbol{t}) = \widehat{\boldsymbol{B}}_{\boldsymbol{N}}^{-\mathbf{1}}\Delta\widehat{\boldsymbol{B}}_{\boldsymbol{N}}(t) \\ \hat{\boldsymbol{\xi}}_{\boldsymbol{F}}(\boldsymbol{t}) = \widehat{\boldsymbol{B}}_{\boldsymbol{N}}^{-\mathbf{1}}\boldsymbol{F}(t)\end{gathered} \tag{7.36}$$

$\widehat{\boldsymbol{B}}_{\boldsymbol{N}}^{-\mathbf{1}}$ is the left inverse matrix of $\widehat{\boldsymbol{B}}_{\boldsymbol{N}}$**,** and $\hat{\boldsymbol{\xi}}_{\boldsymbol{H}}(\boldsymbol{t})$

Now suppose a new state vector **z** that is transferred from the original vector **x** is determined as the same as in equation (5.18).

Then the system dynamics are transferred to the equation (7.37)

$$\begin{gathered}\dot{\boldsymbol{z}} = \boldsymbol{T}\widehat{\boldsymbol{A}}\boldsymbol{T}^{-\mathbf{1}}\boldsymbol{z} + \boldsymbol{T}\widehat{\boldsymbol{B}}_{\boldsymbol{N}}\boldsymbol{u} + \boldsymbol{T}\widehat{\boldsymbol{B}}_{\boldsymbol{N}}\hat{\boldsymbol{\xi}}_{\boldsymbol{H}}(\boldsymbol{t})\boldsymbol{T}^{-\mathbf{1}}\boldsymbol{z} + \boldsymbol{T}\widehat{\boldsymbol{B}}_{\boldsymbol{N}}\hat{\boldsymbol{\xi}}_{\boldsymbol{B}}(\boldsymbol{t})\boldsymbol{u} + \boldsymbol{T}\widehat{\boldsymbol{B}}_{\boldsymbol{N}}\hat{\boldsymbol{\xi}}_{\boldsymbol{F}}(\boldsymbol{t}) \\ \boldsymbol{y} = \boldsymbol{C}\boldsymbol{T}^{-\mathbf{1}}\boldsymbol{z}\end{gathered} \tag{7.37}$$

Where

$$\boldsymbol{T}\widehat{\boldsymbol{B}}_{\boldsymbol{N}} = \begin{bmatrix}\mathbf{0}_{(\boldsymbol{n_x}-\boldsymbol{n_u})\times\boldsymbol{n_u}} \\ \widehat{\boldsymbol{B}}\end{bmatrix} \tag{7.38}$$

Where $\widehat{\boldsymbol{B}} \in \mathbb{R}^{n_u\times n_u}$ is the transferred constant input matrix.

Setting the sliding surface as the same form as in equation (5.22)

Then define reaching condition as in equation (7.39)

$$\widehat{\boldsymbol{k}} \geq \hat{\eta}_L = \frac{\alpha + \hat{\alpha}_2 \widehat{\boldsymbol{\delta}}_{\boldsymbol{x}}}{\hat{L}} \tag{7.39}$$

While the reaching condition is satisfied, the input of the system is the equation (7.42).

$$\hat{\alpha}_2 = \left\| \boldsymbol{GC}(\boldsymbol{A} + \widehat{\boldsymbol{H}}(\boldsymbol{t}) - \boldsymbol{I}(\boldsymbol{1} + \hat{\boldsymbol{\xi}}_{\boldsymbol{B}}(\boldsymbol{t}))) \right\| \tag{7.40}$$

$$\hat{L} = \left\| \boldsymbol{1} + \hat{\boldsymbol{\xi}}_{\boldsymbol{B}}(\boldsymbol{t}) \right\| \tag{7.41}$$

The sliding surface gain matrix is also determined by the LQR method.

$$\boldsymbol{u} = -\left(\boldsymbol{GC}\widehat{\boldsymbol{B}}_{\boldsymbol{N}}\right)^{-1}\boldsymbol{Gy} - \left(\boldsymbol{GC}\widehat{\boldsymbol{B}}_{\boldsymbol{N}}\right)^{-1}(\hat{\eta}_L + \sigma) sat(\boldsymbol{s}) \tag{7.42}$$

The input of the driveline system is the voltage of the DC motor in this chapter, furthermore, the voltage supplies the motor is limited.

7.6 Results and Conclusion

This chapter proposed a control method and simulation results of the limited power source. Figure 7.9 to Figure 7.11 illustrate that the simulation results of the nonlinear driveline system under the limited power condition integrated of different types of controller. Figure 7.9 illustrates the responses of the perturbated dynamic lateral misalignment, twist angle, and the output speed error with the PID controller as proposed in the structure shown in Figure 7.7. The obvious resonances are observed in Figure 7.9 when the rotating speed passage the critical speed zone due to the limited voltage that limits the torque transmitted to the driveshaft system under the $\delta_0 = 35°$ misalignment condition. .Figure 7.10 illustrates the perturbation dynamic lateral misalignment angle, twist angle, and output speed error via torsional SMC/LQR controller with limited power. Figure 7.11 shows the comparison of two angular velocity errors with different controllers with limited power. The PID controller shows the limit on passaging the resonance speed region. The SMC/LQR controller indicates being capable of eliminating the resonance with the same limited voltage level.

Left figures in Figure 7.12 and Figure 7.13 show the same response as Figure 7.9 under the $\delta_0 = 25°$ misalignment condition. However, the right figures shown the angular error between the reference speed and the actual speed rather the angular velocity. By comparison with the previous $\delta_0 = 35°$ misalignment condition, the PID controller is still not capable of passaging through the critical frequencies with the limited power condition under the lower misalignment condition. Figure 7.14 shows the comparison of the angular velocity errors with different controllers. As the figure shows, the critical frequencies are distinct. The proposed hybrid control algorithm is proven being capable of drive the nonlinear driven system through all critical frequencies during the acceleration operation smoothly. The angular velocity error is close to zero when the driveline is coupling with the hybrid SMC/LQR controller. The similar results are shown in Figure 7.15, which illustrates the comparison of the angular velocity error with the $\delta_0 = 25°$ for the subcritical case. The lateral critical frequency is still unovercome, moreover, the error starts to absent from the zero at the end of the simulation period.

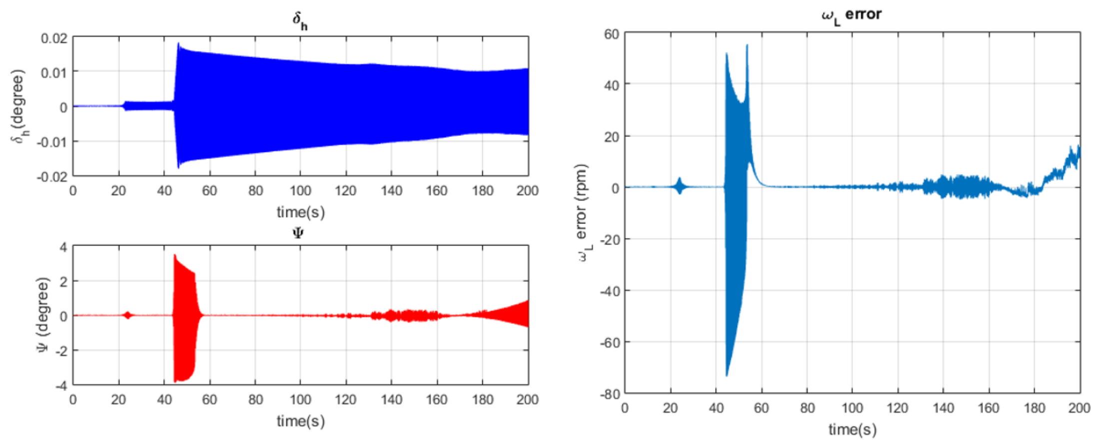

Figure 7.9 PID Controller Supercritical Case (*Va* limited): $\delta_0 = 35°$

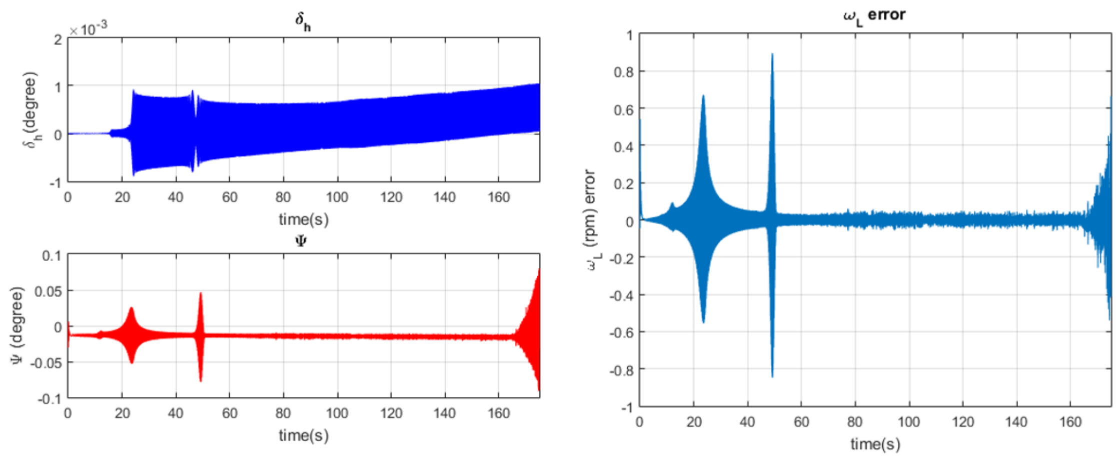

Figure 7.10 SMC/LQR Supercritical Case (*Va* limited): $\delta_0 = 35°$ (Supercritical)

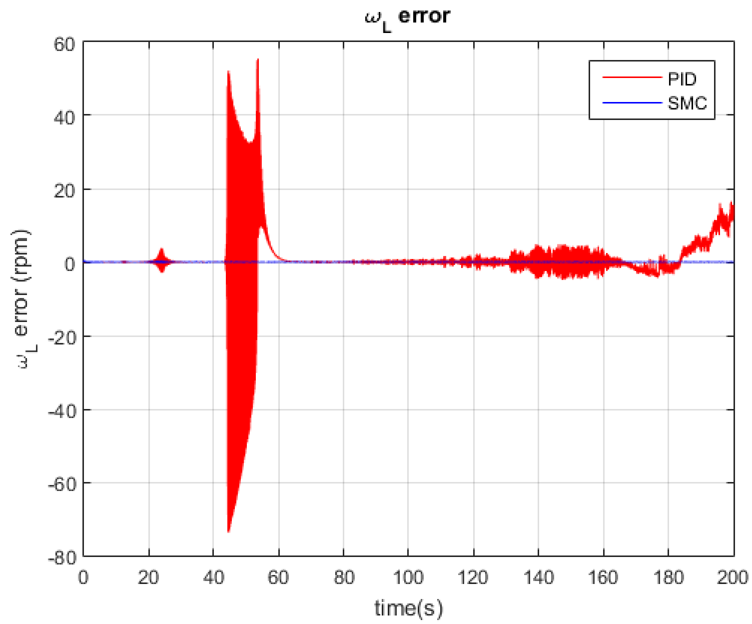

Figure 7.11 Angular Velocity Error Comparison (*Va* limited): $\delta_0 = 35°$ (Supercritical)

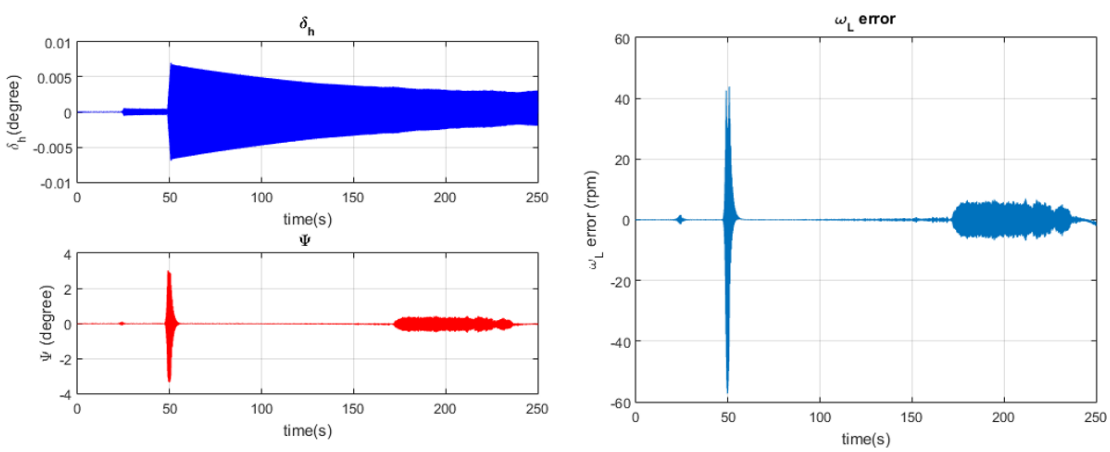

Figure 7.12 PID Controller Supercritical Case (*Va* limited): $\delta_0 = 25°$

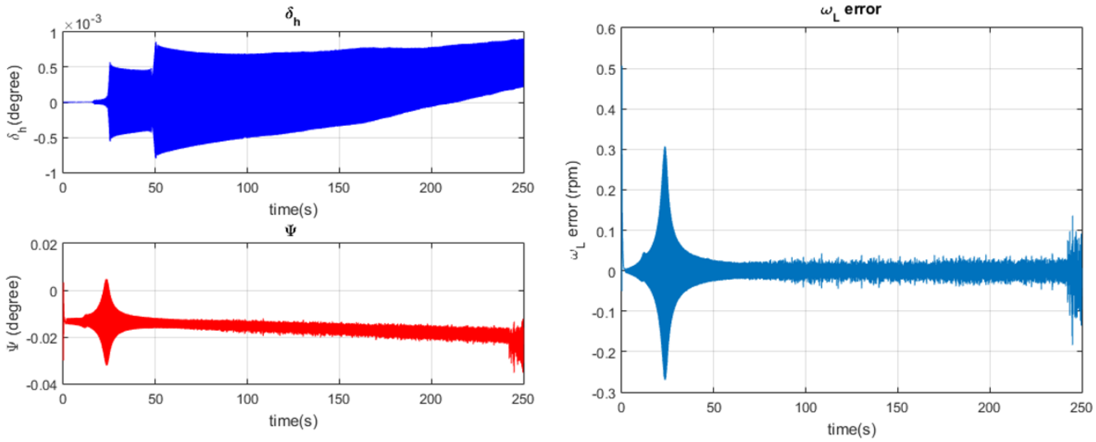

Figure 7.13 SMC/LQR Supercritical Case (*V_a* limited): $\delta_0 = 25°$

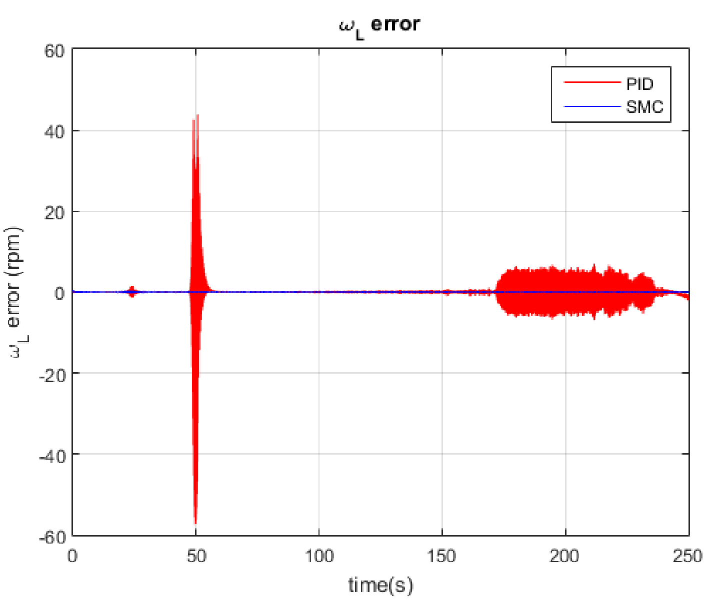

Figure 7.14 Angular Velocity Error Comparison (*V_a* limited): $\delta_0 = 25°$ (Supercritical)

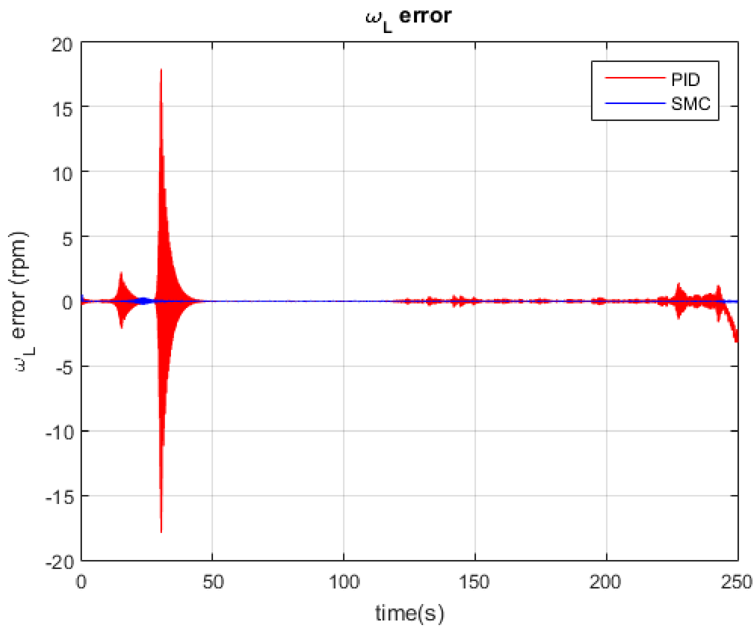

Figure 7.15 Angular Velocity Error Comparison (*V*$_a$ limited): $\delta_0 = 25°$ (Subcritical)

Chapter 8
CONCLUSIONS AND FUTURE WORK

8.1 Conclusions

This dissertation proposes the mathematical method of building the nonlinear driveshaft system model including the elastic intermediate shaft and double U-joints. Firstly, the Eulerian angles are used for mathematical modeling method for U-joint. Then the rotating speed of the intermediate shaft is delivered through the sequence of the body-fixed coordinates transformation. Moreover, the new misalignment angles are introduced to replace the Eulerian angles in the mathematical model. Secondly, the 'offset misalignment' condition is applied on the driveline system, therefore the Eulerian angles of second U-joint are expressed in a function of the Eulerian angles of the first U-joint. Furthermore, the rotating speed of the output shaft is obtained. Finally, the energy method and Lagrange's equation are applied to obtain the nonlinear equations of motion of the driveline system coupling with double U-joints.

The torque is assumed as the input of the driveline system in this dissertation instead of the assumed constant speed. Then the input speed is also a DOF of the system, unlike the previous research work.

Both the passage phenomena and the Sommerfeld effect is observed in the responses of the driveline system during the acceleration operation with constant torque input. The static misalignment condition is proven that is critical for whether the Sommerfeld effect will occur. Moreover, the critical static misalignment angle is identified at the maximum slope of the acceleration of the rotating speed.

Furthermore, the rotating speed limit varies corresponding to the different misalignment angles has been shown in results. Then the Floquet method is applied on the numerical linearized system to identify the natural frequencies respects to different static misalignment angle. The obtained natural frequency curve provides the reference explanation of the speed limits that are captured in the simulation.

The second main part of this dissertation is to propose the hybrid SMC/LQR control algorithm for torsional input to provide the proper torque to overcome the Sommerfeld effect. After the hybrid control method is designed base on the numerical approximate LTV system, it is used to control the original nonlinear driveline system. The PID controller is also applied for the torsional control under different static misalignment conditions. The comparison between the two types of the controllers illustrate that both controllers are effective under the small static misalignment conditions, however, only the proposed hybrid controller is capable of overcoming all resonance frequencies in the acceleration operation.

The limited power source is practical to provide the torque input to the driveshaft system. A DC motor model is integrated with the driveline system in Simulink. The nominal condition is involved for the compassion. As a similar request from the unlimited power condition, the control method is also investigated involving the DC model for the controller design. As well as the unlimited case, the PID controller has applied to the limited DC motor model tor the comparison with the hybrid SMC/LQR control algorithm. The proposed hybrid controller has a better effect on alleviating the vibration even though under the limited power condition with the large static misalignment angle.

8.2 Future Work

Firstly, a numerical approximate linear time-varying model is proposed and used for the systematic properties exploring and the controller design. The proposed LTV model is valid for the controller design for both unlimited or limited power conditions. The natural frequencies of the LTV corresponding to the different static misalignment conditions provide the reference for the physical properties of the critical frequencies obtains thorough the numerical simulation.

Furthermore, the detailed analysis of the limit cycle response of the rotating speed limit is required to help to understand the properties of the speed limit. Moreover, investigating the more forms of the simplified driveline model, which is required being valid for the harmonic method to analyze the potential critical frequencies of the nonlinear driveline system and predicting the speed limit value when the Sommerfeld effect is observed.

Secondly, further research work will focus on the integration of the nonlinear driveline system and the limited power source. The analysis of the minimum power required for the nonlinear driveline system to overcome the Sommerfeld effect is the substantial parameter for the system design. The proper voltage can be determined with the reference of the power required. Due to the complication of the system model, the accurate simplified model is also required.

Last but not least, the LQR is applied to the proposed hybrid SMC/LQR controller in this dissertation. However, the proper weighting matrices are attainable to be determined for some cases. The H_2/H_∞ control law with LMI method is an option to supplant the LQR for determining the sliding surface gain matrix. This is more general than the LQR to determine the gain instead of manually adjusting the gain matrices.

In conclusion, analysis of the limit cycle response and the evaluated linear system are the priority assignments for further systematic investigation and design. The optional robust control method will be integrated into the new hybrid control algorithm.

LIST OF REFERENCES

Asokanthan, S., & Meehan, P. (2000). Non-linear vibration of a torsional system driven by a Hooke's joint. *Journal of Sound Vibration, 233*(2), 297-310.

Asokanthan, S., & Wang, X.-H. (1996). Characterization of torsional instabilities in a Hooke's joint driven system via maximal Lyapunov exponents. *Journal of Sound Vibration, 194*(1), 83-91.

Bag, S., Spurgeon, S., & Edwards, C. (1996). Robust sliding mode design based upon output feedback.

Bag, S. K., Spurgeon, S. K., & Edwards, C. (1996). *Dynamic output feedback sliding mode design for linear uncertain systems.* Paper presented at the Proceedings of 35th IEEE Conference on Decision and Control.

Belato, D., Weber, H. I., Balthazar, J. M., & Mook, D. T. (2001). Chaotic vibrations of a nonideal electro-mechanical system. *International Journal of Solids Structures, 38*(10-13), 1699-1706.

Bisoi, A., Samantaray, A., & Bhattacharyya, R. (2017). Control strategies for DC motors driving rotor dynamic systems through resonance. *Journal of Sound Vibration, 411*, 304-327.

Bolla, M., Balthazar, J. M., Felix, J., & Mook, D. (2007). On an approximate analytical solution to a nonlinear vibrating problem, excited by a nonideal motor. *Nonlinear Dynamics, 50*(4), 841-847.

Browne, M., & Palazzolo, A. (2009). Super harmonic nonlinear lateral vibrations of a segmented driveline incorporating a tuned damper excited by non-constant velocity joints. *Journal of sound vibration, 323*(1-2), 334-351.

Bulut, G. (2014). Dynamic stability analysis of torsional vibrations of a shaft system connected by a Hooke′ s joint through a continuous system model. *Journal of Sound Vibration, 333*(16), 3691-3701.

Bulut, G., & Parlar, Z. (2011). Dynamic stability of a shaft system connected through a Hooke's joint. *Mechanism Machine Theory, 46*(11), 1689-1695.

Chan, M.-L., Tao, C.-W., & Lee, T.-T. (2000). Sliding mode controller for linear systems with mismatched time-varying uncertainties. *Journal of the Franklin Institute, 337*(2-3), 105-115.

Crolla, D. (1978). Torsional vibration analysis of tractor and machine pto drivelines. *Journal of Agricultural Engineering Research, 23*(3), 259-272.

DeSmidt, H., Wang, K., & Smith, E. (2002). Coupled torsion-lateral stability of a shaft-disk system driven through a universal joint. *Journal of applied mechanics, 69*(3), 261-273.

DeSmidt, H., Wang, K., & Smith, E. (2004). Stability of a segmented supercritical driveline with non-constant velocity couplings subjected to misalignment and torque. *Journal of sound vibration, 277*(4-5), 895-918.

Dewell, D., & Mitchell, L. (1984). Detection of a misaligned disk coupling using spectrum analysis. *Journal of vibration, acoustics, stress, reliability in design, 106*(1), 9-16.

Dimentberg, M., McGovern, L., Norton, R., Chapdelaine, J., & Harrison, R. (1997). Dynamics of an unbalanced shaft interacting with a limited power supply. *Nonlinear Dynamics, 13*(2), 171-187.

Edwards, C., & Spurgeon, S. K. (1994). On the development of discontinuous observers. *International Journal of control, 59*(5), 1211-1229.

Edwards, C., & Spurgeon, S. K. (1995). Sliding mode stabilization of uncertain systems using only output information. *International Journal of Control, 62*(5), 1129-1144.

Edwards, C., Spurgeon, S. K., & Akoachere, A. (2000). A sliding mode static output feedback controller based on linear matrix inequalities applied to an aircraft system. *Journal of Dynamic Systems, Measurement, Control, 122*(4), 656-662.

El-Khazali, R., & Decarlo, R. (1995). Output feedback variable structure control design. *Automatica, 31*(6), 805-816.

Felix, J. L. P., & Balthazar, J. M. (2009). Comments on a nonlinear and nonideal electromechanical damping vibration absorber, Sommerfeld effect and energy transfer. *Nonlinear Dynamics, 55*(1-2), 1-11.

Gonçalves, P., Silveira, M., Junior, B. P., & Balthazar, J. (2014). The dynamic behavior of a cantilever beam coupled to a non-ideal unbalanced motor through numerical and experimental analysis. *Journal of Sound Vibration, 333*(20), 5115-5129.

Guan, P., & DeSmidt, H. (2018). *Parametric Instability of Planetary Gear Transmission Mounted on Discrete Support Struts With Minimum Ring Gear Rim Thickness Design.* Paper presented at the ASME 2018 International Mechanical Engineering Congress and Exposition.

Iwatsubo, T., & Saigo, M. (1984). Transverse vibration of a rotor system driven by a Cardan joint. *Journal of Sound and Vibration, 95*(1), 9-18.

Karthikeyan, M., Bisoi, A., Samantaray, A., & Bhattacharyya, R. (2015). Sommerfeld effect characterization in rotors with non-ideal drive from ideal drive response and power balance. *Mechanism Machine Theory, 91*, 269-288.

Kato, M., & Ota, H. (1990). Lateral excitation of a rotating shaft driven by a universal joint with friction. *Journal of Vibration Acoustics, 112*(3), 298-303.

Kato, M., Ota, H., & Kato, R. (1988). Lateral-Torsional Coupled Vibrations of a Rotating Shaft Driven by a Universal Joint: Derivation of Equations of Motion and Asymptotic Analyses. *JSME international journal. Ser. 3, Vibration, control engineering, engineering for industry, 31*(1), 68-74.

Kirk, R., Mondy, R., & Murphy, R. (1984). Theory and guidelines to proper coupling design for rotor dynamics considerations. *Journal of Vibration and Acoustics, 106*(1), 129-138.

Kononenko, V. (1969). Vibrating Systems with a Limited Power Supply,(1969). *London Illife Kooks LTD*, 236.

Krasnopolskaya, T. S., & Shvets, A. Y. (1993). Chaos in vibrating systems with a limited power - supply. *Chaos: An Interdisciplinary Journal of Nonlinear Science, 3*(3), 387-395.

Lewis, A., & Sinha, A. (1999). Sliding mode control of mechanical systems with bounded disturbances via output feedback. *Journal of guidance, control, and dynamics, 22*(2), 235-240.

Li, D., & Slotine, J.-J. E. (1987). *On sliding control for multi-input multi-output nonlinear systems.* Paper presented at the 1987 American Control Conference.

Mazzei Jr, A., Argento, A., & Scott, R. (1999). Dynamic stability of a rotating shaft driven through a universal joint. *Journal of Sound Vibration, 222*(1), 19-47.

Mazzei Jr, A. J. (2011). Passage through resonance in a universal joint driveline system. *Journal of Vibration Control, 17*(5), 667-677.

Ogata, K., & Yang, Y. (2002). *Modern control engineering* (Vol. 4): Prentice-Hall.

Pai, M.-C., & Sinha, A. (2006). *Sliding mode output feedback control of time-varying mismatched uncertain systems.* Paper presented at the SMC'06. IEEE International Conference on Systems, Man and Cybernetics, 2006.

Saigo, M., Okada, Y., & Ono, K. (1997). Self-excited vibration caused by internal friction in universal joints and its stabilizing method. *Journal of Vibration Acoustics, 119*(2), 221-229.

Samantaray, A., Dasgupta, S., & Bhattacharyya, R. (2010). Sommerfeld effect in rotationally symmetric planar dynamical systems. *Int J Eng Sci, 48*(1), 21-36.

Sheu, P.-P., Chieng, W.-H., & Lee, A.-C. (1996). Modeling and analysis of the intermediate shaft between two universal joints. *Journal of vibration acoustics, 118*(1), 88-99.

Slotine, J.-J., Hedrick, J. K., & Misawa, E. A. (1987). On sliding observers for nonlinear systems. *Journal of dynamic systems, Measurement, Control, 109*(3), 245-252.

Sommerfeld, A. (1902). Beiträge zum dynamischen ausbau der festigkeitslehe. *Physikal Zeitschr, 3*, 266-286.

Tsuchida, M., de Lolo Guilherme, K., & Balthazar, J. M. (2005). On chaotic vibrations of a non-ideal system with two degrees of freedom: 1: 2 resonance and Sommerfeld effect. *Journal of Sound Vibration, 282*, 1201-1207.

Utkin, V. (1977). Variable structure systems with sliding modes. *IEEE Transactions on Automatic control, 22*(2), 212-222.

Utkin, V., & Shi, J. (1996). *Integral sliding mode in systems operating under uncertainty conditions.* Paper presented at the Proceedings of the 35th IEEE Conference on Decision and Control, 1996.

Verichev, N. (2012). Chaotic torsional vibration of imbalanced shaft driven by a limited power supply. *Journal of Sound Vibration, 331*(2), 384-393.

Wang, W.-J., & Fan, Y.-T. (1993). *Output feedback in variable structure systems with a simple adaption law.* Paper presented at the Proceedings of the 32nd IEEE Conference on Decision and Control, 1993.

Wang, W.-J., & Fan, Y.-T. (1994). New output feedback design in variable structure systems. *Journal of guidance, control, dynamics, 17*(2), 337-340.

Woodham, C., & Zinober, A. (1993). Eigenvalue placement in a specified sector for variable structure control systems. *International Journal of Control, 57*(5), 1021-1037.

Xu, M., & Marangoni, R. (1994a). Vibration analysis of a motor-flexible coupling-rotor system subject to misalignment and unbalance, Part I: theoretical model and analysis. *Journal of Sound and Vibration, 176*(5), 663-679.

Xu, M., & Marangoni, R. (1994b). Vibration analysis of a motor-flexible coupling-rotor system subject to misalignment and unbalance, part II: experimental validation. *Journal of sound vibration, 176*(5), 681-691.

Yoerger, D., & Slotine, J. (1985). Robust trajectory control of underwater vehicles. *IEEE Journal of Oceanic Engineering, 10*(4), 462-470.

Zhao, J., DeSmidt, H., & Yao, W. (2015). *Damage identification via asymmetric active magnetic bearing acceleration feedback control.* Paper presented at the Sensors and Smart Structures Technologies for Civil, Mechanical, and Aerospace Systems 2015.

VITA

Wei Yao was born in Shanghai, China in 1986. He graduated from Shanghai University of Engineering Science, China, in 2008 with a Bachelor of Engineering degree in Automation. Prior to pursue his graduate degree, he held a position as product development engineer at Shanghai Sanden Behr Automotive Air Condition Co.,Ltd from 2008 to 2009. After he received the Master of Science in mechanical engineering at Lawrence Technological University in 2012. He joined Dr. Hans DeSmidt's research group in August 2012 to pursue his Doctor of Philosophy degree. His research focuses on modeling and simulation of driveshaft system coupling with U-joint, rotordynamics, structural dynamics, stability analysis, time-varying system analysis, and advanced control theory.